Max-Planck-Institut
für Meteorologie

EXAMENSARBEIT Nr. 74

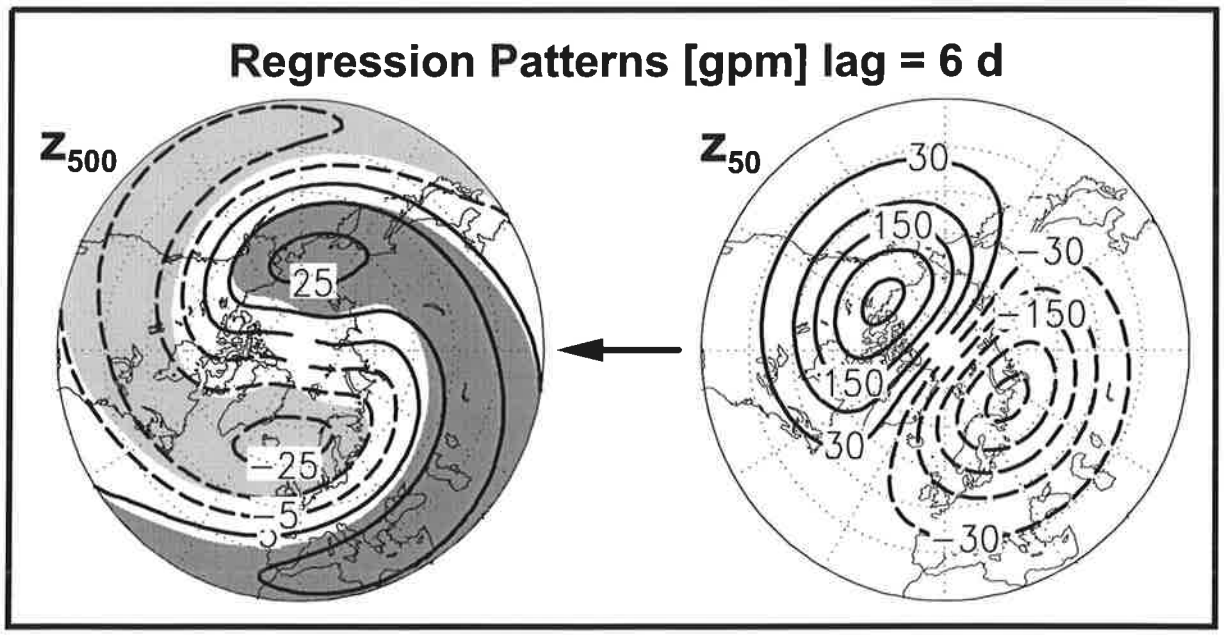

THE DYNAMICAL LINK BETWEEN THE TROPOSPHERE AND STRATOSPHERE AND ITS POTENTIAL TO AFFECT CLIMATE

by

Judith Perlwitz

HAMBURG, June 2000

Dissertation zur Erlangung des Doktorgrades

Autor:

Judith Perlwitz

Max-Planck-Institut
für Meteorologie

MAX-PLANCK-INSTITUT
FÜR METEOROLOGIE
BUNDESSTRASSE 55
D - 20146 HAMBURG
GERMANY

Tel.: +49-(0)40-4 11 73-0
Telefax: +49-(0)40-4 11 73-298
E-Mail: <name> @ dkrz.de

ISSN 0938-5177

The Dynamical Link Between the Troposphere and Stratosphere and its Potential to Affect Climate

Dissertation
zur Erlangung des Doktorgrades
der Naturwissenschaften im Fachbereich
Geowissenschaften
der Universität Hamburg

vorgelegt von
Judith Perlwitz
aus Reuterstadt Stavenhagen

Hamburg 2000

Als Dissertation angenommen vom Fachbereich Geowissenschaften
der Universität Hamburg

aufgrund der Gutachten von Herrn Priv. Doz. Dr. H.-F. Graf
und Herrn Prof. Dr. K. Fraedrich

Hamburg, den 24.05.2000

Prof. Dr. U. Bismayer
Dekan des Fachbereiches Geowissenschaften

Abstract

The main issue of this thesis has been to increase our understanding of the mechanisms by which the stratosphere can affect the tropospheric climate. The dynamical coupling of tropospheric and stratospheric circulation in the Northern Hemisphere was investigated by applying the new approach Single Wave Analysis which combines a well-known theoretical concept of the coupling mechanism with the statistical analysis of observational datasets. The isolated features were used to interpret both the coupled modes of variability in tropospheric and stratospheric geopotential height fields and the changes in the estimated probability density function of these modes.

The prominent result of this thesis is that winter seasons characterized either by an anomalously strong or weak polar winter vortex exhibit different tropospheric circulation regimes. Only in the case of a strong stratospheric polar vortex does a downward control of the tropospheric circulation by reflection of waves of zonal wave number (ZWN) one occur. This downward influence on the structure of tropospheric waves is considerably less than the influence of tropospheric disturbances on the structure of stratospheric waves of ZWN 1 and 2. This result confirms our understanding of the coupling of stratosphere and troposphere: Waves in the stratosphere originate in the troposphere, whereas the disturbances in the tropospheric circulation result mainly from internal processes. However, the findings also reveal that the two circulation regimes, characterized either by an preferred exaggeration of an anomalously strong or weak polar winter vortex, exhibit different tropospheric variability structures and are of high relevance to interannual and interdecadal climate variability.

Contents

Chapter 1

Introduction

The Earth's observed climate state results from the interaction between the components of the climate system atmosphere, hydrosphere, cryosphere, lithosphere and biosphere. The climate state varies on all time scales. Spectral analysis of long-term meteorological, oceanic and glacial records reveals that the spectra of these time series tend to be red. That is, amplitudes increase with decreasing frequency. On one hand, climate variability is caused by free variations due to internal instabilities and positive and negative feedbacks, leading to nonlinear interactions among the various components of the climate system. On the other hand, the climate system is affected by external factors, comprising *astronomical variations* (the intensity of solar irradiance, orbital parameters of the earth) and *terrestrial forcings* (variations in the atmospheric composition e.g. due to volcanic eruptions or human activity). The response to external forcing, however, can be modified by the strong interaction between atmosphere, ocean and cryosphere (Peixoto and Oort, 1992).

A principal objective of climate research is to understand the origin of climate variability on different time scales. This knowledge is required to predict climate variations and to study whether climate change observed in recent decades is anthropogenic in origin. The atmospheric system alone is sufficiently complex and nonlinear to generate low-frequency variability without recourse to any forcing from other climate components or external forcing (e.g. James and James, 1992; Dethloff et al., 1998). However, as one considers low-frequency fluctuations of the atmosphere, the effects of coupling between the atmosphere and more slowly varying components of the climate system become very important. A considerable source of natural climate variability is the interaction of the lower atmosphere with the underlying ocean. This interaction has been broadly studied because the ocean, due to its enormous thermal inertia, provides an important memory for decadal and longer-term climate variations (e.g., Trenberth, 1995). At the beginning of the 90s it was recognized that the stratosphere also plays an important

role in the climate system and that the effect of anthropogenic emissions could modify this role. Therefore, in 1992, the World Climate Research Program established the project "Stratospheric Processes And their Role in Climate" (SPARC) to integrate research into stratospheric processes with investigations of natural climate variability and climate change.

Knowledge of the processes linking the stratosphere and troposphere is a prerequisite for the assessment of the potential of the stratosphere to cause and to modify changes in the climate system (SPARC, 1993). The main objective of this thesis is to study the dynamical link between troposphere and stratosphere, and its importance for the genesis of natural and anthropogenic climate variations. We will show that it is necessary, at least in the cold season, to treat the troposphere and stratosphere in the Northern Hemisphere (NH) as a coupled system to increase our understanding of:

- the origin of natural climate variability,
- the origin and spatial structure of the climate change observed during the last four decades,
- the spatial structure of atmospheric circulation changes due to anthropogenic greenhouse effect.

Section 1.1 describes important links between the troposphere and stratosphere and their potential in affecting climate. Our knowledge of modes of natural climate variability of the coupled troposphere-stratosphere circulation is summarized in Section 1.2. In Section 1.3, the objectives and structure of this thesis are introduced.

1.1 Links Between the Troposphere and Stratosphere and Their Potential to Affect Climate

The troposphere and stratosphere are a coupled system, interacting through dynamical, radiative and chemical processes (Figure 1.1). There is clear evidence for the importance of tropospheric processes in determining the structure of the stratosphere (Andrews et al., 1987). The thermal structure of the stratosphere is influenced by upwelling thermal radiation originating in the troposphere and by solar backscattering from the surface and clouds. The chemical composition of the stratosphere is affected by tropospheric source gases that are transported

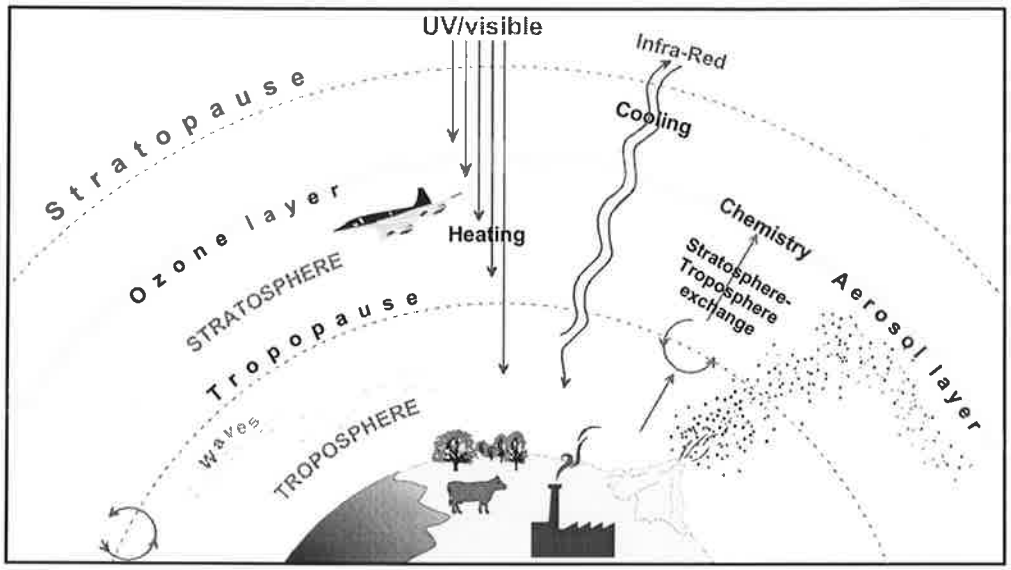

Figure 1.1. Processes affecting the troposphere-stratosphere system (adapted from SPARC, 1993)

into the stratosphere and by the loss of photochemically active gases through transport into the troposphere. The general circulation of the stratosphere is controlled to a great extent by vertically propagating planetary waves generated in the troposphere.

There is growing evidence from observational data and model experiments that the stratosphere cannot be neglected when variations and long-term changes of the tropospheric state are studied (SPARC, 1998). Due to the radiative link between the stratosphere and troposphere, changes in the concentration of stratospheric trace gases and aerosols have a direct influence on the net radiative balance of the surface-troposphere system. *Ozone*, the most important trace species in the stratosphere, reduces the downward radiative flux at the tropopause by absorbing and reflecting solar radiation. *Volcanic sulfate aerosol* in the stratosphere causes surface cooling by scattering incoming solar radiation. The stratosphere interacts with the troposphere and the climate system by the *exchange of longwave radiation*: The warm Earth's surface emits longwave radiation into the atmosphere, this radiation is absorbed and re-emitted to the surface by a number of molecules, like water vapor, carbon dioxide, methane, ozone, nitrous oxide and chlorofluoromethanes (CFCs). These trace species produce the so-called *greenhouse effect* of the atmosphere.

Variations in the *thermal* and *dynamical* structure of the stratosphere are closely related. It is less obvious, however, how the mean flow or planetary waves in the stratosphere play a significant role in the circulation of the troposphere. A possible mechanism that might operate in addition to the radiative influence of strato-

spheric perturbations on tropospheric energetics was suggested by Hines (1974). The basic idea of this mechanism is that stratospheric and mesospheric winds play a dominant role in determining the "refractive index" (Charney and Drazin, 1961; Matsuno, 1970) and, therefore, the transmission-refraction properties of planetary-scale waves, propagating vertically into the strato- and mesosphere. These tropospheric planetary waves can be refracted both meridionally and downward by an anomalously strong polar winter vortex. Thus, the strengthening of the stratospheric mean flow might alter the amplitude and phase of vertically propagating tropospheric planetary waves. Sensitivity experiments with linear wave propagation models (e.g., Bates, 1977; Geller and Alpert, 1980; Schmitz and Grieger, 1980) and GCMs (Boville, 1984; Kodera et al., 1990; Kodera and Koide, 1997) illustrate that the mean stratospheric flow significantly affects tropospheric stationary waves.

GCM experiments reveal that not only linear but also non-linear processes are important, which may influence tropospheric dynamics and climate. Boville (1984) showed that both stationary and transient components of tropospheric waves are affected. On the basis of sensitivity studies with a middle atmosphere model, Kodera et al. (1990) demonstrated that anomalies of the zonal mean zonal wind, which are created initially in the mesosphere, propagate downward into the troposphere by wave-mean flow interaction and modify the strength of the subtropical jet.

The intensity of the cyclonic polar winter vortex in the stratosphere is modified by climate perturbations such as injections of volcanic aerosol and solar activity. *Volcanic aerosol* absorbs both near-infrared and long wave radiation and has been observed to heat the tropical lower stratosphere by about 4–6 K (Labitzke and v. Loon, 1996). During the cold season, the heating of the lower tropical stratosphere leads to an increase in the meridional temperature gradient and, thus, to a strengthening of the westerly thermal wind in the lower stratosphere. In a positive feedback loop, the cyclonic polar winter vortex is further strengthened because the northward transport of heat by planetary waves is reduced. *Solar activity* and the *Quasi-Biennial Oscillation* (QBO) also influence the strength of the stratospheric polar winter vortex. In observational records of stratospheric temperature and circulation a 10-to-12 year oscillation was detected, which is in phase with the 11-year solar cycle (Labitzke and van Loon, 1988; van Loon and Labitzke, 1988; Kodera, 1993). Model experiments reveal that the interaction of solar irradiance and ozone changes can increase climate sensitivity (Shindell et al., 1999a).

Since the beginning of regular observation of the NH stratosphere in 1958, a significant strengthening of the cyclonic polar winter vortex has been observed (Kodera and Koide, 1997; Thompson and Wallace, 1998; Graf et al., 1995; Perlwitz and Graf, 1995). The causes for this change are not as yet clear. One reason may be the anthropogenic emissions of trace gases. In an earlier study (Perlwitz

and Graf, 1995), we proposed a physical process which may explain this alteration of the stratospheric circulation by increased greenhouse forcing: The increase in tropospheric temperature and humidity in lower latitudes due to the combined greenhouse effect leads to a lifting of the lower latitude geopotential height layers and, thus, to an initial intensification of the polar winter vortex by strengthening of the thermal wind. Sensitivity experiments with comprehensive climate models show a continuous intensification of the stratospheric polar winter vortex with increasing anthropogenic greenhouse gas concentration (Shindell et al., 1999b; Graf et al., 1995; Perlwitz et al., 1997). Ramaswamy et al. (1996) and Graf et al. (1998) linked an intensified polar winter vortex at the end of the boreal winter to the observed ozone decease at high latitudes. However, the observational record is too short to exclude the possibility that these observed changes in stratospheric circulation may be caused by natural interdecadal variations of the climate system (Feser et al., 2000).

The stratosphere contains just 10–20% of the atmosphere's total mass. Thus, one might expect the contribution of changes in the stratospheric state by external forcing or internal variability to climate variations to be negligible. However, relatively small amounts of energy may give rise to significant effects on temperature and circulation in the middle atmosphere where the density is low. Due to the dynamical link, changes in the stratospheric winter circulation can significantly affect climate. On the basis of 90-day low-pass filtered observational data of the NH winter season, Baldwin and Dunkerton (1999) found indications for this *downward control* of tropospheric circulation. They calculated the first empirical orthogonal function (EOF) from a single field consisting of geopotential at five pressure levels (1000-, 300-, 100-, 30- and 10-hPa). They showed that a hemispheric-scale anomaly pattern of this EOF, called the *Arctic Oscillation* (AO), takes about three weeks to propagate from the 10-hPa level to the surface. Observational evidence for downward control of climate by the stratosphere was also found by studying the NH temperature anomalies after strong tropical volcanic eruptions. Historical records of near surface temperature reveal that the forcing by volcanic sulfate aerosol causes not only a global-scale cooling but also a winter warming over the NH continents at middle and high latitudes (Robock and Mao, 1992). Sensitivity experiments (Graf et al., 1993) and observational data (Perlwitz and Graf, 1995) indicate that this *unexpected* warming results mainly from a modification of the structure of planetary-scale waves in the troposphere, which is related to an intensified stratospheric polar winter vortex.

1.2 Variability Modes of the Coupled Troposphere-Stratosphere Circulation

To gain insight into the spatial features which characterize the coupling between stratospheric and tropospheric circulation, their quasi-stationary coupled modes of variability have been statistically determined. Multivariate statistical methods like singular value decomposition (SVD) analysis (Baldwin et al., 1994; Cheng and Dunkerton, 1995) and canonical correlation analysis (CCA)(Perlwitz and Graf, 1995) have been used to isolate the coupled modes of variability in NH 50- and 500-hPa geopotential height fields. Kodera et al. (1996) found structural relationships similar to our findings (Perlwitz and Graf, 1995) by deriving EOFs and applying regression analysis. On the basis of winter means ($\overline{\text{DJF}}$), Baldwin et al. (1994) isolated one mode of coupled variability. Using the monthly mean values of the winter season, we found that the linear relationship between tropospheric and stratospheric circulation in the NH can be largely described by two coupled modes (Perlwitz and Graf, 1995).

The first coupled mode of variability describes the relationship between the strength of stratospheric (cyclonic) winter vortex and the index of a tropospheric wave train which covers the North Atlantic and Eurasia (Baldwin et al., 1994; Perlwitz and Graf, 1995; Kodera et al., 1996). This wave train includes the centers of action of the North Atlantic Oscillation (NAO). The preferred coupled mode is also linked to pronounced regional anomalies in both lower tropospheric temperature and precipitation (Hurrell, 1995; Thompson and Wallace, 1998; Perlwitz and Graf, 1995). It is assumed that this coupled mode of NH winter circulation evolves from the wave-mean flow interaction between tropospheric planetary waves and the mean westerly flow in the stratosphere (Matsuno, 1970). Therefore, it can be exaggerated both by stratospheric and tropospheric processes (Graf et al., 1997).

The second mode of coupled variability describes the connection of a tropospheric wave train over the North Pacific/North America region and a hemispheric-scale wave-like pattern of stratospheric geopotential heights. This stratospheric wave pattern describes a perturbation of the stratospheric polar winter vortex by waves of zonal wave numbers (ZWNs) 1 and 2. On the interannual time scale, the second coupled mode is related to the sea surface temperature (SST) in the tropical Pacific (Kodera et al., 1996; Perlwitz and Graf, 1995). This mode also corresponds to results of Baldwin and O'Sullivan (1995). They studied the stratospheric effects of ENSO-related tropospheric teleconnection patterns, using winter mean time series and found that these tropospheric teleconnection patterns were related to the structure of large-scale planetary waves in the lower stratosphere.

The two modes of coupled troposphere-stratosphere circulation represent specific forms of variability which are internally generated in the atmosphere by physical

processes. They were identified in control experiments with GCMs using a climatological SST distribution prescribed as lower boundary condition (Graf et al., 1997). They were also isolated in a coupled atmosphere-ocean general circulation model (AOGCM) with low horizontal and vertical resolution in which the upper-boundary of the model is at the 1 hPa level (Kitoh et al., 1996).

1.3 Objectives and Structure of this Thesis

The main theoretical concept for the understanding of the mutual dynamical coupling between troposphere and stratosphere is based on wave-mean flow interaction between tropospheric planetary waves and the mean stratospheric flow. *It is difficult to find evidence in observational data, about which way the tropospheric circulation is changed by variations in the stratospheric circulations.* A recent study by Baldwin and Dunkerton (1999) has illustrated the downward propagation of the so called "AO-signal" from the stratosphere (10 hPa level) to the surface. However, the physical mechanisms which lead to the circulation anomalies in the troposphere are not explained in this study. We propose an approach called Singular Wave Analysis (SWAN) for the study of the dynamical coupling between tropospheric and stratospheric circulation. In this approach our theoretical understanding of the mutual coupling between both atmospheric layers is used to underpin multivariate statistical methods.

In the last four decades, the cold season climate of the boreal hemisphere has changed significantly. Striking features of this change are the strengthening of both the cyclonic polar vortex in the stratosphere and the westerlies over the North Atlantic (Kodera and Koide, 1997; Graf et al., 1995; Perlwitz and Graf, 1995). The recent study by Corti et al. (1999), based on the suggestions of Palmer (1993), has used the probability density function (PDF) of variability modes of climate parameters for both describing the climate state and studying climate changes (Corti et al., 1999). EOF analysis was used to isolate the modes of variability of mid-tropospheric circulation. Modes of natural climate variability, estimated with the help of multivariate statistical methods, should reflect the relevant physical processes. Only then can these modes be successfully used for the description of both the physical climate state and processes characterizing climate changes. The leading EOFs are the eigenvectors of the covariance matrix of a dataset. *It is not clear, however, whether EOF analysis is the proper method for isolating variability modes in a physically optimized way.* We will study coupled modes of variability of the troposphere/stratosphere circulation system and discuss their implications for our understanding of both the spatial structure of atmospheric variability and observed interdecadal climate change.

The intensity of the stratospheric polar winter vortex determines the transmission-

refraction properties of tropospheric waves. The preferred excitation of a strong polar winter vortex by external forcing or internal climate variability leads to a strong trapping of the energy of ultra-long planetary waves in the troposphere. *The importance of this dynamical process for the spatial structures of variability modes and the climate response to increased anthropogenic greenhouse gas forcing have not yet been investigated.* We will use a long-term control integration and a climate change experiment carried out with the AOGCM ECHAM3-LSG to study the consequences of this process.

The outline of this thesis is as follows: In Chapter 2 the applied multivariate statistical methods and our statistical-dynamic approach, SWAN, are described. In Chapter 3 the reliability of the reanalyses of the National Centers for Environmental Prediction (NCEP) for studying climate change is discussed. This dataset was the main source of our investigations. Chapter 4 illustrates differences between the dynamical structures of the troposphere and stratosphere. In Chapters 5 and 6, SWAN is applied to isolate relevant features of the vertical propagation of tropospheric and stratospheric waves. Climate diagnostics on the basis of variability modes of the coupled troposphere/stratosphere circulation system are carried out in Chapter 7. In Chapter 8 we introduce an aspect of the dynamical coupling of the troposphere and stratosphere relevant to interdecadal climate change based on AOGCM integrations. An overview of the results and an outlook are given in Chapter 9.

Chapter 2

Statistical Methods and Dynamical Approaches

In this thesis, multivariate statistical methods are applied to both observational and model data. The methods are used for studying the coherent variation of tropospheric and stratospheric circulation and to analyze the relevant processes which characterize the dynamical coupling between both atmospheric layers. For the latter description knowledge of the processes of this coupling and the application of statistical methods are combined in developing an approach called *Single Wave Analysis* (SWAN). In the following, the multivariate statistical methods (Section 2.1) and the statistical-dynamic approach SWAN (Section 2.2) are introduced.

2.1 Multivariate Statistical Methods

Atmospheric datasets often contain a geophysical parameter of interest $s_i(t)$ (e.g., 500-hPa geopotential height of the NH) which is simultaneously observed at $i = 1, \ldots, N_s$ grid points or stations over $t = 1, \ldots, T$ time units. Statistical methods are applied to select information about physical and dynamical structures inherent in the datasets. An often declared aim in climate diagnostics is to identify *relevant* spatial patterns which can be interpreted physically. There are various statistical techniques to study the coherent relationships within the time series of one dataset or among the time series of different datasets. The simplest methods of analysis are composites and correlation. Based on selected reference grid points, reverence stations or temporal indices, these methods are easy to perform. However, they involve subjective decisions about the choice of reference time series (Bretherton et al., 1992). The application of multivariate statistical

methods based on matrix operations allows an elegant and more objective determination of complex spatial structures. Principal Component Analysis (PCA), CCA and SVD[1] analysis are linear multivariate methods which are often used in climate diagnostics. PCA, which is mainly called EOF analysis in geophysical studies, is applied to a single dataset to select spatial patterns that optimally describe the relationships between the time series in one field. CCA and SVD analysis can be understood to be a generalization of the PCA. With the help of both methods, pairs of patterns in the two datasets can be isolated that optimally describe the relationships between the two fields.

What these multivariate methods have in common is that they maximize a special squared property of interest, like covariance (EOF and SVD analysis) or correlation (CCA). These properties are maximized subject to a certain constraint like spatial orthogonality. Often two or more ways can be chosen to find the characteristic patterns. One way consists of the formulation of an eigenproblem which has to be solved (von Storch and Zwiers, 1998). A second one is offered by the application of the singular value decomposition theorem (Bretherton et al., 1992) described in Appendix A.2.

In this thesis the three multivariate methods mentioned above are applied. In the following, the EOF analysis (Section 2.1.1) is described according to Peixoto and Oort (1992), and SVD analysis and CCA (Section 2.1.2) are compared. The latter two descriptions follow the papers of Bretherton et al. (1992) and Cherry (1996).

2.1.1 EOF Analysis

First proposed by Pearson (1902), the EOF analysis detects linear transformations of a dataset that concentrate as much of the total variance as possible into a small number of variables. Since its introduction into atmospheric science by Fukuoka (1951) and Lorenz (1956), and especially to climate research by Kutzbach (1967), this statistical method has been widely used to study the linear relationships within one dataset. Geophysical fields are characterized by high correlations between measurements at different grid points. Therefore, EOF analysis makes it possible to describe the spatial structure of a multi-dimensional variable with a relatively small number of spatial patterns and the corresponding expansion coefficients in the time domain.

[1] In general, SVD is a special matrix theorem of linear algebra, which is presented in appendix A.2. In climate diagnostics the term *SVD* or *SVD analysis* is widely used to indicate a linear multivariate method, which maximizes the covariance between two datasets. To avoid confusion, von Storch and Zwiers (1998) called this statistical method *Maximum Covariance Analysis.*

Analysis Description

Let us suppose a random vector $\mathbf{s} = (s_1, \ldots, s_{N_s})'$ characterizing a geophysical field at $i = 1, \ldots, N_s$ grid points. The notation $(')$ indicates the transpose of a vector or matrix. Supposing $t = 1, \ldots, T$ observations, a $T \times N_s$ data matrix $\mathbf{S}$ can be defined. In this matrix the ith column contains the T observations of the grid point s_i. For convenience it will be assumed that this vector has mean 0; that is, $\langle s_i \rangle_t = 0$ for all $i = 1, \ldots, N_s$, where $\langle s_i \rangle_t$ denotes the time average over T observations. The sample covariance matrix based on the recorded observations of the field s is

$$\mathbf{C}_{ss} = \frac{1}{T}\mathbf{S}'\mathbf{S} \qquad (N_s \times N_s). \tag{2.1}$$

The EOF analysis determines the dominant patterns of variability (EOFs) from the geophysical field s by deriving a reduced set of variables, which explains the highest possible variance. To accomplish this reduction, linear combinations of the form

$$\begin{aligned} x_1 &= \mathbf{a}_1'\mathbf{s} \\ x_2 &= \mathbf{a}_2'\mathbf{s} \\ &\vdots \\ x_{N_s} &= \mathbf{a}_{N_s}'\mathbf{s} \end{aligned}$$

are extracted so that x_1 has maximum variance, x_2 has maximum variance among all linear combinations that are uncorrelated with x_1 and so on for all N_s variables. The vectors $\mathbf{a}_i$ representing the EOFs are found by maximizing the expression

$$\langle x_i, x_j \rangle_t = \frac{1}{T}\mathbf{a}_i'\mathbf{S}'\mathbf{S}\mathbf{a}_i = \mathbf{a}_i'\mathbf{C}_{ss}\mathbf{a}_i \qquad \text{for} \qquad i = 1, \ldots, N_s \tag{2.2}$$

subject to the constraints:

$$\mathbf{a}_i'\mathbf{a}_j = \begin{cases} 1 & \text{if } i = j, \\ 0 & \text{if } i \neq j. \end{cases} \tag{2.3}$$

Due to the constraint 2.3, the variance cannot be arbitrarily increased by making the components of vector $\mathbf{a}$ large. The maximization of Equation 2.2 keeping Equation 2.3 in mind leads to an eigenvalue or characteristic value problem:

$$\mathbf{C}_{ss}\mathbf{a}_i = \lambda_i\mathbf{a}_i \qquad \text{or} \qquad (\mathbf{C}_{ss} - \lambda\mathbf{I})\,\mathbf{a}_i = 0. \tag{2.4}$$

The vector $\mathbf{a}_i$ is the eigenvector associated with the eigenvalue λ_i (introduced as a Lagrange multiplier) of the matrix $\mathbf{C}_{ss}$, and $\mathbf{I}$ is the unit matrix of order N_s (Anderson, 1984). The matrix $\Lambda = \lambda\mathbf{I}$ is a diagonal matrix with the eigenvalues λ_i

as diagonal elements. Since the covariance matrix $\mathbf{C}_{ss}$ is symmetric and positive definite, the eigenvalues $\lambda_1, \ldots, \lambda_{N_s}$ are real and positive. Due to the symmetry of $\mathbf{C}_{ss}$, its trace (sum of the diagonal elements c_{ii} of the matrix) is invariant under a basis transformation and, thus, is equal to the sum of the eigenvalues

$$\sum_{i=1}^{N_s} c_{ii} = \sum_{i=1}^{N_s} \lambda_i. \tag{2.5}$$

Each eigenvalue λ_i explains a fraction of the total explained variance of the considered field i.e. $\lambda_i / \sum_{j=1}^{N_s} \lambda_j$. The eigenvectors λ_i are arranged in decreasing order of magnitude so that $\lambda_1 \geq \lambda_2 \geq \ldots \geq \lambda_{N_s}$. Thus, the first mode characterized by λ_1 and the corresponding eigenvector (EOF) $\mathbf{a_1}$ explains the largest fraction of the total variance of the dataset.

Due to the constraint of Equation 2.3, the set of EOFs $\mathbf{a}_1, \ldots, \mathbf{a}_{N_s}$ can be taken as an orthonormal basis in the N_s vector space. Thus, any observation vector $s(t)$ can be expressed as a linear combination of the N_s eigenvectors:

$$\mathbf{s}(t) = \sum_{i=1}^{N_s} x_i(t)\mathbf{a}_i, \tag{2.6}$$

where the coefficients $x_i(t)$ are the expansion coefficients. These coefficients are determined by projections of the data vector on the eigenvector:

$$x_i(t) = \mathbf{a}_i' \mathbf{s}(t) \qquad \text{for} \qquad i = 1, \ldots, N_s. \tag{2.7}$$

The expansion coefficients, also called principal components (PCs), represent the weight of a certain mode $\mathbf{a}_i$ in describing the observations $\mathbf{s}(t)$. Substituting Equation 2.7 for Equation 2.3 reveals that the new variables are uncorrelated and their variance is equal to the corresponding eigenvalue λ_i

$$\langle x_i, x_j \rangle_t = \mathbf{a}_i' \mathbf{C} \mathbf{a}_i = \begin{cases} \lambda_i & \text{if } i = j, \\ 0 & \text{if } i \neq j. \end{cases} \tag{2.8}$$

Subject to the constraint 2.3, the EOFs are the most efficient patterns (in terms of degrees of freedom) to explain the temporal variance, summarized over the total region of analysis.

North's Rule of Thumb

The spatial cross-covariance matrix from which the eigenvalues and EOFs are determined is based on a finite number of realizations. Thus, information of the sampling error of these parameters is very important for the reliability of the

analysis results. North et al. (1982) derived an approximation for the "typical error" of the estimated eigenvalues:

$$\Delta\lambda_i \approx \sqrt{\frac{2}{N}}\lambda_i \tag{2.9}$$

and eigenvectors:

$$\Delta\,\mathbf{a}_i \approx \frac{c\,\Delta\lambda_i}{\lambda_j - \lambda_i}\mathbf{a}_j, \tag{2.10}$$

where c is a constant and N is the number of independent realizations.

North's "Rule of Thumb" follows from approximation 2.10: "If the sampling error of a particular eigenvalue λ is comparable to or larger than the spacing between λ and a neighboring eigenvalue, then the sampling errors for the EOF associated with λ will be comparable to the size of the neighboring EOF". In other words, if the difference between the eigenvalue λ_i and the neighboring eigenvalue λ_j is greater than the sampling error $\Delta\lambda_i$ both eigenvectors will be well separated. Otherwise the corresponding eigenvectors can be mixed and the true eigenvector may be a linear combination of the two EOFs $\mathbf{a}_i$ and $\mathbf{a}_j$.

Physical Interpretation of EOFs

Spatial patterns derived from EOF analysis are the most efficient patterns for explaining the temporal variance integrated over the entire analysis domain within the constraints of being both spatially and temporally orthogonal to each other (Cheng and Dunkerton, 1995). However, the pattern that represents variance most efficiently does not necessarily have anything to do with the underlying dynamical structure. Real world processes do not need to be characterized by orthogonal spatial patterns or uncorrelated temporal indices. Thus, there is no guarantee of an accurate representation of the real physical processes inherent in the input data. Other problems inherent in EOF analysis are that the isolated EOFs are sensitive to the spatial domain, and the sample used for analysis (Richman, 1986; North et al., 1982).

While it is often possible to identify the first EOF with a known physical process, this is much more difficult with the second and higher EOFs. Nevertheless, numerous papers exist which attempt to find a physically plausible interpretation not only of the leading but also of higher modes. For example, Wallace and Gutzler (1981) applied EOF analysis to fields of NH sea level pressure and NH 500-hPa geopotential heights (Wallace and Gutzler, 1981). In a previous study (Perlwitz and Graf, 1995), we determined the leading EOFs of the NH 50-hPa geopotential height fields.

Linear transformation (or rotation) of a subset of leading EOFs, known as *rotated EOF analysis*(e.g. Horel, 1981; Richman, 1986), is often used to obtain regional "simple" patterns that are more physically meaningful and statistically robust. Horel (1981) found that the rotated EOFs of the 500-hPa geopotential field better agree with the teleconnection patterns than the original EOFs. A known application of this approach is the determination of the teleconnection patterns of the NH 700-hPa geopotential height field for each individual month of the year (Barnston and Livezey, 1987). These patterns are used to define the index of different teleconnection patterns, published monthly in the *Climate Diagnostic Bulletin.* The simplicity of patterns are, however, no guarantee of an inherent physical mechanism. Von Storch and Zwiers (1998) demonstrated that features are sometimes split into different patterns due to rotation, even though they are part of the same physical process. Jolliffe (1989) found that the results of EOF rotation are sensitive to the choice of rotation criterion and the normalization of EOFs. Another feature is that information about the dominant sources of variation in the data is lost.

Other multivariate statistical methods can be used to isolate spatial patterns which may have a high physical relevance. Such methods determine the coupled variability modes between the time series of two variables. The prerequisite for such an analysis is knowledge of the physical relationship between both variables. For instance investigation of the coherent variation of geopotential height and SST fields takes into account the interaction between the atmosphere and the underlying ocean (e.g. Wallace et al., 1992). Two methods which can be used to isolate coupled variability modes will be introduced in the next section.

2.1.2 CCA and SVD Analysis

In a review paper Bretherton et al. (1992) discussed *methods of isolating coupled modes of variability between the time series of two fields.* They mainly recommended SVD analysis and *CCA in the phase space of leading EOFs* for the investigation of the relationship between two geophysical datasets. Since its application to geophysical data sets by Glahn (1968), CCA has been broadly used in the atmospheric science (for a review, see Bretherton et al., 1992). SVD has gained an increasing number of applications since its recommendation by Bretherton et al. (1992) and the accompanying paper by Wallace et al. (1992).

Following Bretherton et al. (1992), let us suppose a *left* geophysical field $\mathbf{s} = (s_i, \ldots, s_{N_s})$ and a *right* one $\mathbf{z} = (z_1, \ldots, z_{N_z})$ with N_s and N_z grid points respectively. T observations are given for both random fields. Again, for convenience, it is assumed that $\langle s_i \rangle_t = \langle z_i \rangle_t = 0$ for all i and j. Thus, the two data fields can be viewed as a $T \times N_s$ data matrix $\mathbf{S}$, in which the ith column contains the T observations of s_i, and as a $T \times N_z$ data matrix $\mathbf{Z}$ whose jth column contains the

T observations of z_j.

The indicated sample covariance matrices based on the observations in the two fields are

$$\begin{aligned} \mathbf{C_{ss}} &= \frac{1}{T}\mathbf{S'S} \qquad (N_s \times N_s), \\ \mathbf{C_{zz}} &= \frac{1}{T}\mathbf{Z'Z} \qquad (N_z \times N_z), \\ \mathbf{C_{sz}} &= \frac{1}{T}\mathbf{S'Z} \qquad (N_s \times N_z). \end{aligned}$$

SVD Analysis

SVD analysis is a straightforward expansion of EOF analysis. To find the dominant coupled modes of the variability between the time series of two geophysical fields, s and z, SVD analysis determines linear combinations of the form $u_i = \mathbf{a}_i'\mathbf{s}$ and $v_i = \mathbf{b}_i'\mathbf{z}$ for $i = 1, \ldots, d$, where $d = min(N_s, N_z)$, such that the covariance between the new variables

$$\langle u_i, v_i \rangle_t = \frac{1}{T}\mathbf{a}_i'\mathbf{S'Z}\mathbf{b}_i = \mathbf{a}_i'\mathbf{C}_{sz}\mathbf{b}_i \qquad \text{for} \qquad i = 1, \ldots, d \tag{2.11}$$

is maximized. The constraints for the associated patterns $\mathbf{a}_i$ and $\mathbf{b}_i$ are

$$\mathbf{a}_i'\mathbf{a}_j = \mathbf{b}_i'\mathbf{b}_j = \begin{cases} 1 & \text{if } i = j \\ 0 & \text{if } i \neq j. \end{cases} \tag{2.12}$$

Solving the constrained maximizing problem by using a Lagrange multiplier leads to the following system of equations

$$\begin{aligned} \mathbf{C}_{sz}\mathbf{b}_i &= \sigma\mathbf{a}_i \\ \mathbf{C}_{sz}\mathbf{a}_i &= \sigma\mathbf{b}_i. \end{aligned} \tag{2.13}$$

The solution can be found by substituting the two equations into each other (von Storch and Zwiers, 1998) or by singular value decomposition of the covariance matrix $\mathbf{C}_{sz}$ (Appendix A.2):

$$\mathbf{C}_{sz} = \mathbf{A}\Sigma\mathbf{B}', \tag{2.14}$$

where Σ is a $N_s \times N_z$ matrix whose elements are equal to zero except for the first d diagonal values $\sigma_1, \ldots, \sigma_d$. The first d column vectors of $\mathbf{A}$ and $\mathbf{B}$, the *singular vectors* are the associated patterns $\mathbf{a}_1, \ldots, \mathbf{a}_d$ and $\mathbf{b}_1, \ldots, \mathbf{b}_d$ (Bretherton et al., 1992).

Corresponding to the EOF analysis, the expansion coefficients x_i and y_i, for $i = 1, \ldots, d$ can be determined by projecting the original data onto the eigenvectors of the corresponding field

$$\begin{aligned} x_i &= \mathbf{s}'\mathbf{a}_i \\ y_i &= \mathbf{z}'\mathbf{b}_i. \end{aligned} \tag{2.15}$$

It can be easily shown that

$$Cov\langle u_i, v_i \rangle_t = \sigma_i. \tag{2.16}$$

After arranging the singular values such that ($\sigma_1 \geq \sigma_1 \geq \cdots \geq \sigma_d \geq 0$), the first mode which belongs to the first singular vectors $\mathbf{a}_1$ and $\mathbf{b}_1$ maximizes the covariance of the two fields. The pair of patterns associated with the second singular value explains the maximum amount of covariance subject to the constraint that they are orthogonal to the first pair of patterns (Equation 2.11) and so on.

In contrast to the EOF analysis, in which the total variance of a data field is invariant under a basis transformation (Equation 2.5), the total covariance between the two fields is not a constant in this statistical approach. As a benchmark for comparison, however, the squared covariance fraction (SCF) can be used (Bretherton et al., 1992):

$$\mathrm{SFC}_i = \frac{\sigma_i^2}{\sum_{k=1}^{d} \sigma_k^2}. \tag{2.17}$$

Another property of the SVD analysis is that the expansion coefficients belonging to each field are generally correlated. For $i \neq j$ is

$$\begin{aligned} \mathrm{r}\,[x_i, x_j]_t &\neq 0 \\ \mathrm{r}\,[y_i, y_j]_t &\neq 0. \end{aligned} \tag{2.18}$$

in which $\mathrm{r}[x_i, x_j]_t$ denotes the correlation coefficient between the time series x_i and x_j.

The same limitation exists for the physical interpretation of higher SVD modes and for higher EOF modes because of the constraints of spatial orthogonality of the singular patterns. Cheng and Dunkerton (1995) introduced an approach for the rotation of the leading singular patterns. This method relaxes the spatial orthogonality similar to the rotation of EOFs.

CCA

CCA analysis is a technique that isolates the linear combination of data in the left field and the linear combination of data in the right field that have the maximum

correlation coefficient (Bretherton et al., 1992). There are two mathematical approaches to CCA. The classical approach, developed by Hotelling (1936) was applied to geophysical data by Glahn (1968) and Nicholls (1987). In the other developed by Barnett and Preisendorfer (1987), the time series of each field are first filtered by projection onto a leading subset of its EOFs. Then, the new variables having maximum correlation are calculated from the temporal projection coefficient (principal components of the leading EOFs) of the two fields.

The Classical Approach to CCA

To find the dominant coupled modes of the variability between the time series of the two geophysical fields $\mathbf{s}$ and $\mathbf{z}$, CCA isolates linear combinations of the form

$$u_i = \mathbf{p}_i'\mathbf{s} \qquad \text{and} \qquad v_i = \mathbf{q}_i'\mathbf{z} \tag{2.19}$$

for $i = 1, \ldots, d$, where $d = min(N_s, N_z)$, such that u_1 and v_1 have maximum sample correlation r_1. The pair u_2 and v_2 have maximum sample correlation subject to the restriction that u_2 is uncorrelated with u_1 and v_2 is uncorrelated with v_1, and so on for all $i = 1, \ldots, d$ pairs. The new variables u_i and v_i are called canonical variables, the weight vectors $\mathbf{p}_i$ and $\mathbf{q}_i$ are the ith canonical vectors, and r_i is the ith canonical correlation coefficient. The canonical vectors $\mathbf{p}_i$ and $\mathbf{q}_i$ are found by solving the following maximization problem:

$$r_i = r[u_i, v_i]_t = \mathbf{p}_i'\mathbf{C}_{sz}\mathbf{q}_i' = max, \tag{2.20}$$

under the constraint:

$$\langle u_i, u_i \rangle_t = \langle v_i, v_i \rangle_t = \mathbf{p}_i'\mathbf{C}_{ss}\mathbf{p}_i = \mathbf{q}_i'\mathbf{C}_{zz}\mathbf{q}_i = 1 \qquad \text{for} \qquad i = 1, \ldots, d. \tag{2.21}$$

The correlation of a multiple of u_i and a multiple of v_i is the same as the correlation of u_i and v_i. Therefore, it is possible to normalize the weights $\mathbf{p}_i$ and $\mathbf{q}_i$ so that u_i and v_i have unit variance (Equation 2.21). The appearance of these constraints can be simplified by defining *normalized* weight vectors $\hat{\mathbf{p}}$ and $\hat{\mathbf{q}}$ such that

$$\begin{aligned} \mathbf{p}_i &= \mathbf{C}_{ss}^{-1/2}\hat{\mathbf{p}}, \\ \mathbf{q}_i &= \mathbf{C}_{zz}^{-1/2}\hat{\mathbf{q}}. \end{aligned} \tag{2.22}$$

Inserting Equations 2.22 into the maximization problem (Equations 2.20 and 2.21) leads to the following equivalent maximization problem:

$$\hat{\mathbf{p}}'\hat{\mathbf{U}}\hat{\mathbf{q}} = max, \qquad \hat{\mathbf{M}} = \mathbf{C}_{ss}^{-1/2}\mathbf{C}_{sz}\mathbf{C}_{zz}^{-1/2} \tag{2.23}$$

with

$$\hat{\mathbf{p}}'\hat{\mathbf{p}} = \hat{\mathbf{q}}'\hat{\mathbf{q}} = 1. \tag{2.24}$$

This simplified problem has the same form as the original maximization problem and can be solved using SVD (Appendix A.2) of $\hat{\mathbf{M}}$ (Nicholls, 1987; Bretherton et al., 1992):

$$\hat{\mathbf{M}} = \mathbf{C}_{ss}^{-1/2}\mathbf{C}_{sz}\mathbf{C}_{zz}^{-1/2} = \hat{\mathbf{P}}\Sigma\hat{\mathbf{Q}}'. \tag{2.25}$$

where the ith columns of $\mathbf{P} = \mathbf{C}_{ss}^{-1/2}\hat{\mathbf{P}}$ and $\mathbf{Q} = \mathbf{C}_{zz}^{-1/2}\hat{\mathbf{Q}}$ contain the ith pair of canonical vectors and the ith diagonal element of the diagonal matrix Σ contains the square of the ith canonical correlation coefficient. The canonical variables or expansion coefficients u_i and v_i are determined by projection of the data vectors onto the weight vectors (Equations 2.19).

CCA in the Phase Space of Leading EOFs

In many geophysical applications the number of observations is less than the number of grid points in the spatial fields. In this case, the matrices $\mathbf{C_{ss}}$ and $\mathbf{C_{zz}}$ are not invertible. To avoid the above mentioned problem, Barnett and Preisendorfer (1987) supposed a prefiltering of the two data fields by retaining only the projection of each field on a subset of its EOFs before applying CCA. If all EOFs are retained, the results of this method are identical to those of classical CCA (Bretherton et al., 1992).

Decomposing the fields $\mathbf{s}$ and $\mathbf{z}$ into their truncated principal components (Equation 2.7) gives

$$\begin{aligned} \mathbf{s}(t) &= \sum_{i=1}^{N_s} \lambda_i^{1/2}\xi_i(t)\mathbf{a}_i \\ \mathbf{z}(t) &= \sum_{i=1}^{N_z} \kappa_i^{1/2}\upsilon_i(t)\mathbf{b}_i, \end{aligned} \tag{2.26}$$

where ξ_i and υ_i are the normalized principal components

$$\xi_i(t) = \lambda_i^{-1/2}x_i(t) \qquad \text{and} \qquad \upsilon_i(t) = \kappa_i^{-1/2}y_i(t). \tag{2.27}$$

The temporal orthonormality of the normalized expansion coefficients of CCA guarantees that

$$\begin{aligned} \mathbf{C}_{\xi\xi} &= \mathbf{I} \\ \mathbf{C}_{\upsilon\upsilon} &= \mathbf{I}. \end{aligned}$$

Hence, in the EOF subspace, CCA reduces to find the SVD of $\mathbf{C}_{\xi\upsilon} = \hat{\mathbf{L}}\Lambda\hat{\mathbf{R}}'$. The left and right canonical vectors are just the left and right column vectors $\hat{\mathbf{l}}$ and $\hat{\mathbf{r}}$ of the matrices $\hat{\mathbf{L}}$ and $\hat{\mathbf{R}}$. The expansion coefficients are then found by projecting

the field of the EOF subspace onto these canonical vectors:

$$u_k(t) = \mathbf{l}_k \xi(t) \tag{2.28}$$

$$v_k(t) = \mathbf{r}_k \upsilon(t). \tag{2.29}$$

The expansion coefficients are orthonormal. The weight vectors from the original grid point base can be found by

$$\mathbf{p}_k = \mathbf{S} u_k \tag{2.30}$$

$$\mathbf{q}_k = \mathbf{Z} v_k. \tag{2.31}$$

After transformation back into the original grid point base, the canonical vectors are no longer orthogonal.

CCA or SVD Analysis?

Both SVD analysis and CCA in the phase space of leading EOFs were recommended for isolating coupled modes of variability (Bretherton et al., 1992). Cherry (1996) made clear that both techniques have different analytical goals. CCA identifies spatial patterns by maximizing the temporal correlation between two fields. Thus, CCA may be used when the correlation structure is important. SVD analysis between-field cross-covariance part of the combined covariance matrix and may be appropriate when it is covariance that is of interest. This information is obscured by CCA.

We used SVD analysis for the investigation of the coherent covariance structure between tropospheric and stratospheric circulation. This method was applied to the time series of monthly or winter mean time series of the 50- and 500-hPa geopotential heights. The SVD analysis results of the simultaneous time series of the two fields cannot used for the interpretation of the direction of the relationship. To study the influence of tropospheric circulation on the circulation of the lower stratosphere and vice versa, we applied CCA as a lag-correlation technique. We analyzed daily data of the 50- and 500-hPa geopotential height fields, in which the time series of one field was lagged relative to the time series of the other field. In this way, we found out the time lag at which the maximum correlation between the time series of both fields exists.

Newman and Sardeshmukh (1995) argued that SVD analysis is capable of detecting coupled modes only under very special circumstances because of the orthogonality constraints of the maximizing procedure (Equation 2.12). Cherry (1996) showed that, in general, both methods have a high chance of producing spurious patterns and correlations. This chance is increased when small samples or autocorrelated time series are used.

Interpretation of Results

The measure which illustrates the degree of the relationship described by the associated patterns of a coupled mode is the correlation coefficient between the expansion coefficients $r[u_k, v_k]$. In CCA, this measure is maximized.

Various kinds of maps can be defined to simplify the physical interpretation of the statistical results of CCA and SVD analysis. Once the expansion coefficients u_k and v_k are obtained, two types of correlation maps - the *homogeneous* and the *heterogeneous correlation maps* - can be generated (Bretherton et al., 1992). The kth left homogeneous correlation map is defined as the vector of correlations $r[s, u_k]_t$ between the grid point values of the left field s and the kth left expansion coefficient u_k. This map is a useful indicator of the geographical localization of the covarying part of the left field of the respective mode. The kth left heterogeneous correlation map $r[s, v_k]_t$ is defined as the correlation coefficient between the grid point values of the left field with the expansion coefficients of the right field v_k. This map indicates how well the grid points in the left field can be predicted by the knowledge of the kth right expansion coefficients. The squared correlation coefficients in [%] are a measure of the explained fraction of variance which is locally explained by the respective expansion coefficient. With an interchange of left and right, an analogue description for the right patterns is given.

In parallel, one may also define homogeneous and heterogeneous regression maps. An overview of the mathematical description of the regression maps is given in Table 2.1. The time series of the anomaly fields are regressed to the standardized index time series (temporal expansion coefficients). These regression maps have the same units as the anomaly fields itself because the standardized index time series are dimensionless. Therefore, the amplitudes shown in the regression maps correspond to anomaly values in that field, which occur in association with the index time series anomaly of one standard deviation. Thus, this amplitude can be considered as the typical strength of the amplitude in relation to the index time series studied.

Often, multivariate statistical methods are applied to data on a regular grid like a $5° \times 5°$ grid. In general (as in EOF analysis, CCA, SVD analysis) the grid-point time series are weighted with the square root of the cosine of the latitude before the covariance matrix is determined. This takes into account that the area represented by a grid point decreases with increasing latitude. Non-weighted time series at the grid points are used in the regression maps.

Table 2.1. Overview of the mathematical description of the homogeneous and heterogeneous regression maps as determined on the basis of CCA and SVD analysis.

	SVD analysis		CCA	
	left field	right field	left field	right field
homogeneous maps	$\frac{1}{\sigma_{u_k}}\mathbf{C}_{ss}u_k$ [a]	$\frac{1}{\sigma_{v_k}}\mathbf{C}_{zz}v_k$ [a]	p_k	q_k
heterogeneous maps	$\frac{\delta_k}{\sigma_{v_k}}u_k$ [b]	$\frac{\delta_k}{\sigma_{u_k}}v_k$ [b]	$r_k p_k$ [c]	$r_k q_k$ [c]

[a] σ_{u_k} and σ_{v_k} are the standard deviation of the kth left and right temporal expansion coefficient, respectively.

[b] The heterogeneous patterns are proportional to the corresponding singular patterns. This is not valid for the homogeneous pattern.

[c] Homogeneous and heterogeneous patterns are proportional in the respective fields.

2.2 SWAN - a Statistical-Dynamic Approach

A principal goal of this thesis is to isolate statistically relevant features, which describe the processes of dynamical coupling between troposphere and stratosphere. A new approach is introduced which uses theoretical knowledge of this coupling to apply statistical methods to observational data. In the following, theoretical aspects of the troposphere/stratosphere coupling are described (Section 2.2.1) and the concept of SWAN and its applications are presented (Section 2.2.2).

2.2.1 Theoretical Aspects

Concept of Eulerian average

Averaging observational data in various ways is a standard approach for handling the complexity of global scale atmospheric flow. Straightforward averages over a set of points fixed in space or time are known as *Eulerian average*. Given any particular average, one can define the deviations or departure of each atmospheric

variable from its mean value. These disturbances are often known as *wave* or *eddy* quantities. Averaging not only allows compressing of the volume of information but improves the statistical reliability. A suitable framework for the diagnosis and interpretation of atmospheric quantities has also been developed that separates *mean state* and *wave* parts. Owing to the nonlinearity of the equations of motion, there is, in general, a mutual coupling between waves and mean state. Thus, the configuration of the mean flow can strongly influence the propagation of waves, for example through the refraction of the wave, while the disturbances themselves can bring about significant mean flow changes through rectified nonlinear effects (e.g. by breaking of waves).

The theoretical framework providing qualitative physical insights into the two-way process of wave-mean flow interaction has most satisfactorily been constructed for zonal mean average. We introduce the (Eulerian) zonal average of any quantity $\Psi(\lambda, \phi, z, t)$, denoted by an overbar

$$\bar{\Psi}(\phi, z, t) = (2\pi)^{-1} \int_0^{2\pi} \Psi(\lambda, \phi, z, t)\, d\lambda, \tag{2.32}$$

and the departure from the average, denoted by a prime:

$$\Psi'(\lambda, \phi, z, t) = \Psi - \bar{\Psi}. \tag{2.33}$$

λ, ϕ, z and t are longitude, latitude, height and time, respectively.

Charney-Drazin Theorem and Evidence of Observation

The most important processes which dynamically link troposphere and stratosphere are the vertical propagation of Rossby waves into the stratosphere and their interaction with the mean stratospheric flow. However, there are critical parameters for the vertical propagation of these waves. These parameters are the horizontal scale of the waves and the mean zonal wind distribution in the stratosphere. Using the quasi-geostrophic theory on a β-plane, Charney and Drazin (1961) showed that planetary waves can propagate vertically provided that their phase speeds c are westward relative to the zonal mean flow $\bar{u}$:

$$0 < \bar{u} - c < \bar{u}_c \equiv \beta[(k^2 + l^2) + f_0^2/(4H^2N^2))]^{-1}, \tag{2.34}$$

with

$$\beta = 2\Omega \cos\phi \qquad \text{and} \qquad f_0 = 2\Omega \sin\phi. \tag{2.35}$$

H, N and u are the scale height, the Brunt–Väisälä frequency and the zonal velocity, respectively. $\Omega = 7.292 \times 10^{-5} \mathrm{s}^{-1}$ is the earth's rotation rate. The zonal and meridional wave lengths are defined by $2\pi k^{-1}$ and $2\pi l^{-1}$, respectively. $\bar{u}_c$

is called *Rossby critical velocity.* Equation 2.34 reveals that $\bar{u}_c$ decreases with increasing horizontal wave number. The waves having the largest amplitudes are stationary with respect to the ground, i.e. $c = 0$. Hence, there is $0 < \bar{u} < \bar{u}_c$. Andrews et al. (1987) illustrated that for typical stratospheric stability ($N^2 = 5 \times 10^{-4}\mathrm{s}^{-}2$), and choosing $l = \pi/(10,000\,\mathrm{km})$, $\bar{u}_c$ at 60°N is given by:

$$\bar{u}_c \approx 110/(s^2 + 3)\,\mathrm{m\,s^{-1}}, \tag{2.36}$$

where the integer $s = k\,a\,cos\phi$ is the spherical zonal wave number. Using this simple model, the Rossby critical velocities for the ZWNs 1 and 2 amount to 28 $\mathrm{m\,s^{-1}}$ and 16 $\mathrm{m\,s^{-1}}$, respectively.

The *Charney-Drazin Theorem* (Equation 2.34) gives a theoretical explanation for numerous observational phenomena although the model used for the deviation of the theorem (constant $\bar{u}$ and N) is un-realistic and the actual critical velocity may be larger than indicated by the β-plane theory:

- The window of the zonal mean flow for the propagation of tropospheric disturbances becomes smaller as the zonal wave number s increases. As a consequence, the stratosphere and upper troposphere has a strong filter effect on tropospheric disturbances since zonal westwind normally increases with height. Only ultra-long planetary waves generated by diabatic heating and orography can propagate into the stratosphere.

- Radiatively caused, the stratospheric zonal mean flow alternates between easterlies in the summer hemisphere and westerlies in the winter hemisphere. This fact is an essential condition for whether a dynamical coupling between both atmospheric layers exists. Only in the winter hemisphere can ultra-long planetary waves propagate into the stratosphere and interact with the mean stratospheric flow. During the summer season ($\bar{u} < 0$), the dynamical coupling between troposphere and stratosphere is strongly reduced because the waves are trapped in the troposphere.

- The dynamical coupling between troposphere and stratosphere is stronger in the boreal than in the austral winter hemisphere. The reason for this is that the wave forcing by both diabatic heating and orography is only weak at Southern Hemisphere (SH) mid-latitudes where there is mainly ocean.

Eliassen Palm Flux

Andrews and McIntyre (1976) introduced the *transformed Eulerian mean* (TEM) formulation of the zonal mean quasi-geostrophic equations which shows clearly the interaction between eddy forcing and the mean state. The basic concept of

wave-mean flow interaction will now be described. We denote the zonal, meridional and vertical component of the velocity vector as u, v and w, respectively. The TEM equations are based on the definition of the *residual circulation* $(\bar{v}^*, \bar{w}^*)$. Following the definitions of Kanzawa (1982) the components of the residual circulation in spherical coordinates $(\lambda, \phi, z = -H \ln p/p_s)$ are given by

$$\bar{v}^* = \bar{v} - \frac{1}{\rho_0}\frac{\partial}{\partial z}(\rho_0 \overline{v'\Phi'_z}/N^2) \tag{2.37}$$

$$\bar{w}^* = \bar{w} + \frac{1}{a\cos\phi}\frac{\partial}{\partial \phi}(\cos\phi \overline{v\Phi'_z}/N^2), \tag{2.38}$$

where Φ, a and ρ_0 are the geopotential, the Earth's radius and the basic density respectively.

The zonal mean quasi-geostrophic equations can be transformed into:

$$\frac{\partial \bar{u}}{\partial t} - f\bar{v}^* = \frac{1}{\rho_0 a \cos\phi}\nabla \cdot \mathbf{F} \tag{2.39}$$

$$\frac{\partial \bar{\Phi}_z}{\partial t} + N^2\bar{w}^* = 0 \tag{2.40}$$

$$\frac{1}{a\cos\phi}\frac{\partial \bar{v}^*\cos\phi}{\partial\phi} + \frac{1}{\rho_0}\frac{\partial \rho_0 \bar{w}^*}{\partial z} = 0. \tag{2.41}$$

The vector $\mathbf{F} \equiv (0, F^{(\phi)}, F^{(z)})$ is known as the Eliassen-Palm flux (E-P flux); its components are given by

$$F^{(\phi)} = -\rho_0(z)\, a\, \cos\phi\, \overline{u'v'} \tag{2.42}$$

$$F^{(z)} = \rho_0(z)\, a\, \cos\phi\, (f/N^2)\, \overline{v'\Phi'_z}. \tag{2.43}$$

From a theoretical point of view we can interpret $\mathbf{F}$ as westward angular wave moment flow propagating through westerly flow and $\nabla\cdot\mathbf{F}$ as wave-induced torque per unit volume acting on the mean flow (Kanzawa, 1982). In the transformed formalism, the non-acceleration theorem for steady linear waves on a basic zonal flow $\bar{u}(\phi, z)$ with no frictional or diabatic effects is reduced to $\nabla\cdot\mathbf{F} = \mathbf{0}$ (Eliassen and Palm, 1961). To see the effect of waves on the temporal change of the zonal mean wind $\partial\bar{u}/\partial t$, we define D_{F} as

$$D_{\mathrm{F}} = \frac{1}{\rho_0 a \cos\phi}\nabla \cdot \mathbf{F}. \tag{2.44}$$

Then, we can rewrite Equation 2.39 as

$$\frac{\partial \bar{u}}{\partial t} - f\bar{v}^* = D_{\mathrm{F}}. \tag{2.45}$$

Hence, D_{F} can be regarded as a zonal force per unit mass acting on the mean state. If the divergence is positive (negative), there is an acceleration (deceleration) of the mean flow.

2.2.2 SWAN

Concept

At a specific latitude, the decomposition of the longitudinal geopotential height fields $z(\lambda)$ in their Fourier harmonics $s = 1, \ldots, S$ is given as follows:

$$z(\lambda) = \sum_{s=1}^{S} \alpha_s \sin s\lambda + \beta_s \cos s\lambda. \tag{2.46}$$

in which ZWN S represents the limit of data resolution. The amplitude A_s and the phase ψ_s of waves of ZWN s are given by $A_s = \sqrt{{\alpha_s}^2 + {\beta_s}^2}$ and $\psi_s = \arctan(\alpha_s/\beta_s)$. The phase is defined as the longitude of the first maximum eastward of the Greenwich meridian. The recomposed geopotential height field $z_s(\lambda, \phi, t)$ of a single planetary wave with ZWN s is given as

$$z_s(\lambda, \phi, t) = \alpha_s(\phi, t) \cos s\lambda + \beta_s(\phi, t) \sin s\lambda, \tag{2.47}$$

in which the total field is received by $z(\lambda, \phi, t) = \sum_{s=1}^{S} z_s(\lambda, \phi, t)$.

The main implication of the Charney-Drazin Theorem for our understanding of the dynamical coupling between troposphere and stratosphere is as follows: Vertically propagating waves are selectively reflected at levels of supercritical velocity. This critical Rossby velocity decreases with increasing ZWN. Hence, the treatment of single wave fields z_s for $s = 1, 2 \ldots$ seperately is a *proper approach* for studying relevant features of dynamical interaction between troposphere and stratosphere. Clearly, ultra-long planetary waves are primarily involved. The following approach which is physically encouraged by this Theorem is called Single Wave Analysis: *The study of the relationships between tropospheric and stratospheric single waves applying statistical methods.*

Applications

SWAN can be applied to investigate processes concerning the interaction of tropospheric waves and the mean stratospheric flow like the upward and downward propagation of wave-like disturbances or the relationship between the strength of the stratospheric polar winter vortex and single tropospheric waves.

Randel (1987) studied the propagation characteristics of ultra-long planetary waves applying the cross-spectral correlation analysis to individual zonal waves of ZWNs 1, 2 and 3 of geopotential heights. This study clearly follows the SWAN concept.

In this thesis, we will apply CCA (Section 2.1.2) in lag-correlation technique to observational data in order to isolate relevant features of the dynamical interaction between tropospheric and stratospheric circulation. The up- and downward propagation of single planetary waves of ZWN 1 and 2 will be addressed in Chapter 5. The relationship between the strength of the stratospheric polar winter vortex and single tropospheric waves is discussed in Chapter 6. For the physical interpretation of the CCA results, we take into account that the propagation of wave energy in vertical and meridional direction is accompanied by a longitudinal phase shift. The tilt in vertical and meridional direction of planetary waves of a specific ZWN can be used to recognize this physical process in associated anomaly patterns, isolated by CCA. The up- and downward propagation of wave anomalies is related to a west- and eastward tilt of waves with increasing height, respectively (e.g., James, 1994, page 195). A west- and eastward tilt of the waves with increasing latitude characterizes pole- and equatorward propagation, respectively (e.g., Kodera and Chiba, 1995).

Another diagnostic tool utilizing the SWAN concept concerns the vertical propagation of stationary waves in the meridional plane in terms of the E-P flux $\mathbf{F}$. The contributions to $\mathbf{F}$ from the different Fourier harmonics are given as follows (Andrews et al., 1987, pages 231–235):

$$\mathbf{F} = \frac{1}{2}\rho_0 \sum_{s=1}^{S} s A_s^2 \left(0, \frac{1}{f^2 a}\frac{\partial \psi_s}{\partial \phi}, \frac{1}{N^2}\frac{\partial \psi_s}{\partial z}\right). \tag{2.48}$$

This quasi-geostrophic version of the E-P flux $\mathbf{F}$ (Equation 2.48) indicates that the contributions to $\mathrm{F}^{(\phi)}$ and $\mathrm{F}^{(z)}$ from each harmonic depend on the square of the amplitude and the latitudinal and vertical derivatives of the phase of that harmonic. The different Fourier components contribute additively to $\mathbf{F}$, since products of terms of differing ZWNs vanish in the zonal mean.

We use the ZWN decomposition of the E-P Flux to illustrate differences in the vertical propagation of single waves of ZWN 1 and 2 between composites characterized either by an anomalously strong or by an anomalously weak polar winter vortex (Chapter 8).

Chapter 3

Reliability of Statistical Results using NCEP Reanalyses

3.1 Introduction

Most of our present knowledge of the physical and dynamical structure of the atmosphere is based on *in situ* observations of the state of the surface and upper air, and by radiance measurements from satellites. Long-term homogeneous datasets are very important for testing theories, monitoring climate and validating climate models used for the prediction of future climate.

Global analyses of the atmospheric state are produced using a four-dimensional data assimilation system in which multivariate observed data are combined with the 'first guess' of a weather forecast model using a statistical optimization. The first guess is the best estimate of the current state of the atmosphere from previous analyses produced using a numerical weather prediction model. A principal advantage of global analyses in comparison to traditional observations is that atmospheric GCMs are an integral component of the analysis system, which enables a wide range of observational data to be used. However, operational analyses are mainly performed for weather prediction and not for climate purposes. Thus, these datasets are inhomogeneous because of changes in both the weather prediction model (e.g., their horizontal resolution) and data handling techniques (Trenberth, 1995). Therefore, strong efforts have been made to *reanalyze* observations using a frozen state-of-the-art analysis/forecast system. An additional advantage of reanalyses is that data which were not available at the time of operational analyses can be included. Reanalyses have been carried out by the European Centre for Medium-range Weather Forecasts (ECMWF), by NCEP in collaboration with the National Center for Atmospheric Research (NCAR), and

by the Goddard Space Flight Centre (GSFC) in cooperation with the Data Assimilation Office (DAO). The longest is the NCEP/NCAR reanalyses covering the period from 1948 to the present.

Large spurious variations in operational analyses which arise from modifications in the atmospheric circulation model and in the assimilation systems are avoided in the NCEP datasets. However, effects from the varying observational data sources are still possible. For instance, systematic observations of the NH stratosphere by rawinsondes only date back to the International Geophysical Year (IGY), 1957/58. The utilization of satellite sounding data for the reanalyses began in March 1975. Data from Tiros Operational Vertical Sounder (TOVS) has been used since January 1979 (Kalnay et al., 1996). It was recognized that a positive shift of NCEP atmospheric temperatures in 1978-1979 is related to the begin of the incorporation of TOVS data into the reanalysis system (Leder et al., 1998). This change is most pronounced in the tropics at the 100- and 150-hPa levels, where the increase is higher than the intraannual and interannual variability of the zonal mean temperature (Figure 3.1). Leder et al. (1998) compared the equatorial temperature at the 100-hPa level of the NCEP reanalyses and with an independent long-term dataset from the Free University of Berlin (FUB). They showed that the NCEP temperatures are lower than the FUB temperatures before 1979 and higher than the FUB temperatures after this year (Figure 3.2). As a result, the NCEP data exhibit a statistically significant temperature increase whereas the long-term linear trend in the FUB dataset is negative.

Leder et al. (1998) also compared the 30-hPa temperatures at high latitudes. During the cold season, the zonal mean temperature over the Arctic in the NCEP reanalyses agrees very well with the FUB dataset (e.g., in March as indicated by Figure 3.3a). During the summer season, in contrast, the time series of the zonal mean temperatures of both datasets clearly differ (e.g., June as shown in Figure 3.3b). Before incorporating the satellite data, the NCEP reanalyses are several degrees lower than the FUB temperatures. As a result, the NCEP temperatures exhibit a strong positive trend, whereas the FUB temperatures indicate a temperature decrease.

Increasing attention has being payed to the change in atmospheric circulation observed in recent decades (Graf et al., 1995; Kodera and Koide, 1997; Thompson and Wallace, 1998; Thompson et al., 2000; Perlwitz and Graf, 1995). Here, we investigate to what extent the NCEP dataset can be used for studying climate change in stratospheric circulation. After describing the datasets, we will address the question whether SH reanalysis data in the period before the incorporation of satellite data and NH data before the IGY can be included in long-term climate change studies (Section 3.3). It will be shown how the lack of observations in the stratosphere affects the reanalyses data there.

NH geopotential heights at the 50-hPa level will be investigated in more detail by

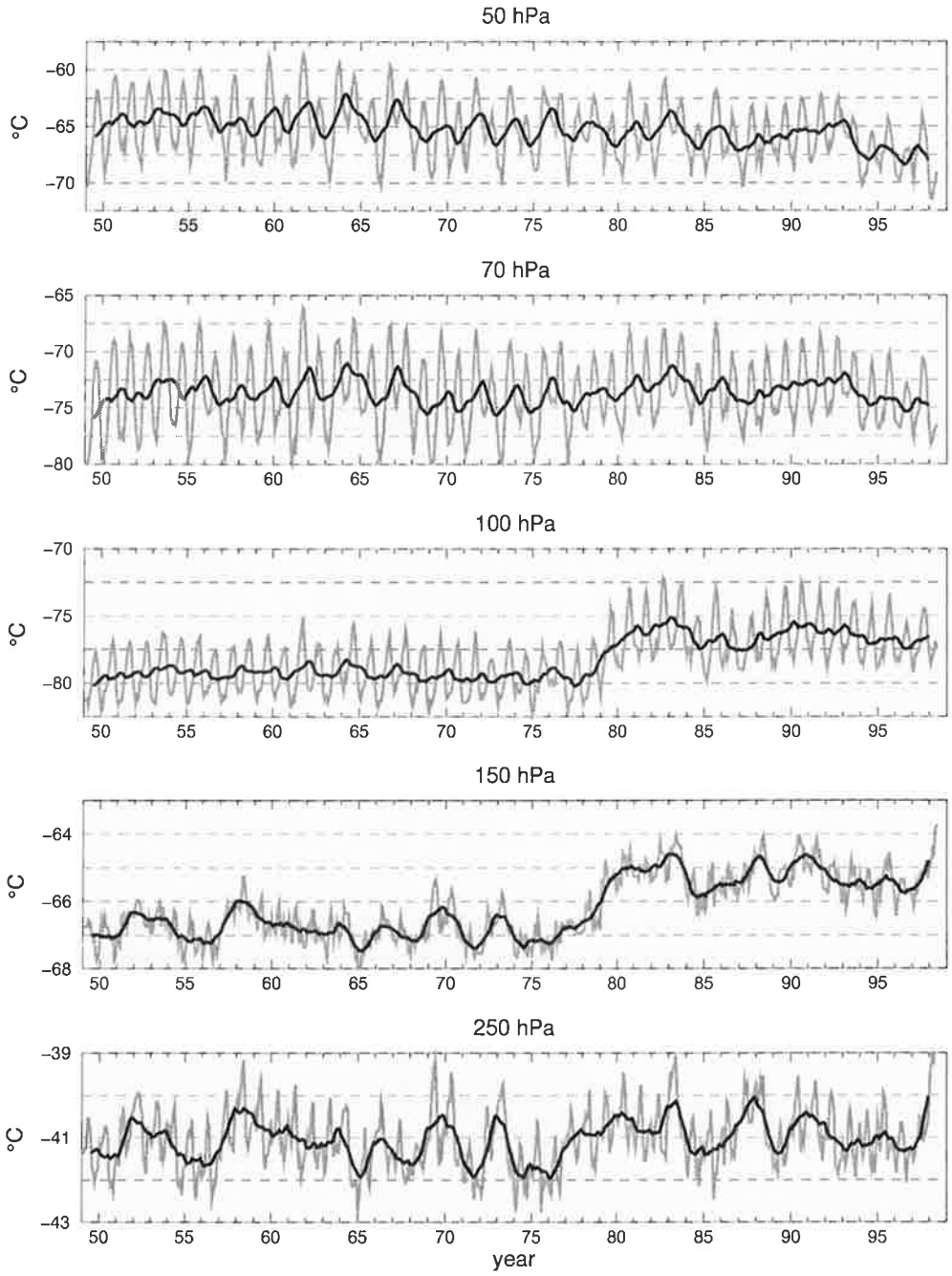

Figure 3.1. Monthly mean zonally averaged temperature at 0°N and running average over 12 months (dark line) at different pressure levels, determined from NCEP reanalyses.

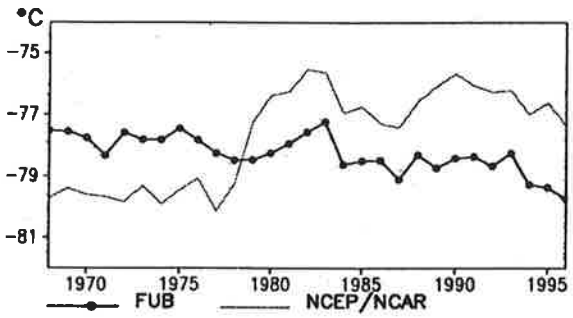

Figure 3.2. Annual mean temperature time series at the equator at 100-hPa (from Leder et al., 1998, Figure 6)

comparing the temporal behaviors of the zonal mean heights from the NCEP and FUB datasets (Section 3.4). We are also interested in the modes of coupled variability of tropospheric and stratospheric circulation and their temporal behavior. To isolate these coupled modes, SVD analysis was applied to the time series of the 50- and 500-hPa geopotential heights. Here, we have used the 50-hPa heights in the FUB analyses and the 500-hPa heights in the operational analyses carried out at the National Center of Meteorology (NMC) of the United States to test the reliability of the SVD results based on the NCEP dataset (Section 3.5).

3.2 Datasets

NCEP Reanalyses

A description of the reanalyses project of NCEP and the National Center for Atmospheric Research (NCAR) was given by Kalnay et al. (1996). The data assimilation and the model design are identical to the system implemented operationally at NCEP on 10 January 1995 (Kanamitsu, 1989; Kanamitsu et al., 1991), except that the horizontal resolution is T62 (about 210 km). The number of vertical levels is 28, and the upper boundary level is at 2.7 hPa. A comparison of reanalyses of the tropical stratosphere was done by Pawson and Fiorino (1998a,b, 1999). The preprocessed data at the pressure levels are available on a regular 2.5° × 2.5° grid at 17 levels, with six pressure levels in the stratosphere (100-, 70-, 50-, 30-, 20- and 10-hPa).

FUB Analyses

Long-term datasets of stratospheric temperatures and geopotential heights are provided by the Stratospheric Research Group of the Free University of Berlin.

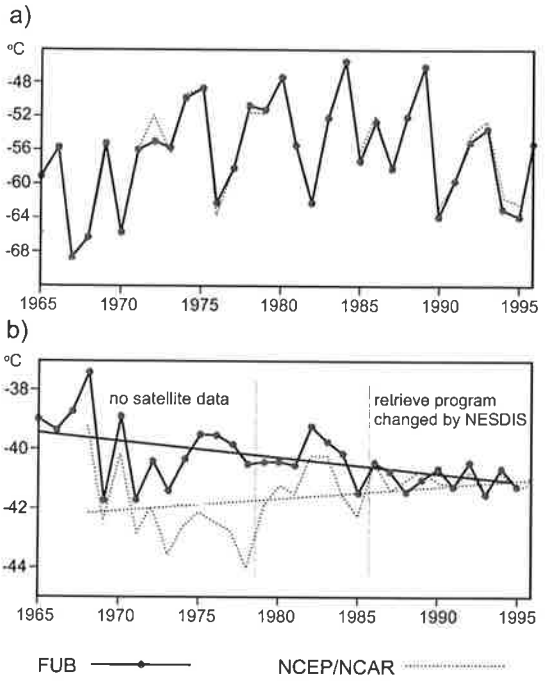

Figure 3.3. Zonally averaged temperature at 30-hPa at 80°N for (a) March and (b) June (from Leder et al. (1998), Figure 3.)

These datasets are based on subjective analyses derived from rawinsonde data. For the NH, daily analyses at 50, 30 and 10 hPa and monthly data at 100 hPa are available. Pawson et al. (1993) published a comprehensive climatology of these analyses.

The 50-hPa geopotential heights used for our comparison cover the period 1958-1998. The long-term analyses of the NH are available on a 10° × 10° grid north of 10°N. At 80°N, the longitude interval is 20°.

The FUB datasets are based on rawinsonde measurements. Rawinsonde observations were first made for weather forecasting. The instrument, however, was not designed to operate in a way that guarantees a homogeneous climate record. Sources of inhomogeneities are changes in both calibration and characteristics of the sondes. Studies show that these problems strongly affect moisture measurements (Trenberth, 1995). In addition, the data quality differs for individual measurements and primary analyses. In the past, the latter had a strong subjective factor. Today, the primary analyses are carried out more objectively by computer programs. A major change affecting all analyses of geopotential height was the change in the value of acceleration due to gravity used in 1990 (Trenberth, 1995).

NMC Operational Analyses

We have used the NMC 500-hPa geopotential heights based on operational analyses from 1958 to 1998. The dataset is available[1] on a $5° \times 5°$-grid north of 20°N. We call the dataset *NMC operational analyses*. This dataset may be affected by modification of both the data assimilation system and the weather prediction model.

3.3 Effects of the Lack of Observational Data

SH Temperatures of the Lower Stratosphere Before 1978

A long-term independent hemispheric scale dataset of stratospheric temperatures is not available for the SH because the coverage rawinsonde station in the SH was very small. Thus, an assessment of the usefulness of the NCEP temperature data is more difficult. Angell (1986) published annual mean temperature trends of the lower SH stratosphere covering the period 1965–1985 on the basis of rawinsonde data from a few stations. The temperatures were derived from the 100-50-hPa layer thickness. A significant SH-mean temperature change of −0.37 K per decade (K/dec) in the lower stratosphere was found. The magnitude of this decrease is larger than 0.5 K/dec both in the tropics and at 75°S.

We calculated the annual means of the 100-50-hPa layer thickness using the NCEP dataset. The corresponding layer-mean temperatures are area-averaged over the SH extratropics (south of 30°S). In contrast to the results of Angell (1986), we found that neither the annual mean temperature of the SH extratropics (Figure 3.4a) nor the temperature at 75°S (Figure 3.4c) show a negative trend in the lower stratosphere during the period 1965–1985. We conclude that the NCEP SH stratospheric data for the period before the incorporation of satellite data (1949–1978) should not be included in climate change studies.

NH Temperatures of the Lower Stratosphere Before the IGY

We found a significant cooling in the extra-tropical lower stratosphere of the NH for the period 1958–1999 (Figure 3.4b). This change in the NCEP data agrees very well with the results of trend studies using rawinsonde data (Angell, 1986; Graf et al., 1998). It is impossible to validate the increase in extratropical mean temperature of the lower stratosphere for the period 1949–1958 shown by the NCEP data. This short-term increase in contradiction to the long-term decrease

[1] (http://www.scd.ucar.edu/dss/datasets/ds085.1.html)

starting in the IGY, may be spurious for the following reason. Atmospheric GCMs tend to have a polar cold bias at lower stratospheric levels. When the spatial coverage of rawinsonde data is poor or observations of the stratosphere do not exist at all, the temperature will be close to this characteristic *cold* model state. The assimilation of hemispheric scale temperature and wind distribution given by the rawinsonde network since the IGY appears as a shift of stratospheric temperatures in the reanalyses towards more realistic (warmer) values. Therefore, we do not recommend the use of stratospheric data from the NCEP dataset before the IGY for climate change studies.

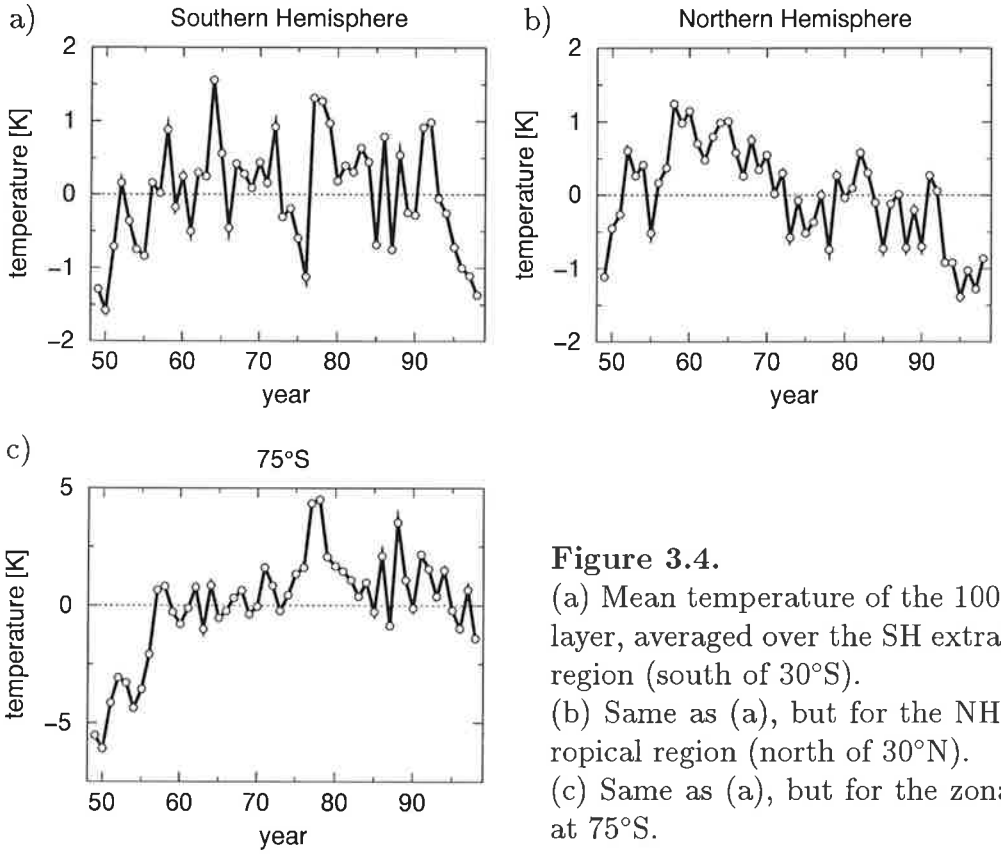

Figure 3.4.
(a) Mean temperature of the 100-50-hPa layer, averaged over the SH extratropical region (south of 30°S).
(b) Same as (a), but for the NH extratropical region (north of 30°N).
(c) Same as (a), but for the zonal mean at 75°S.

3.4 50-hPa Geopotential Heights

The spurious temperature change in the NCEP dataset described in Section 3.1 also affects the NH geopotential height data in the lower stratosphere. We investigated to what extent the zonal mean 50-hPa geopotential heights are influenced. The panels in Figure 3.5 show this parameter from the NCEP and

FUB datasets at different latitudes both for winter ($\overline{\text{DJF}}$[2], left panels) and summer means ($\overline{\text{JJA}}$[3], right panels). For winter means, the correlation between the time series of the two datasets increases with increasing latitudes. At low latitudes, the zonal mean geopotential heights from the NCEP reanalyses are lower (higher) before (after) 1977 than these from the FUB dataset. At high latitudes, the interannual variability in both datasets, which strongly dominates long-term temporal behavior, agrees very well. During the entire period, the values of the zonal mean 50-hPa heights at 80°N in the FUB dataset are somewhat smaller than the NCEP values. In contrast for the summer-mean data, this parameter is, in general, higher in the FUB than in the NCEP analyses.

The differences described between the temporal behavior of the zonal mean geopotential heights in the two datasets are related to differences in the results of linear trend analyses. This is illustrated in Figures 3.6 which shows monthly mean linear trends of the 40-year period 1958-1998. Shading indicates where the trends are significant to at least at the 95% level. It is obvious that the region of statistically significant trends is larger in the NCEP analyses (Figures 3.6b) than in the FUB analyses (Figures 3.6a). At lower latitudes, the NCEP data show an increase for all months of the year. In the FUB dataset, this increase is limited to the cold-season months. This difference between both datasets corresponds to the spurious temperature changes in the lower tropical stratosphere discussed in Section 3.1.

During winter and summer, both datasets show a significant decrease in the heights at higher latitudes (north of 60°N). Figure 3.6 reveals that the decrease is larger in the NCEP reanalyses than in the FUB analyses. It also apparent that the significant decrease at mid-latitudes from April to September only appears in the NCEP dataset.

We conclude that the 50-hPa geopotential heights in the NCEP reanalyses do not correctly reflect observed changes in NH stratospheric circulation. For the cold season, height data north of 40 °N and, for summer, data north of 60 °N are recommended for trend studies of the recent four decades.

3.5 Leading Coupled Modes of Variability

A principal goal of this thesis is to study the coupled modes of variability of tropospheric and stratospheric circulation in the NH and their interdecadal change. We will now evaluate to what extent these hemispheric scale modes of variability are affected by the inhomogeneities in the NCEP reanalyses. To do this, two

[2] $\overline{\text{DJF}}$: average over the months December, January, February
[3] $\overline{\text{JJA}}$: average over the months June, July,August

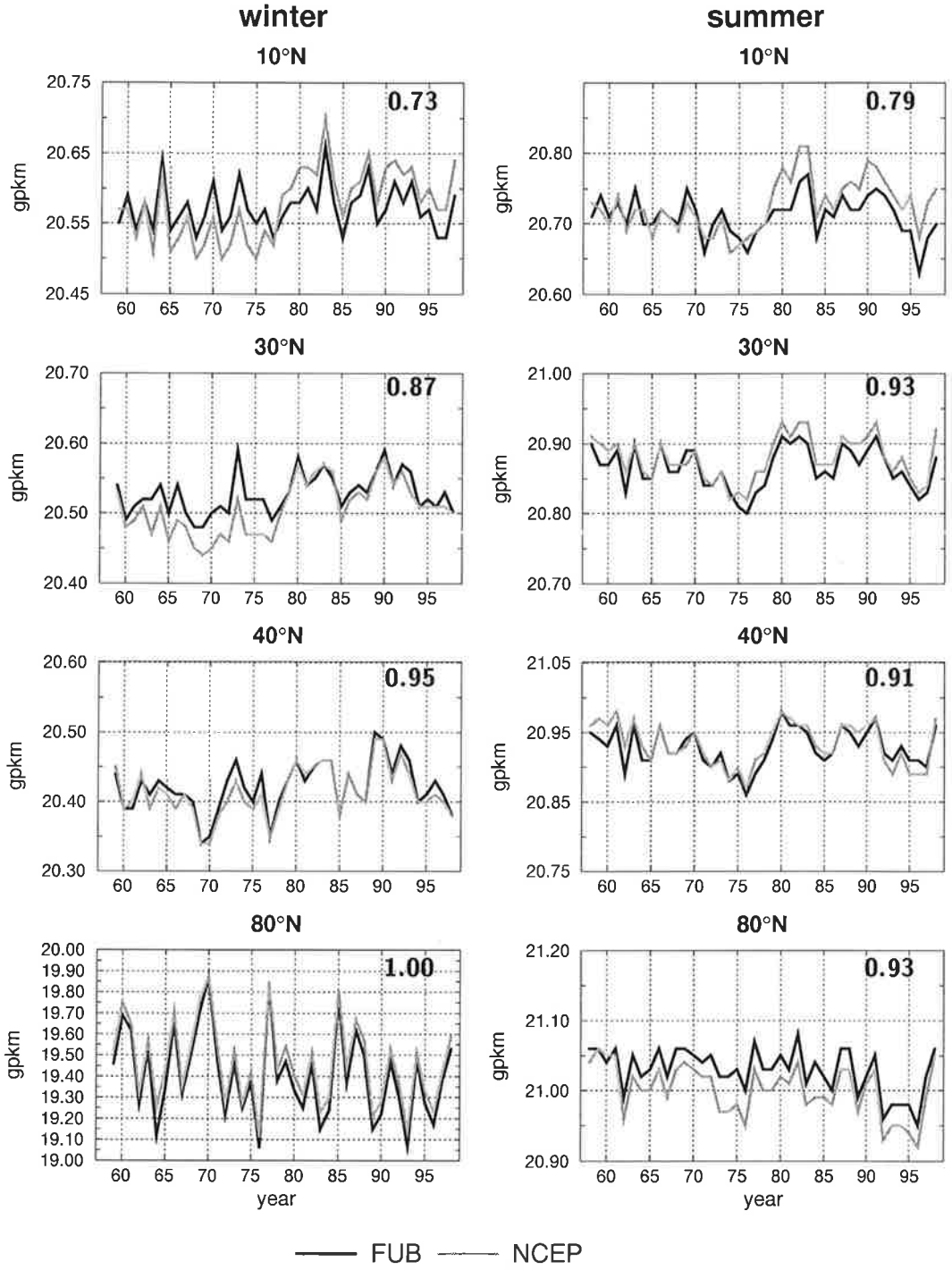

Figure 3.5. Winter mean ($\overline{\text{DJF}}$, left panels) and summer mean ($\overline{\text{JJA}}$, right panels) zonally averaged 50-hPa geopotential heights, determined for FUB (black line) and NCEP reanalyses (grey line) at different latitudes. The number in the upper right corner of the graphs indicates the temporal correlation coefficient between both time series.

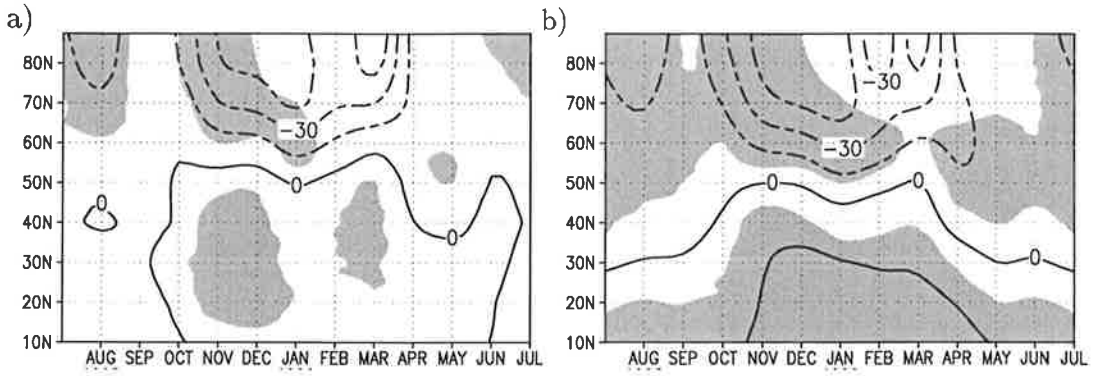

Figure 3.6. Monthly long-term linear trends (1958–1998) of zonally averaged 50-hPa geopotential heights, determined for (a) the FUB dataset and (b) the NCEP dataset. The shading indicates where the local trends are significant at least at the 95% level.

different datasets, the NCEP reanalyses and the combined FUB/NMC dataset were compared. SVD analysis was applied to isolate the coupled modes in the 50- and 500-hPa geopotential height fields. In particular, the correlation coefficients between the temporal expansion coefficients of the first mode of both datasets were calculated to compare their temporal behavior. The same is done for the second coupled mode. We studied the cold-season months November to April, and both winter ($\overline{\text{DJF}}$) and summer ($\overline{\text{JJA}}$) means. The physical interpretation of the coupled modes can be found in Chapter 7.

To study the cold-season months November to April, the data was preprocessed by removing the mean seasonal cycle and weighting the grid point data with the square root of the cosine of the latitude. In order to isolate a possibly strong effect of the spurious change at low latitudes, we analyzed the regions from 20°, 30° and 40°N northwards, individually. Table 3.1 indicates that the correlation coefficients for the expansion coefficients of both the 50- and the 500-hPa geopotential heights are very heigh. The largest agreement is found for the region north of 30°N. The correlation coefficients for both levels of the first two coupled modes amounts to 0.99.

We also calculated correlation coefficients for each month separately. From the temporal expansion coefficients, we created sets for each months (November to April) and calculated the correlation coefficients for the individual sets. This analysis allows as to examine whether the high similarity of the time series as shown in Table 3.1 results from the seasonal cycle of variability. Figure 3.7 confirms the high agreement between the temporal expansion coefficients of the first coupled variability mode for both the north-of-20°N and the north-of-30°N analyses. The correlation coefficients are 0.99 for the most months and never smaller than 0.98. For the second coupled mode, the highest agreement between the two datasets can be found for the region north of 30°N.

Table 3.1. Correlation coefficients between the expansion coefficients of the coupled modes in the FUB analyses and the NCEP reanalyses. SVD analyses was applied to isolate the coupled modes in the 50- and 500-hPa geopotential height fields of the cold-season months for the NH regions northwards of 20°N, 30°N, and 40°N).

	1st Mode			2nd Mode		
	20°N[(a)]	30°N	40°N	20°N	30°N	40°N
50 hPa	0.99	0.99	0.99	0.98	0.99	0.95
500 hPa	0.99	0.99	0.94	0.99	0.99	0.96

[(a)] 20°N, 30°N and 40°N stands for north-of-20°N, north-of-30°N and north-of-40°N analyses, respectively.

In the case of winter mean geopotential heights only the first coupled mode is important (Baldwin et al., 1994). The correlation coefficients between the temporal expansion coefficients of both datasets are larger than 0.99 for both the 50- and 500-hPa level and each of the three regions. The relationships are smaller during summer than during winter. For instance, the correlation coefficients for the first coupled mode of the north-of-30°N analyses are 0.92 (50-hPa level) and 0.89 (500-hPa level).

These analyses show that SVD-filtered time series of the cold-season NH 50- and 500-hPa geopotential heights in the NCEP reanalyses are insensitive to inhomogeneities due to modifications in the databases incorporated into the reanalyses. During winter, these time series reflect the dynamical coupling of stratosphere and troposphere. Due to this coupling which is a hemispheric-scale feature, the variability in the stratosphere is strongly related to the tropospheric circulation. Hence, changes in the database have a relatively small influence on the stratosphere in the reanalyses, providing the GCM used for the reanalyses is able to reproduce the dynamical coupling between the troposphere and stratosphere in the right way. During summer, radiative processes in the stratosphere itself dominate the variability of the climate variables in this layer, since the dynamical coupling of troposphere and stratosphere is not an important process in this season. Therefore, inhomogeneities in the stratospheric database more affect the SVD-filtered time series in summer than in winter.

SVD-filtered time series increase the reliability of trend analyses not only in the stratosphere but also in the mid-troposphere time series because the tropospheric data at lower latitudes may also be affected by the changes in the observations used for the reanalyses.

The previous analyses reveal that datasets of tropospheric and stratospheric

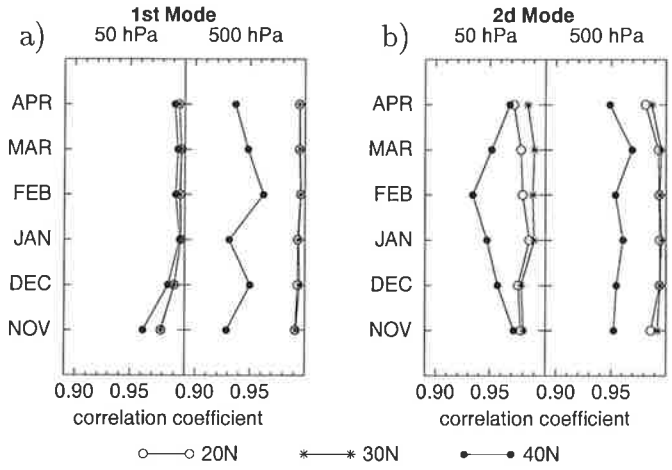

Figure 3.7. Correlation coefficients between the expansion coefficients of the NCEP dataset and the FUB/NMC dataset. a) 1st SVD mode, and b) 2nd SVD mode determined between the 50- and 500-hPa geopotential height fields for the NH regions north of 20°N, 30°N and 40°N.

geopotential heights in the cold-season months filtered by SVD analysis can be used for studying interdecadal climate change.

3.6 Summary

We cannot expected to have a dataset which perfectly reflects the real temporal behavior of global-scale tropospheric and stratospheric circulation for the last four decades. The most comprehensive information is available for the NH where a large number of long-term rawinsonde records over the continental areas exists. Reanalysis projects are designed to study climate variability and climate change. The NCEP reanalyses, however, exhibit inhomogeneities because of the changing datasets incorporated during the 50 year period. This makes the use of this data for studying climate change more difficult.

We investigated whether SH stratospheric data before the incorporation of satellite data, and NH data before the IGY can be considered for trend calculations. We also studied the reliability of trend analysis results of the zonal mean geopotential heights at the 50-hPa level in more detail. We concluded that the NCEP reanalyses of stratospheric geopotential heights and temperature data in the SH and in the NH lower latitudes should not be used for long-term climate change studies. In contrast, mid- and high latitude data in the boreal winter and high latitude data in the boreal summer are reliable for the statistical analysis of cli-

mate trends. Such analysis should only include stratospheric data from the period after the IGY.

We studied the coupled modes of NH tropospheric and stratospheric circulation. SVD analysis was applied to isolate the coupled modes in NH 50- and 500-hPa geopotential height fields. The temporal expansion coefficients of the first two modes of the NCEP and an independent dataset (FUB/NMC), studied for cold-season months, have shown strong agreement. During winter, the SVD-filtered time series of the NH 50- and 500-hPa geopotential heights in the NCEP reanalyses are less sensitive to inhomogeneities than during summer. We have recommended the SVD-filtered time series of 50- and 500-hPa geopotential heights for studying climate change in the cold-season months.

Chapter 4

The Variability of the Horizontal Circulation in the Troposphere and Stratosphere

4.1 Introduction

Wave motions in the stratosphere are primarily produced and maintained by the vertical propagation of planetary wave disturbances generated in the troposphere (for a review, see Hartmann, 1985). The atmospheric flow in the troposphere shows a broad spectrum of Rossby modes, including synoptic scale waves, whereas the atmospheric flow in the stratosphere is dominated by ultra-long planetary waves. The reason for this difference is that the stratospheric zonal wind distribution has a strong filtering effect on tropospheric disturbances as indicated by the Charney-Drazin Theorem (Section 2.2.2, Equation 2.34). As a consequence, the space-time variability of the horizontal circulation differs strongly between the troposphere and stratosphere.

We applied various approaches in order to illustrate the differences between the variability of the horizontal circulation in the NH troposphere and stratosphere: Spatial degrees of freedom (dof) on different time scales were derived, EOF analysis was performed to geopotential height fields for cold-season months November to April, and features of the spatial and temporal variability of the winterly zonal mean zonal wind were studied by applying recurrence and persistence analyses. NCEP reanalyses of the 50- and 500-hPa geopotential heights of the period from 1958 to 1999 were used.

The number of dof is a parameter for describing the dimensionality of a dynamical system, such as the atmosphere, or for defining the number of independent

variables in a dataset. Numerous studies exist using different approaches for giving estimates of the *dof* of the NH tropospheric circulation (e.g., Fraedrich et al., 1995; Toth, 1995; Wang and Shen, 1999). *Dof* of the horizontal circulation in the lower stratosphere have not been investigated so far. Here, we will compare the spatial *dof* of the NH 50- and 500-hPa geopotential heights on different time scales both for the summer and winter season (Section 4.2).

The spatial structure of the leading EOFs in the NH 50-hPa geopotential height fields is similar to spherical harmonics (Wallace et al., 1995; Perlwitz and Graf, 1995). The leading EOFs of the 500-hPa geopotential heights exhibit more complex hemispheric-scale structures (e.g., Wallace and Gutzler, 1981). Thompson and Wallace (1998) defined the the first EOF of cold season monthly-mean 1000-hPa geopotential anomalies as Arctic Oscillation. The authors emphasized that the regression patterns based on the AO-index exhibit a distinct signature in the geopotential height fields marked by a zonally symmetric, equivalent barotropic structure that amplifies by a factor of 5 from the surface to the lower stratosphere. Here, we have applied EOF analysis to the geopotential heights at the 50- and 500-hPa levels in order to illustrate differences between the spatial variability of the atmospheric circulation in both atmospheric layers in more detail (Section 4.3).

Regime-like behaviour of atmospheric flow is manifested by the recurrence or persistence of flow patterns (Wallace et al., 1991; Dole and Gordon, 1983). Here, both features of the zonal mean zonal wind $\bar{u}$ were studied to emphasize differences between the time-space anomaly structures of $\bar{u}$ at the 50- and 500-hPa level in the winter season (Section 4.4).

4.2 Spatial Degrees of Freedom of the Atmospheric Flow

We used the simplified method of Fraedrich et al. (1995) to illustrate the difference in complexity of horizontal circulation between troposphere and stratosphere. With this method, the squared distance from the climatological mean is analyzed. The estimate is based on a linear approach, because spatial patterns are described in terms of EOFs. The spatial *dof* are estimated by comparing the variance of the theoretical standardized chi-squared distribution with the sum of the squared eigenvalues of a spatial correlation matrix:

$$dof = N^2 / \sum_{k=1}^{N} \lambda_k^2 \tag{4.1}$$

Table 4.1. Estimates of spatial degrees of freedom (*dof*) of NH (north of 30°N) mid-tropospheric and lower stratospheric flow using the method of Fraedrich et al. (1995)

	daily		daily (low-pass)		monthly	
	DJF	**JJA**	**DJF**	**JJA**	**DJF**	**JJA**
Z-50 hPa	9	4	8	3	5	2
Z-500 hPa	29	46	21	36	13	19

where N is the number of grid-points and λ_k is eigenvalue of the correlation matrix.

Our estimates of the spatial *dof* of the NH stratospheric and tropospheric flow are based on grid-point data of the 50- and 500-hPa geopotential heights north of 30°N. We analyzed daily data, lowpass (>10-days) filtered daily data[1] and monthly means. Before applying EOF analysis, the data was transformed from the regular grid to an equal-area grid in order to avoid an overestimate of the variability at high latitudes.

Table 4.1 shows the *dof* calculated for both the summer (JJA) and winter (DJF) seasons. The tropospheric *dof* correspond to published results. For example, Wallace et al. (1991) determined 20 *dof* for the NH lowpass filtered daily 500-hPa geopotential heights. In agreement with previous studies, we also found a considerable increase in the *dof* from 29 in winter to 46 in summer. This interseasonal change in the number of *dof* indicates that regime-like behavior is less present during northern summer (Wallace and Zhang, 1993). During this season, local processes like convection play a more important role than in winter when the tropospheric flow is dominated by large scale dynamics.

Comparing troposphere with stratosphere, we found that the stratospheric flow is characterized by a considerably smaller number of spatial *dof*. The reason is that only ultra-long planetary scale motions can be observed in the stratosphere. The further reduction of the *dof* is relatively smaller in the stratosphere, when low-pass filtered variability or monthly averaged fields are studied, because synoptic-scale Rossby waves are strongly trapped in the troposphere. In addition, the troposphere and stratosphere exhibit different interseasonal behavior. In the stratosphere, the number of *dof* of daily variability *decreases* from 9 in winter to 4 in summer. The reason for this decrease is that the dynamical coupling between troposphere and stratosphere is very weak during summer.

[1]The lowpass filtered daily data were determined on the basis of the 21-point filter by Blackmon and Lau (1980).

4.3 Leading EOFs of Cold Season Winter Months

We derived the leading EOFs of the 50- and 500-hPa geopotential heights of the cold season to illustrate differences between the variability structures of tropospheric and stratospheric circulation. The monthly means from November to April were analyzed. During this time of the year, on average, the zonal mean zonal wind at the 50-hPa level is westerly, and one standard deviation (σ) of monthly interannual variability in mid-latitude exceeds $2.5\,\mathrm{m\,s^{-1}}$ (Figure 4.1). Before applying EOF analysis, the seasonal cycle and the long-term trends for each month were removed from the time series.

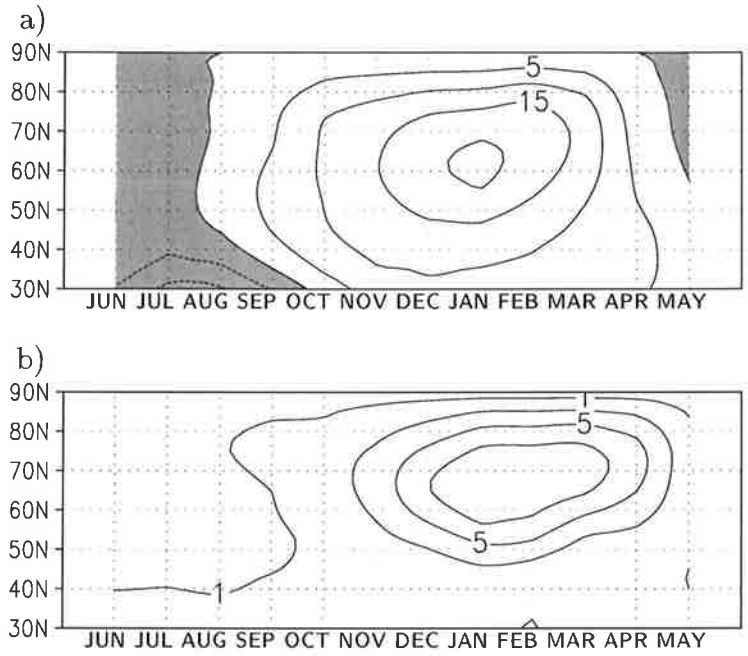

Figure 4.1. a) Long-term monthly mean and (b) monthly standard deviation of the zonal mean zonal wind at 50-hPa in [m/s]. Negative values in (a) are shaded.

The spectra of the first 10 eigenvalues of the 50- and 500-hPa heights are shown in Figure 4.2. The errorbars of the eigenvalues were calculated according to North et al. (1982) (see Section 2.1.1, Equation 2.10). These errorbars indicate that the first three EOFs are well separated in the stratospheric field. In the tropospheric field, the eigenvalues of the second and third modes are very close. Thus, it is quite probable that a linear combination of these two EOFs is also an EOF of this field.

The first three EOFs of the 50- and 500-hPa fields are displayed in Figures 4.3 and 4.4. The fraction of total variance explained by the individual EOFs is given at the right upper corner of each EOF map. A principal reason for the difference

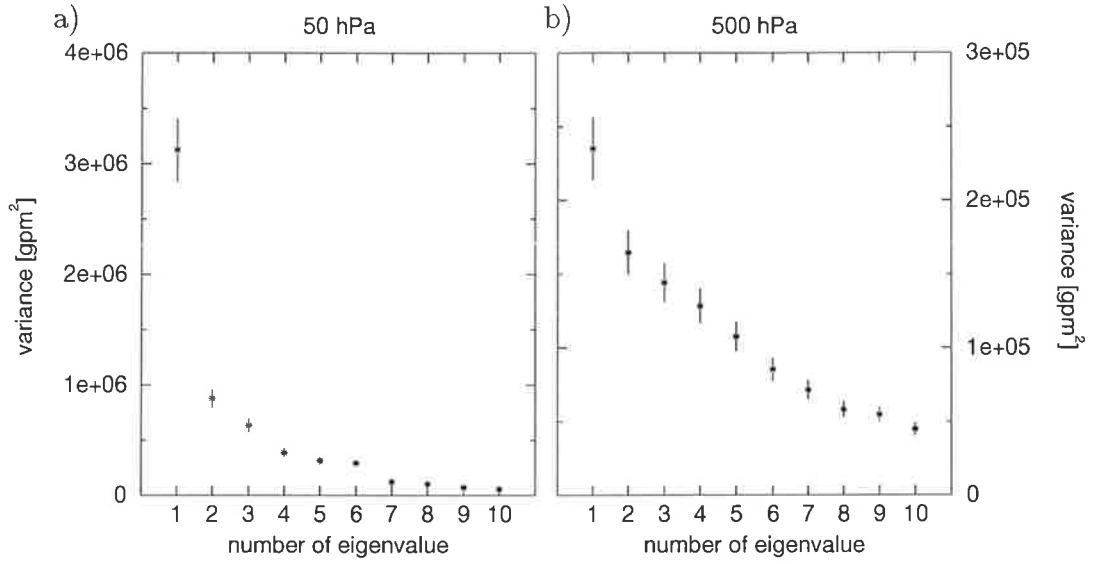

Figure 4.2. Eigenvalues and errorbars for the first 10 EOFs of the a) 50-hPa and b) 500-hPa geopotential height fields. The errorbars of the eigenvalues were calculated according to North et al. (1982).

in dimensionality of the horizontal flow in the troposphere and stratosphere, as discussed in the previous section, becomes clear. At the stratospheric level, the leading EOF of the geopotential height field already describes a large fraction (about 50%) of the total variance. The first three EOFs taken together account for more than 74% of the total variance. The eigenvalue spectra of the 500-hPa geopotential height field exhibit a slowly and more continuous drop (Figure 4.2b). To explain 75% of the total variance, the first 10 EOFs have to be considered.

The EOFs of the 50-hPa field clearly assume the form of spherical harmonics because of the strongly reduced influence of longitudinal asymmetries in the lower boundary conditions (North, 1975; Wallace et al., 1995). The leading EOF of the stratospheric geopotential height field shows a circumpolar pressure seesaw between high and subpolar latitudes (Figures 4.3a). Thus, this EOF describes the variation in the strength of the polar winter vortex. Both the second and third mode of the 50-hPa height field have the structure of a spherical wave of ZWN 1 (Figures 4.3b and 4.3c). The phase of the third EOF is shifted with respect to the phase of the second one by 90° of zonal direction. The next two higher modes (not shown) exhibit the structure of spherical waves of ZWN 2. These two higher modes contribute significantly to the total variability, not on the basis of monthly means, but on the daily time scale.

In contrast, the EOFs of the 500-hPa geopotential height field exhibit more complex, global scale structures by forming of wave trains. The first EOF shows a

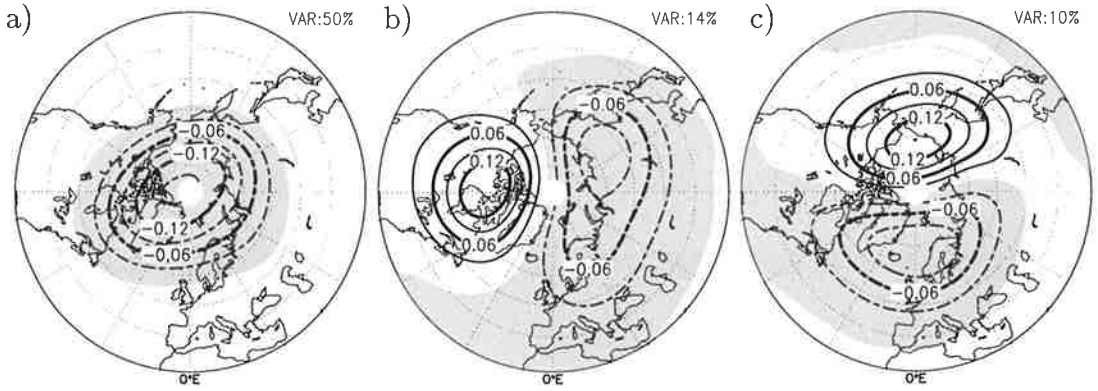

Figure 4.3. a) First, b) second and c) third EOF of the 50-hPa NH (north of 30°N) geopotential height field, determined on the basis of monthly means November to April for the time period 1958/59– 1998/99. Negative values are shaded. The fraction of explained total variance is given in the right upper corner of the individual maps.

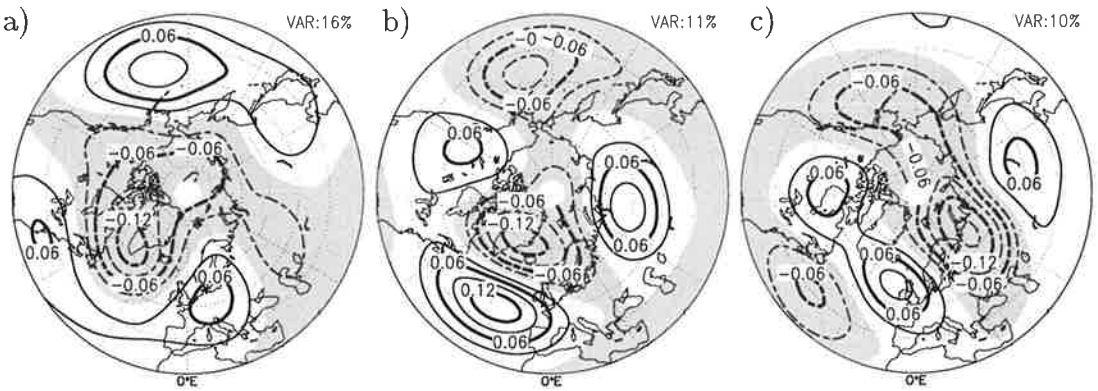

Figure 4.4. Same as Figure 4.3, but for the 500-hPa geopotential height field.

main center over southern Greenland. The mid-latitude centers of action with opposite sign appear over the North Pacific, the western Atlantic and Central Europe (Figure 4.4a). The second and third EOF (Figures 4.4b and 4.4c) show a similar wave train-like structure in which the centers of action of the third EOF appear near the nodelines between the centers of action of the second EOF. The second EOF is similar to the circulation pattern that corresponds to the *cold ocean warm land* (COWL) temperature pattern which explains a large fraction of the temperature change observed during the recent decades (Wallace et al., 1996). We have shown that the eigenvalue of this EOF is not clearly separated from the eigenvalue of the third EOF when 246 monthly realizations are used. However, this pattern is very robust, when reanalysis data for a longer period (1949–1999) are studied (not shown).

Thompson and Wallace (2000) characterized the AO as an "annular mode" because of its deep, zonally symmetric structures, with geopotential height perturbations of opposing signs in the polar cap region and in the surrounding zonal ring centered near 45°N. To study the importance of the variation of the zonal structure of the first EOFs of the 50- and 500-hPa level in more detail, we determined the correlation coefficients between the temporal expansion coefficients of these EOFs and the zonal mean zonal wind at the respective pressure level. The same was done for the zonal mean meridional component. The results for both the tropospheric and stratospheric field are shown in Figure 4.5. The pattern of the first stratospheric EOF clearly exhibits an annular mode because this mode is closely related to variations in the zonal mean zonal wind at mid-latitudes whereas variations in the meridional component are not relevant. In contrast, the expansion coefficients of the leading EOF of the tropospheric field are strongly related to the zonal average of both wind components in mid-latitudes. Therefore, the first EOF of the 500-hPa geopotential height field cannot be regarded as an annular mode.

There are not only pronounced differences between the spatial structure of the first EOFs of the 50- and 500-hPa geopotential heights, but also remarkable differences between the temporal behaviors of the expansion coefficients of the respective EOFs. The one-month autocorrelation of the first stratospheric mode (0.5) is higher than the respective autocorrelation of the first tropospheric mode (0.3). The significant one-month autocorrelation of the stratospheric index indicates a high persistence of anomalously strong or weak polar vortexes.

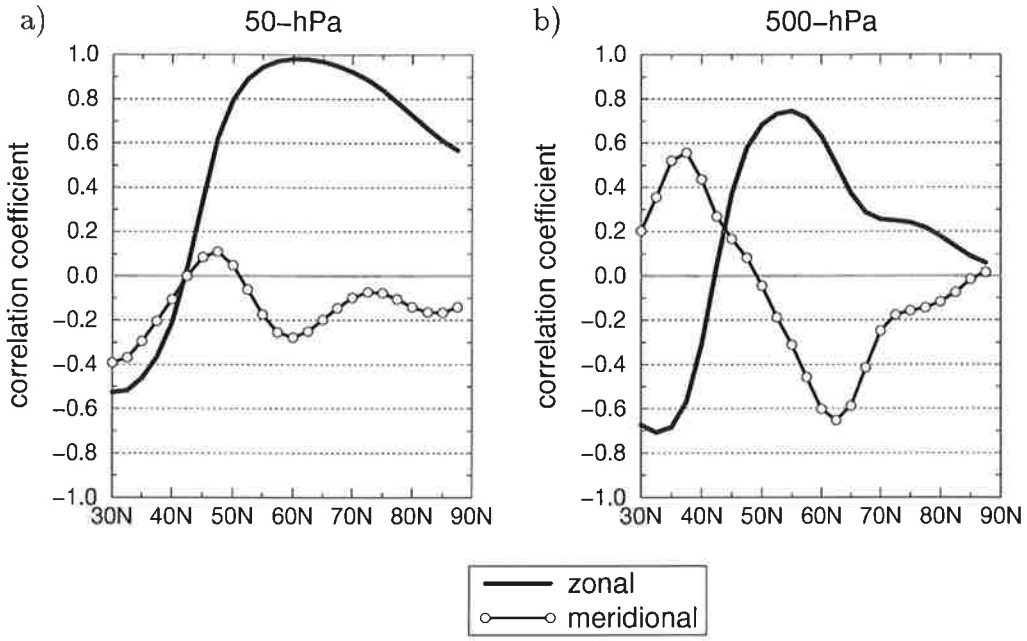

Figure 4.5. a) Correlation between the expansion coefficients of the first EOF of the 50-hPa geopotential height and both the zonal mean zonal wind and the zonal mean meridional wind at the same pressure level. b) Same as in (a) but for the 500-hPa geopotential heights.

4.4 Variability Characteristics of the Zonal Mean Zonal Wind

We have described that on the monthly time scale, the index of the strength of the stratospheric polar vortex explains about 50% of the total variability in the NH 50-hPa geopotential height field. Next, we will discuss in greater detail whether this feature indicates that the zonal mean winter circulation in the lower stratosphere is characterized by two preferred states: an anomalously weak or an anomalously strong polar vortex. We have applied the same methods used to study the regime-like behavior of low-frequency atmospheric flow (Wallace et al., 1991; Dole and Gordon, 1983). Regime-like behavior of atmospheric flow is manifested by recurrence or persistence of flow patterns. We studied these features in the NH zonal mean wind field ($\bar{u}$) at the 50- as well as at the 500-hPa pressure level to demonstrate the differences between the tropospheric and stratospheric circulation.

4.4.1 Recurrence of Anomaly Patterns of the Zonal Mean Zonal Wind

Studying the recurrence of anomaly patterns of $\bar{u}$ at specific pressure levels, these patterns actually exhibit one-dimensional arrays. We determined the frequency distribution of spatial correlation between these anomaly patterns (referred to as *anomaly correlation*) based on a large number of pairs of the lowpass filtered arrays of $\bar{u}$. The analyses were performed for the 50- and 500-hPa field using mid-winter months (DJF) for the period from December 1958 to February 1999. We removed the climatological annual cycle before applying the temporal filtering. From the filtered time series, arrays at 5-day intervals, i.e., a total of 738 arrays (18 graphs $\times$ 41 years) were selected. Following the approach used by Gutzler and Shukla (1984) and Wallace et al. (1991), we calculated the anomaly correlation r_{ij} between two graphs $\bar{u}_i$ and $\bar{u}_j$

$$r_{ij} = \frac{[(\bar{u}_i - \bar{u}_i^g)(\bar{u}_j - \bar{u}_j^g)]}{\sqrt{[(\bar{u}_i - \bar{u}_i^g)^2]}\sqrt{(\bar{u}_j - \bar{u}_j^g)^2}},$$

where $\bar{u}^g$ is the spatial mean, the indices i and j identify particular arrays, and the brackets operator [ ] represents an average over all grid points. Pairs of graphs with large positive anomaly correlation may reflect circulation regimes that recur relatively frequently within the time period studied. Only half of the 738 $\times$ 737 matrix needed to be computed since $r_{ij} = r_{ji}$. The frequency distribution of the anomaly correlations was determined on the basis of the correlation coefficients between all graphs excluding those from the same winter.

Figure 4.6 shows the frequency distributions of these anomaly correlations at the 50- and 500-hPa levels. The frequency distribution of $\bar{u}$(50-hPa) exhibits a strong bimodality. The most frequent correlation coefficients occur in the classes from 0.8 to 0.9, and from -0.9 to -0.8. Thus, the variability of $\bar{u}$(50-hPa) has one preferred latitudinal structure appearing in its two polarities. In contrast, the corresponding frequency distribution of the 500-hPa field has one broad maximum region centered between -0.6 and 0.6 where values larger than 15000 occur. This distribution seems slightly skewed because the number of frequencies is higher in the classes from -0.9 to -0.4 than in the corresponding classes of positive polarity.

The frequency distributions of $\bar{u}$ can be understood within the context of the non-linear paradigm for the description of low-frequency variability (Wallace et al., 1991, for a review). This non-linear paradigm views the climatological mean as an arbitrary mathematical construct, which does not need to bear any relation to the most frequently observed state(s) of the atmosphere. It predicts that indices of spatial patterns may exhibit highly skewed or even bi- (or multi-) modal

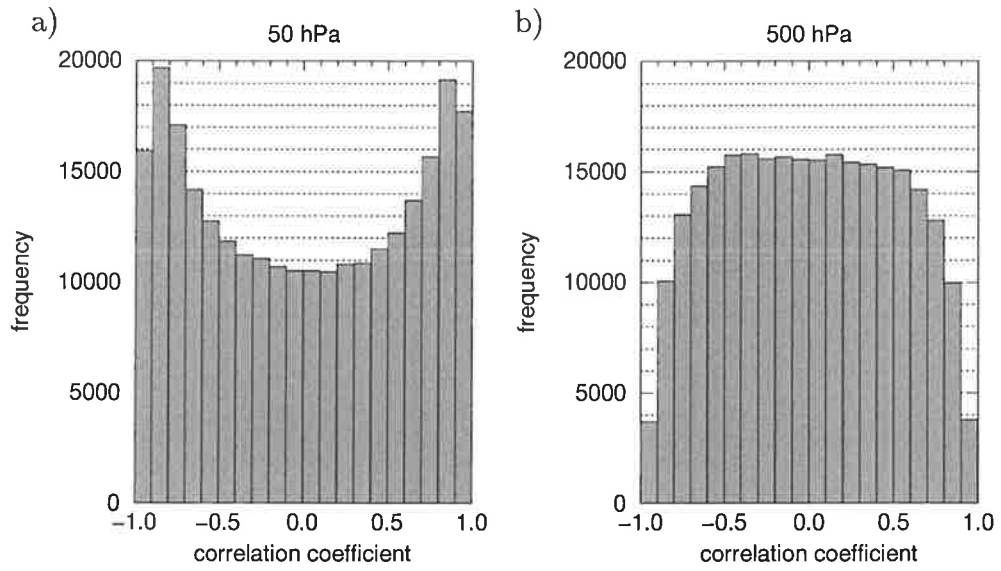

Figure 4.6. Frequency distribution of the anomaly correlation r_{ij} between all possible pairs of lowpass filtered anomaly graphs of $\bar{u}$, excluding those from the same winter. a) $\bar{u}_{50}$, and b) $\bar{u}_{500}$.

frequency distributions. The bimodal distribution of the anomaly correlations of the zonal mean wind in the stratosphere exhibits such non-linear behavior. The two patterns, which belong to the maxima, exhibit an anomalously strong and weak polar winter vortex with maximum anomalies between 55° and 75°N. The variations of $\bar{u}$, which very strongly smoothed the longitudinal structures of circulation, are in-sufficient for the understanding of tropospheric climate regimes.

To put stress on the anomaly strength, we also calculated the frequency distribution of the *spatial covariance* between pairs of arrays. We found that strong bimodality in $\bar{u}$(50-hPa) is only a feature of the anomaly correlation, i.e., it does not result from the strength of the anomaly, but rather clearly reflects structural effects.

4.4.2 Persistence of the Leading EOF of the Zonal Mean Zonal Wind

The previous analysis has not given any information about the persistence of a specific structure that very often appears in its two polarities (anomalously strong and anomalously weak polar night vortex). The high one-month autocorrelation of the leading EOF of NH 50-hPa geopotential height has already indicated a persistent anomalously strong or weak polar vortex. We studied this behavior in more detail on the basis of 10-day lowpass filtered time series of $\bar{u}$. We determined

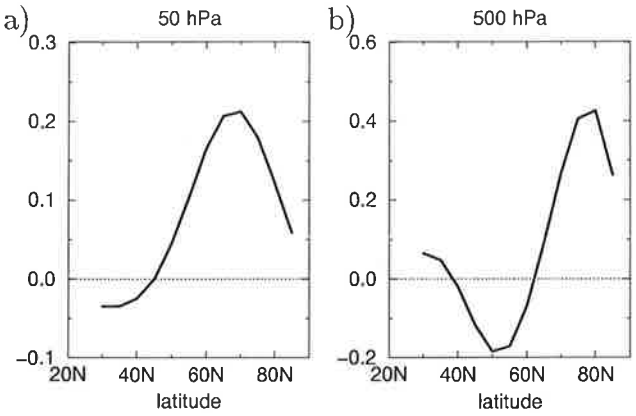

Figure 4.7. First EOF of zonal mean zonal wind during winter, determined on the basis of lowpass filtered daily data. a) 50-hPa level, b) 500-hPa level.

the leading EOF of $\bar{u}$ at the 50-hPa pressure level and, for comparison, also at the 500-hPa level for the winter months (December to February). Again, the climatological annual cycle was removed before applying EOF analysis and the EOFs were derived on the basis of the covariance matrix.

The first EOF of $\bar{u}$ at both the 50- and 500-hPa level are shown in Figure 4.7. The corresponding explained fractions of total variance are 71% and 41%, respectively. As expected, the stratospheric EOF describes the variation of the strength of the stratospheric polar winter vortex, with a maximum variation near 65°N. The leading EOF of the 500-hPa level, which has an extremum near 75°N and an extremum of opposite sign near 50°N, describes the shift of the mid-tropospheric zonal mean wind maximum.

We determined the positive and negative persistence of these two patterns by using the standardized temporal expansion coefficients, i.e. the mean value and the standard deviation (σ) are equal to zero and one, respectively. Anomalies larger than the absolute value of 0.5σ are defined as *relevant anomalies*. We studied the duration (e.g., longer than 10 days) of relevant positive and negative anomalies. These events, determined for each 90-day period of the 41 years considered, were counted for specific durations. The total number was normalized to a 10-year period. We found that the distributions of the events for positive and negative anomalies were very similar. The sum total of events is shown in Figure 4.8. It can be seen that the tropospheric index drops faster with increasing duration than the stratospheric index. A persistence of 40 days or more of relevant anomalies ($>0.5\sigma$ or $< -0.5\sigma$), which have the pattern of the leading EOF, is not observable in the troposphere, but is seen about 3 times within 10 years in the lower stratosphere.

The remarkable persistence of an anomalously strong or weak stratospheric po-

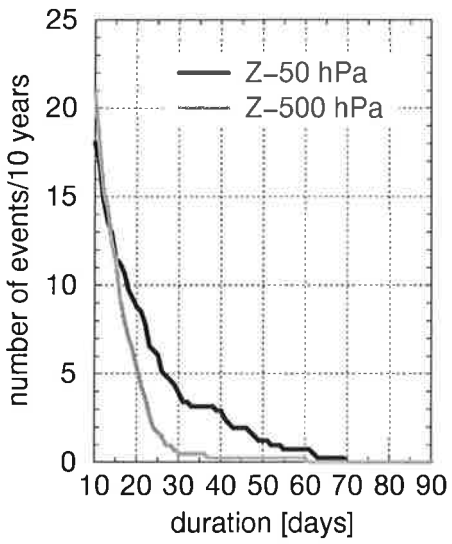

Figure 4.8. Number of the total sum of events for persistent positive and negative anomalies ($>0.5\sigma$ or $< -0.5\sigma$), which have the structure of the leading EOF of $\bar{u}$ as function of a minimum duration, exceeded. The distributions are normalized to 10 years. The distributions for the first mode of $\bar{u}$ (north of 30°N) at the 50- and 500-hPa level are shown.

lar vortex results from a positive feedback mechanism that exists between wave forcing of the zonal mean flow and the refraction of waves by the mean flow. The propagation of wave energy into the polar stratosphere, which occurs in conjunction with weaker lower stratospheric winds, results in stronger wave forcing of the mean winds in the stratosphere. The wave drag tends to maintain the weak winds and, therefore, a warm polar stratosphere, that allows a continuous strong propagation of waves into the stratosphere. On the other hand, strong lower stratospheric winds shield the polar stratosphere from wave activity and allow it to more nearly approach the radiative equilibrium state. Thus, due to the positive feedback mechanism of wave–mean flow interaction, an anomalously weak or strong polar stratospheric vortex, caused by external forcing or internal variability, is maintained for a longer period. However, Figure 4.8a also indicates that the effect of such positive feedback mechanisms is limited. For instance, sudden warmings resulting from anomalous tropospheric conditions destroy the cold, anomalously strong polar vortex. The persistence of an anomalously weak vortex requires a continuous influx of wave activity from the troposphere which is not given in all instances.

4.5 Summary and Conclusions

To illustrate differences in the variability of the horizontal circulation in the mid-troposphere and stratosphere, various approaches were applied like estimating the spatial *dof*, EOF analysis, persistence and recurrence analyses.

We have elucidated that a striking feature of the stratospheric circulation is its apparent structural simplicity, when compared to the troposphere. An indication for the simplicity of stratospheric circulation is the remarkably smaller number of spatial *dof*. For 10-day lowpass filtered time series of the NH 50- and 500-hPa geopotential heights during the winter season (December to February), we have obtained 21 *dof* and 8 *dof*, respectively. This difference is even clearer during summer, when stratospheric and mid-tropospheric circulation are characterized by 3 *dof* and 36 *dof*, respectively. Thus, a different interseasonal behavior regarding the spatial dimensionality of both atmospheric layers becomes obvious.

By applying EOF analyses of the 50- and 500-hPa geopotential height fields, it was illustrated that the number of circulation modes during the cold season (November to April), which can be well isolated without being obscured by noise, is three in the lower stratosphere, but only one in the mid-troposphere. The spatial variability of the stratospheric winter circulation can be mainly described by spherical harmonics, whereas hemispheric-scale EOFs of the mid-tropospheric fields show complex hemispheric-scale structures by forming of wave trains. However, it is important to keep in mind that these EOFs alone provide only limited information about important variability structures which could be explained physically.

Our analyses indicated that an essential fraction of variability in the stratosphere during the cold season is characterized by the variation in the strength of the stratospheric polar vortex. This is the most important mode of the intra- and interannual variability of the stratospheric winter circulation. Variations in the strength of the stratospheric polar winter vortex show a high temporal persistence. We also illustrated that the recurrence patterns of $\bar{u}$ exhibit a bimodal distribution, describing an anomalously strong and an anomalously weak polar winter vortex.

The modification of the tropospheric circulation during the cold season due to increased anthropogenic forcing is closely related to the climate change response of the near surface temperature. Taking into account that climate changes appear as a change in the occurrence of modes of natural climate variability (Palmer, 1993, 1999), our main conclusion is as follows: The detection of cold season climate change should be based on variability modes of the coupled troposphere-stratospheric circulation because of the strong spatial filtering of the tropospheric circulation by the stratospheric mean flow. As a consequence of the larger signal

to noise ratio for the stratospheric circulation, the spatially filtered climate change pattern may be detectable earlier in the stratosphere than in the troposphere. This climate change pattern, however, may have a different spatial structure in the troposphere than in the stratosphere.

Chapter 5

Relationship Between Tropospheric and Stratospheric Wave-Like Disturbances

5.1 Introduction

A principal concept for the description of the mutual dynamical coupling between troposphere and stratosphere is based on the wave-mean flow interaction (Matsuno, 1970). Ultra-long planetary waves, generated by orography and diabatic heating, propagate into the stratosphere and modify the mean flow by transfer of heat and momentum. The strength of the stratospheric polar winter vortex determines the transmission-refraction properties of these vertically propagating waves, and, thus, modifies the structure of ultra-long tropospheric waves. Finding evidence in observational data for this mutual coupling is relevant to verifying this theoretical concept. The characteristic features of the coupling are also very important in validating the capability of atmospheric GCMs to reproduce this dynamical process.

On the basis of observational data, Randel (1988) studied the coherent behavior of tropospheric and stratospheric waves by applying the cross-spectral correlation analysis of Randel (1987) on individual zonal waves 1, 2 and 3 in geopotential height fields. The author used low-pass filtered (>10 days) geopotential grid data from 1000 up to 1-hPa of the winter months December to February. Main features of the observed vertical propagation of the individual waves of ZWN 1 to 3, studied at 51°N, can be summarized as follows:

- The observed time scale of the vertical propagation from the middle tro-

posphere to middle stratosphere decreases with increasing wave number. The propagation time is in the order of 4 days for ZWN 1, of 2–3 days for ZWN 2 and of 0–2 days for ZWN 3.

- The maximum coherence, which corresponds to the correlation coefficient, is higher for waves of ZWN 2 (between 0.4 and 0.6) than for waves with ZWN 1 and 3 (<0.4).

- Waves of ZWN 1 and ZWN 2 show a westward propagation with increasing height, whereas waves of ZWN 3 are quasi-stationary. The westward propagation is more pronounced for ZWN 1 than for ZWN 2.

Kaurola (1997) analyzed the vertical propagation characteristics of planetary-scale waves in a control run of the GCM ECHAM3-T42 and found a good agreement of main features between observational data and the climate model.

Randel's (1988) analyses did not indicate a downward propagation of wave-like anomalies from the stratosphere into the troposphere. The cross-spectral correlation analysis of Randel (1987) is not a suitable method for identifying the most important patterns of tropospheric circulation, which exaggerate wave-like disturbances of different spatial scale in the stratosphere because the propagation characteristics were studied on a two-dimensional plane. Cheng and Dunkerton (1995) used rotated SVD analysis to illustrate the associated patterns of the NH 50- and 500-hPa geopotential height fields, when the time series of the troposphere lead the stratospheric time series by four days. They determined two coupled modes, in which the datasets were filtered neither spatially nor temporally. They did not considered that planetary waves are selectively reflected at supercritical velocities (Charney and Drazin, 1961) and are characterized by different upward propagation times (Randel, 1988).

Baldwin and Dunkerton (1999) identified a downward propagation of the "AO signal" during high winter on the basis of 90-day lowpass-filtered data. They defined the structure of the AO as first EOF of the 3-dimensional geopotential height field. The very strong filtering applied in their study was necessary for the sake of identifying the 3-dimensional AO signal. So far, it has not been well understood which dynamical processes are involved in the downward control or which regions in the troposphere are significantly affected by modifications in the strength of the stratospheric polar winter vortex.

The main goal of this chapter is to isolate characteristic features of the vertical propagation of wave-like disturbances on the basis of observational data. Corresponding to our SWAN concept, we will examine the following two questions in more detail: Which disturbances of the tropospheric circulation exaggerate waves of ZWN 1 and 2 in the lower stratosphere (Section 5.3)? Is it possible to

find evidence for a downward propagation of waves from the stratosphere into the troposphere (Section 5.4)?

5.2 Applied Approaches

CCA was applied as a lag-correlation technique in order to isolate the coupled modes of variability in NH 50- and 500-hPa geopotential height fields, that characterize the relationship between tropospheric and stratospheric circulation. The slightly lowpass[1] filtered (>10 days) time series of the cold-season months (November to April) were used. We carried out a series of CCAs consisting of different analyses by varying the time lag $(\ldots, -10, -9, \ldots, 0, \ldots, 9, 10, \ldots)$ between the time series of the 50 and 500-hPa height fields. In this way, we determined the time lag at which both fields are maximally correlated. Taking the stratospheric field as reference level, a time lag of -10 (10) indicates that the tropospheric (stratospheric) time series leads the stratospheric (tropospheric) by 10 days. With the help of CCA, maximally correlated canonical variables of the two datasets were isolated. The canonical correlation coefficient, r_{CCA}, was the parameter compared between the various analyses at different time lags. This parameter $r_{CCA}(lag)$ is the unambiguous measure of the maximum correlation indicating the time lag of maximally related anomaly patterns of the 500- and 50-hPa geopotential height fields ($r_{CCA}(lag)$=max). We used the sign of the time lag to draw conclusions about the direction of the relationship between tropospheric and stratospheric circulation described by the respectively associated anomaly patterns. That is, $r_{CCA}(lag)$=max at a positive time lag indicates the influence of the stratospheric circulation on the troposphere and vice versa.

In the NH stratosphere, waves mainly of ZWN 1 and 2 are important. It is known that they have their origin in the troposphere. Randel (1988) showed that waves of ZWN 1 and 2 are able to propagate into the stratosphere. We studied the modes of tropospheric circulation which exaggerated waves of ZWN 1 and 2 in the stratosphere. For this analysis we used the stratospheric geopotential height field recomposed by waves of ZWN 1 as described in Section 2.2.2 (Equation 2.47) and the original (not spatially filtered by Fourier harmonics) 500-hPa heights. The same analysis series was carried out for the recomposed ZWN 2 field of 50-hPa heights. For the investigation of downward propagation of spherical wave-like anomalies, additionally, the tropospheric field was spatially filtered by harmonic analysis.

We analyzed the cold-season months November to April. For each cold season, the time series of the stratospheric field were fixed. They start on November 16th

[1]The lowpass filtered daily data were determined on the basis of the 21-point filter by Blackmon and Lau (1980).

and end on April 14th which means 150 realizations of low-pass filtered (>10 days) data. The tropospheric 150-day time series for each season were temporally lagged relative to the fixed stratospheric time series from -15 to 15 days. For instance, at a lag of -15 (15) days, the tropospheric time series start on November 1st (December 1st). The mean seasonal cycles were removed and the grid-point time series were weighted with the square root of the cosine of the latitude prior to the analyses.

5.3 Tropospheric Circulation Modes and Stratospheric Wave-like Disturbances

The zonal mean flow in the stratosphere is mainly disturbed by waves of ZWN 1 and 2, with waves of ZWN 1 having a larger amplitude than waves of ZWN 2. The maximum standard deviations of the amplitudes at the 50-hPa level in the NH, determined on the basis of daily data, amount to 150 and 100 gpm for ZWN 1 and ZWN 2, respectively. The total variability of the 50-hPa height fields (north of 30°N) recomposed by these single waves, can be almost completely (about 90%) described by two EOFs.

The two leading EOFs of the ZWN 1 field have approximately the same structure as the second and third EOF derived for the cold-season monthly means (Figure 4.3b and 4.3c). The first EOF of the ZWN 1 field accounts for 56% of total variance. The two centers of action of this EOF are located between 50° and 80°N with one center over North America (80°–120°W) and the other one over Eurasia (60°–100°E). The temporal variability of this mode is very important for the understanding the variability of the stratospheric circulation over North America, because more than 60% of the total (not spatially filtered) variability of the 50-hPa height time series is explained by this mode over that region. This fraction is considerably smaller for the second (Eurasian) center of action of the first EOF. About 35% of the original variability over Eurasia can be locally explained by waves of ZWN 1. The positions of the two mid-latitude centers of the second mode are shifted in zonal direction by 90° owing to the constraint of spatial orthogonality of higher EOF modes.

The first EOF of the spherical ZWN 1 field explains more variability (56%) than the second EOF (33%). In general, both EOFs are necessary to describe the real phase and amplitude of this zonal wave at a specific realization in time. We examined in more detail whether the much larger fraction of variability is an indication of temporal or spatial stationarity in the ZWN 1 field. In order to study spatial stationarity, the frequency distribution of the phases of ZWN 1 at 60°N was determined (Figure 5.1a). We calculated this phase for each realization in time of our cold-season sample and counted how often the phase occurs in

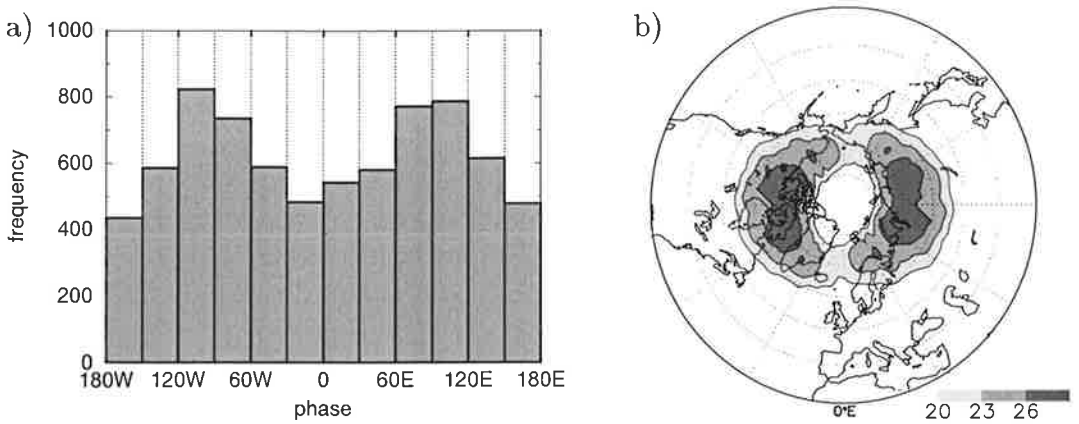

Figure 5.1.
(a) Frequency distribution of the phase of ZWN 1 of 50-hPa geopotential heights at 60°N. Longitudinal 30°-intervals were used for counting. The phase describes the longitude of the maxima.
(b) Number of events per 10 years (cold seasons) with a duration > 15 days of positive and negative anomalies (larger than an absolute value of 75 gpm) of waves of ZWN 1 at the 50 hPa level.

longitudinal intervals of 30°. The frequency distribution (Figure 5.1a) has two maximum regions which have a longitudinal distance of about 180° and clearly correspond to the two centers of action of the first EOF.

Temporal stationarity was studied by determining the local persistence of positive and negative wave anomalies (Dole and Gordon, 1983). At each grid point north of 30°N, we calculated the duration of positive and negative anomalies of ZWN 1 larger than an absolute value of 75 gpm. This value represents 50% of the standard deviation of the amplitude of this wave at mid-latitudes. Figure 5.1b shows how often, within 10 cold seasons, the duration of positive and negative anomalies exceeds 15 days. This pattern also corresponds to the structure of the leading EOF of the ZWN 1 field because most persistent anomaly events can be observed at the longitudes of the two centers of action of this EOF.

The first two EOFs of the 50-hPa ZWN 2 field explain 51 and 39% of total variance, respectively. Similar to the stationary behavior of waves of ZWN 1, the spatial pattern of the first EOF corresponds to the structure of the frequency distribution of the phase of waves of ZWN 2 between 60° and 80°N (not shown). The first maximum of the phase can be found at about 0°E.

The CCA series, described in the next two subsections, were carried out in the phase space of the first two EOFs of the recomposed stratospheric wave field and of the first 10 EOFs of the total 500-hPa geopotential height field. In the latter,

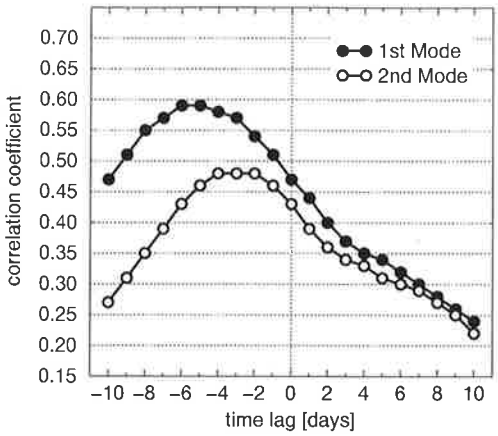

Figure 5.2. Canonical correlation coefficients ($r_{CCA}(lag)$) of the CCA series using the 500-hPa height field and the recomposed ZWN 1 height field at the 50-hPa level. A positive time lag indicates that the time series of the stratospheric field leads the time series of the tropospheric field and vice versa.

64% of total variance is explained by the first 10 EOFs. We found that the results are also robust even though a larger number of EOFs of the tropospheric field is considered.

5.3.1 Stratospheric Waves of ZWN 1

Two coupled modes can be isolated when CCA is applied in the phase space of the first two and the first ten EOFs of the stratospheric and tropospheric fields, in which the temporal expansion coefficients of the second coupled mode are ambiguously determined by the first mode. The values of r_{CCA} from the time lag of -10 to 10 days are illustrated in Figure 5.2. For both modes, the maximum values of r_{CCA} are clearly shifted towards the region of negative time lags. The graph of r_{CCA} of the first coupled mode exhibits a pronounced increase from 0.47 at lag 0 to 0.59 at a time lag of -5 to -6 days. The increase for the second mode is not as strong: $r_{CCA}(lag)$ amounts to 0.43 and 0.48 at a time lag of 0 and about -3 days, respectively.

The graph of $r_{CCA}(lag)$ indicates the expected influence of mid-tropospheric circulation on the structure of waves of ZWN 1 in the lower stratosphere. Figure 5.3 displays the associated regression and correlation maps of the first coupled mode of the '-5 days-lag CCA'. We regressed the standardized temporal expansion coefficients of the tropospheric canonical pattern onto the original time series of both the 500- and 50-hPa heights of the NH (north of 20°N). Thus, the regression coefficients represent the typical amplitude in [gpm] corresponding to the anomalies of one standard deviation of the index time series. The shading illustrates the squared correlation coefficients (in [%]) between the respective time series, which is a measure for the locally explained variance. Figure 5.3a exhibits the structure of a wave train covering the North America/North Pacific region. One center of action is located over Alaska, two anomaly centers of opposite sign are situated over North America between 50°and 70°N and near Hawaii. This wave train-like pattern at the 500-hPa level is most strongly linked to a ZWN 1

anomaly pattern in the lower stratosphere (Figure 5.3b) about 5 days later. The structure of the stratosphere is very similar to the first EOF of this field and results from the stationary behavior of the wave of ZWN 1 in the stratosphere. With the temporal expansion coefficient of the 500-hPa field more than 25% of the local variability of waves of ZWN 1 at the 50-hPa level can be explained in the two centers of action over North America and Eurasia. Over North America, even more than 25% of the original (spatially unfiltered) variability of 50-hPa geopotential heights is explained by the tropospheric expansion coefficient of the 500-hPa anomaly pattern (Figure 5.3a).

This result of the CCA series reveals that the stationary feature of waves of ZWN 1 in the stratosphere is affected to a large degree by a tropospheric mode of variability, characterized by a wave train-like pattern over the North America/North Pacific region. The propagation time of this anomaly structure from the 500- to the 50-hPa level amounts to 5 - 6 days. By comparing the associated patterns (Figure 5.3) a strong equivalent-barotropic increase in the anomalies over North America from the 500- to the 50-hPa level is apparent. The spatial structure of the coupled variability mode is very similar to the second coupled mode determined by Cheng and Dunkerton (1995). They applied rotated SVD to unfiltered daily data of the winter season (December to February), in which the tropospheric time series leads the stratosphere by 4 days. The stratospheric pattern also has a large similarity to the second coupled mode determined by Perlwitz and Graf (1995) and Kodera et al. (1996). They used monthly and seasonal mean data, respectively. Both studies showed that on the interannual time scale, this mode is closely related to the SST in the tropical Pacific.

5.3.2 Stratospheric Waves of ZWN 2

The graphs of r_{CCA} of the two coupled modes in the stratospheric ZWN 2 field and the 500-hPa height field are given in Figure 5.4. Again the maxima are shifted towards negative time lags. The first mode shows a maximum value of 0.71, when the tropospheric field leads by 2 days.

The associated anomaly patterns of the first coupled mode of the '-2 days-lag CCA' are shown in Figure 5.5. These patterns describe a wave of ZWN 2 in the mid-troposphere as well as in the lower stratosphere. The phase of the 50-hPa ZWN 2 pattern exhibits a small westward shift of about 20 degrees relative to the 500-hPa pattern. This indicates the upward propagation of the energy of this zonal wave (Section 2.2.2). Figure 5.5b clearly corresponds to the leading EOF of the ZWN 2 field in the lower stratosphere. Thus, quasi-stationary waves with ZWN 2 remain nearly intact when propagating into the stratosphere.

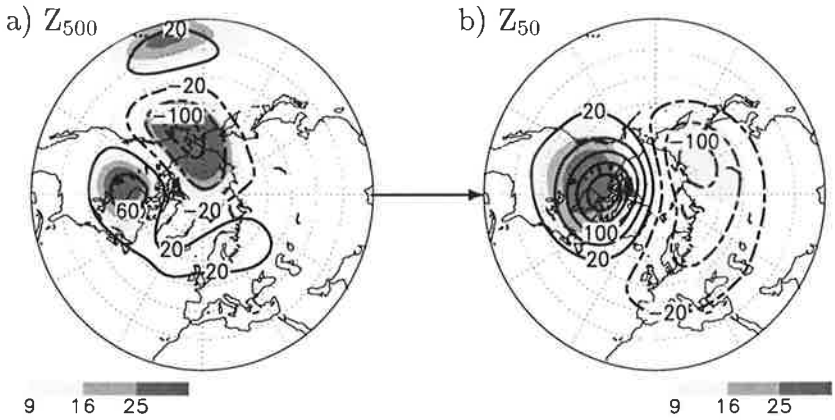

Figure 5.3. Maps of regression coefficients (isolines, [gpm]) and squared correlation coefficients (shading, [%]) for the first coupled mode of the '−5 day-lag-CCA' in which the ZWN 1 field at the 50-hPa height was used: The time series of the total both (a) 500- and (b) 50-hPa geopotential heights of the NH (north of 20°N) were regressed onto the standardized temporal expansion coefficient of the 500-hPa canonical pattern. The shading indicates where the locally explained variance exceeds 9, 16 and 25%. The arrow shows the direction of the relationship.

5.4 Downward Propagation of Stratospheric Waves

The previous analyses have elucidated the existence of a strong influence of the tropospheric circulation on the structure of wave-like disturbances of ZWN 1 and 2 in the lower stratosphere. Theoretical studies (e.g., Matsuno, 1970), as well as sensitivity experiments with GCMs (e.g., Kodera et al., 1996), indicate that in case of an anomalously strong polar winter vortex, planetary wave energy is

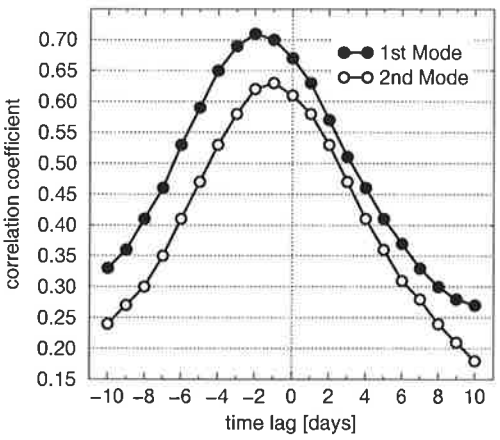

Figure 5.4. Canonical correlation coefficients ($r_{CCA}(lag)$) of the CCA series using the 500-hPa height field and the recomposed ZWN 2 height field at the 50-hPa level. A positive time lag indicates that the time series of the stratospheric field leads the time series of the tropospheric field and vice versa.

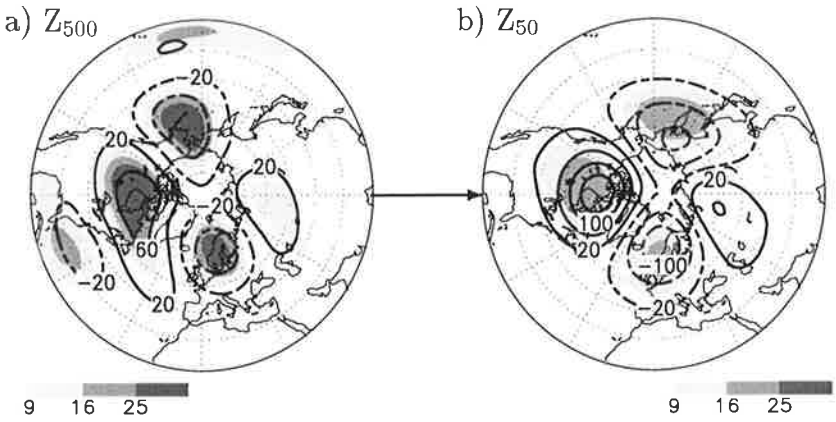

Figure 5.5. Maps of regression coefficients (isolines, [gpm]) and squared correlation coefficients (shading, [%]) for the first coupled mode of the '−2 day-lag-CCA' in which the ZWN 2 field at the 50-hPa height was used: The time series of the total both (a) 500- and (b) 50-hPa geopotential heights of the NH (north of 20°N) were regressed onto the standardized temporal expansion coefficient of the 500-hPa canonical pattern. The shading indicates where the locally explained variance exceeds 9, 16 and 25%. The arrow shows the direction of the relationship.

refracted both downwards and southwards. Using observational data, Kodera et al. (1996) showed that during winter seasons, characterized by an anomalously strong polar winter vortex, the equatorward propagation of tropospheric wave-like disturbances is increased. By our approach, no indications for a downward or southward propagation of wave-like circulation anomalies have yet been found. One reason may be the greater spatial variability of the tropospheric circulation which prevents the isolation of a wave-like signal in the mid-troposphere circulation induced by variations in the stratospheric circulation. It becomes additionally difficult to isolate such a relationship because the influence of the stratospheric circulation on the troposphere may only be weak. Therefore, we decomposed the 500-hPa geopotential height field in wave fields of single ZWNs and studied the relationships between the recomposed wave fields at the 500- and 50-hPa pressure levels. The analyses series were carried out for both the ZWN 1 and ZWN 2 fields. Corresponding to our SWAN concept, the motivation for this spatial filtering is the physical relationship, expressed in the Charney-Drazin Theorem. So we could make a pre-selection of single waves to reduce the noise caused by the wave-mean flow interaction. For these analyses, two and four EOFs were used for the stratospheric and tropospheric wave fields, respectively. The first four EOFs explain 80% - 85% of total variance in the tropospheric wave fields.

Next, the results of the analysis obtained of the cold-season months November to

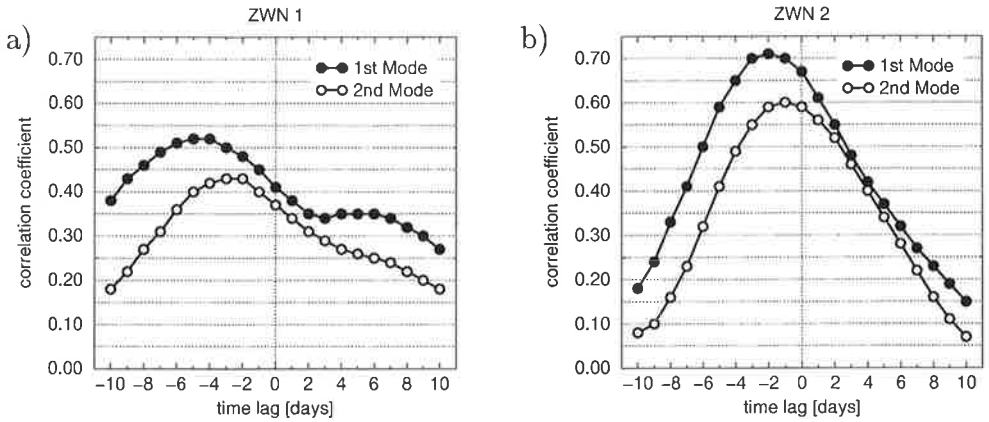

Figure 5.6. Canonical correlation coefficients of the CCA series of different time lags between the time series of the geopotential height fields at the 50- and 500-hPa levels, recomposed by waves of (a) ZWN 1 and (b) ZWN 2. A positive time lag indicates that the time series of the stratospheric field leads the time series of the tropospheric field and vice versa.

April will be described and the analyses for winter seasons (December to February), which are characterized either by an anomalously strong or anomalously weak polar winter vortex will be discussed.

5.4.1 Cold Season

Figure 5.6 shows the canonical correlation coefficients of the CCA series carried out for the time lag from -10 to 10 days. The main course of the graphs of $r_{CCA}(lag)$ both for the ZWN 1 and the ZWN 2 fields agree very well with the previous results (Figures 5.2 and 5.4), where the EOF-filtered 500-hPa height field was studied. The maxima obviously appear at negative time lags for both modes. We want to point out, however, a difference in the course of $r_{CCA}(lag)$ of the first coupled mode in the ZWN 1 analysis series. The graph does not show a continuous drop with increasing positive time lag but a saddle-region between the time lags of about 4 to 6 days ($r_{CCA} \approx 0.35$) before a further decrease of r_{CCA} occurs. This feature may indicate some weak influence of stratospheric waves on the tropospheric circulation.

Before examining the associated patterns corresponding to the saddle region, we will briefly discuss the results of the analyses when $r_{CCA}(lag) = max$. In this case, the time series of the 500-hPa wave field leads the time series of the 50-hPa field by about 4 days for waves of ZWN 1 and by 2 days for waves of ZWN 2.

The spatial structure of the associated patterns, determined for the '−2 days-lag CCA' of the ZWN 2 series (not shown), is very similar to the respective patterns of the previous analyses, based on the EOF-filtered 500-hPa height field (Figure 5.5). Again, the associated patterns exhibit a westward tilt of the waves with increasing height of about 20 degrees indicating that the coupled variability mode describes an upward propagation of wave energy of ZWN 2.

In the previous subsection, we illustrated that the preferred tropospheric mode exiting waves of ZWN 1 in the lower stratosphere exhibits the spatial structure of a wave train-like pattern. When only waves of ZWN 1 are studied, a different 500-hPa anomaly pattern in the '−4 days-lag CCA' appears. In Figure 5.7, the homogeneous regression pattern of the 500-hPa ZWN 1 field and heterogeneous regression pattern of the 50-hPa ZWN 1 field are shown, i.e. the time series of both ZWN 1 fields were regressed onto the standardized temporal expansion coefficients of the 500-hPa canonical pattern. The largest amplitudes of the wave field at the 500-hPa level appear between 50° and 70°N in which the maxima are located over the North Atlantic and Eastern Asia. At about the same longitude, wave anomalies with opposite sign are present at low latitudes. The maxima of the related 50-hPa ZWN 1 pattern by 4 days later are shifted westward relative to the maxima at the 500-hPa level by about 80°. It is also notable that the structure of the heterogeneous correlation pattern of the 50-hPa field exhibits an eastward tilt of the wave with increasing latitude. Thus, the process which is described by the first mode of the '−4 *days*-lag CCA' is the upward propagation of wave energy of ZWN 1 into the stratosphere where a southward propagation of this energy may occur. The propagation time from the 500- to the 50-hPa level amounts to 4 - 5 days.

The upward propagation of wave-like anomalies from the troposphere into the stratosphere is the dominating feature of the dynamical coupling between both atmospheric layers which could be isolated. However, the saddle-like feature in the decrease of r_{CCC} of the ZWN 1 CCA series may indicate some weak influence of the structure of stratospheric waves on tropospheric circulation. Figure 5.8 shows the associated regression patterns of the '5 days-lag CCA', i.e., the time series of the stratospheric field leads the time series of the tropospheric field by 5 days. In this case, we regressed the wave fields of both pressure levels to the standardized temporal expansion coefficients of the stratospheric canonical pattern. Most obvious is that the structure of the spherical ZWN 1 pattern is very different between the '−4 days-lag CCA' (Figure 5.7a) and '5 days-lag CCA' (Figure 5.8a), although the centers of action of the waves of ZWN 1 at the latitudinal belt from 50°to 70°N appears in both patterns. The 500-hPa pattern of the analysis with the positive time lag exhibits very clearly a eastward tilt of the waves of the ZWN 1 with increasing latitude. By comparing the vertical phase shift between both analyses, another remarkable difference between both analyses becomes obvious. The associated patterns in Figure 5.8 exhibit an

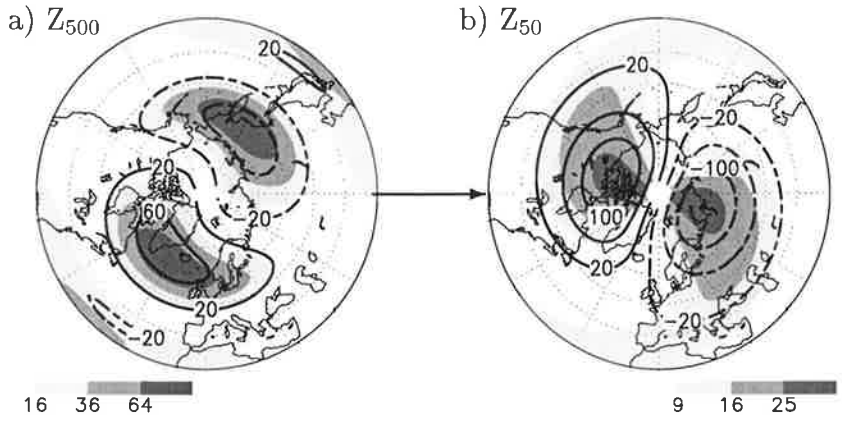

Figure 5.7. Maps of (a) homogeneous regression coefficients [gpm] of the 500-hPa ZWN 1 field and (b) heterogeneous regression coefficients [gpm] of the 50-hPa ZWN 1 field for the '−4 days-lag CCA'. The shading indicates the explained fraction of local variance of the recomposed ZWN 1 field in [%]. Please note the difference scaling of the color bars in (a) and (b).

eastward phase shift with increasing height, whereas in Figure 5.7 an westward shift appears. Therefore, the process which is described by the first mode of the '5 *days*-lag CCA' is the downward propagation of wave energy of ZWN 1 into the troposphere where a southward propagation of this wave energy occurs. The propagation time from the 50- to the 500-hPa level amounts to 4 - 6 days.

5.4.2 Different Winter Seasons

According to the Charney-Drazin Theorem, bifurcations of the vertical propagation of planetary waves exist at critical values (within critical regions) of the zonal mean zonal wind. That is, winter seasons characterized either by an anomalously strong or weak polar winter vortexes may differ in the propagation characteristic of vertically propagating waves. On the basis of cold-season daily time series, characteristic features of the up- and downward propagation of waves of ZWN 1 were isolated. Now, we will look for evidence of the existence of such a bifurcation of the vertical propagation of waves of ZWN 1.

For this investigation, the high winter months December to February were used. First, we defined an index for the strength of the stratospheric polar winter vortex. We used the temporal expansion coefficient of the first EOF of the NH 50-hPa geopotential height, determined on the basis of winter means ($\overline{\text{DJF}}$). The first mode of the EOF analysis represents very well the variation in the strength of the polar winter vortex (Kodera et al., 1996; Perlwitz and Graf, 1995, and Section 4.3

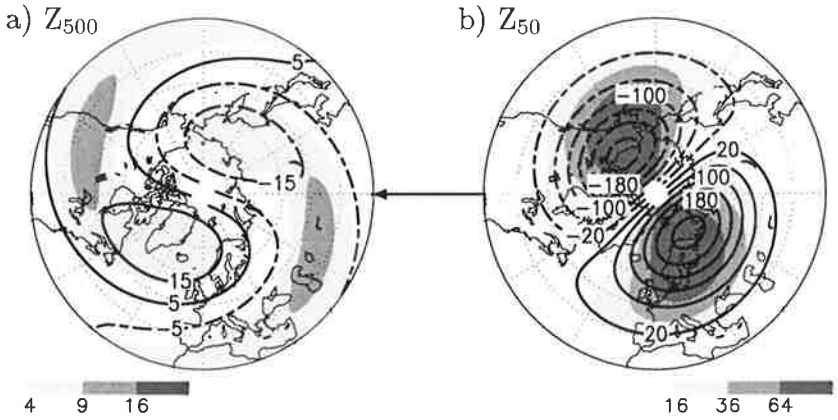

Figure 5.8. Maps of (a) heterogeneous regression coefficients [gpm] of the 500-hPa ZWN 1 field and (b) homogeneous regression coefficients [gpm] of the 50-hPa ZWN 1 field for the '5 days-lag CCA'. The shading indicates the explained fraction of local variance of the recomposed ZWN 1 field in [%]. Please note the difference scaling of the color bars in (a) and (b).

of this thesis). The standardized expansion coefficients of the first EOF are shown in Figure 5.9. We call winter seasons, characterized by an anomalously strong (positive index $> 0.5\,\sigma$) and by an anomalously weak (negative index $< -0.5\,\sigma$) polar winter vortex S-PVS (strong polar-vortex-season) and W-PVS (weak polar-vortex-season), respectively.

We composed the 10-day lowpass filtered time series of the NH 50- and 500-hPa geopotential heights of the winter months December to February (90 days), respective to the winter seasons of the S-PVS and W-PVS. Figure 5.9 indicates that the samples of the S-PVS and W-PVS for the observed time period from 1958–1999 consist of 13 and 15 winter seasons, respectively. Corresponding to

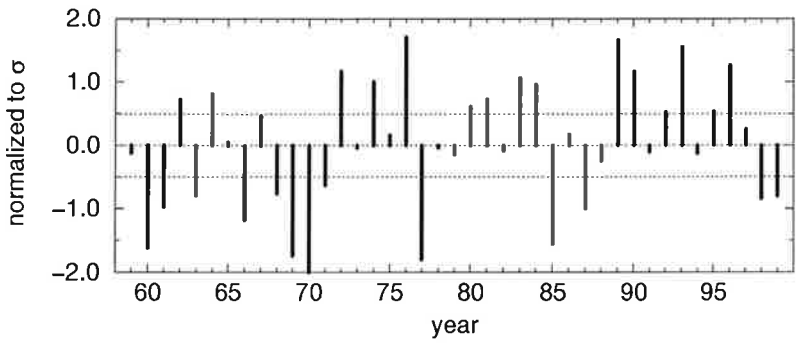

Figure 5.9. Expansion coefficients of the first EOF of the NH (north of 30°N) geopotential heights, determined on the basis of winter means ($\overline{\text{DJF}}$). The time series is normalized to the standard deviation (σ).

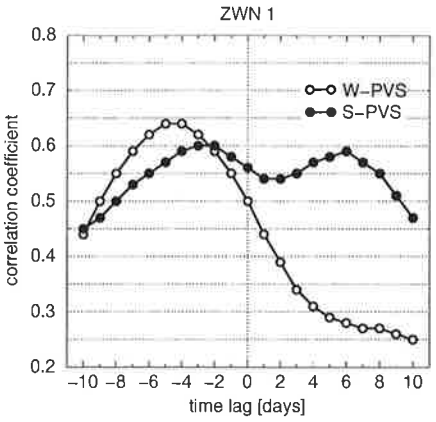

Figure 5.10. Canonical correlation coefficients of the CCA series of different time lags in the 50- and 500-hPa height fields, recomposed by waves of ZWN 1 for both the weak-polar-vortex seasons (W-PVS) and the strong-polar-vortex seasons (S-PVS). A positive time lag indicates that the time series of the stratospheric field leads the time series of the tropospheric field and vice versa.

the previous study of the sample of cold-season months, we carried out CCAs with different time lags for the recomposed 50- and 500-hPa ZWN 1 fields both for the S-PVS and W-PVS composites.

The correlation coefficients of the first modes of the two CCA series for ZWN 1 are shown in Figure 5.10. The most obvious difference between both graphs is the number of maxima. In the S-PVS, two maxima appear, one at a negative time lag of about −2 days and the other one at a positive time lag of about 6 days. In contrast, only one pronounced maximum in the W-PVS at a negative time lag of about −4 days can be seen. The latter shows a fast drop with increasing positive time lag. Hence, waves are not reflected by the stratospheric mean flow but can propagate without obstruction into the stratosphere in the case of the W-PVS whereas in the case of the S-PVS, waves are partly refracted down- and equatorwards. The downward propagation of waves of ZWN 1 from the 50- to the 500-hPa level takes about 6 days.

The interpretation of the differences in the course of the canonical correlation coefficients is supported by the structure of the associated patterns. The down- and equatorward propagation of waves of ZWN 1 in the S-PVS is illustrated in Figure 5.11 showing the associated patterns of the '6 days-lag CCA'. The structure of the patterns is very similar to the patterns of the corresponding analyses of the cold-season months (Figure 5.8). In the latter, the anomalies and explained local variances are smaller because the downward propagation of wave anomalies is not as relevant, when all cold-season months (November to April) are considered (including also the W-PVS).

Now, we will focus on the features of the associated patterns, describing the upward propagation of wave energy of ZWN 1. From Figure 5.10 it becomes obvious that the maximum at the negative time lags in the S-PVS appears earlier and is somewhat smaller than the maximum in the W-PVS. In addition, differences in the associated patterns become obvious. Figures 5.12 and 5.13 show the associated patterns for the '−4 days-lag CCA' in the W-PVS and the '−2 days-lag CCA' in the S-PVS. Comparing the westward tilt of the waves with increasing height, a

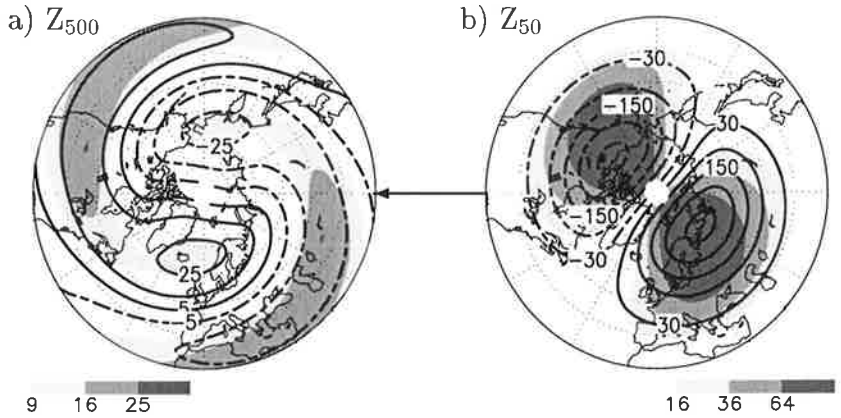

Figure 5.11. Maps of (a) heterogeneous regression coefficients [gpm] of the 500-hPa ZWN 1 field and (b) homogeneous regression coefficients [gpm] of the 50-hPa ZWN 1 field for the '6 days-lag CCA' in the S-PVS composite. The shading indicates the explained fraction of local variance of the recomposed ZWN 1 field in [%]. Please note the difference scaling of the color bars in (a) and (b).

smaller phase shift appears in the associated patterns in the S-PVS (about 50°) than in the W-PVS (about 80°) which corresponds to the faster propagation time in the S-PVS. The heterogeneous regression patterns of the 50-hPa geopotential heights of both composites also indicate that during the S-PVS, an equatorward propagation occurs (eastward tilt with increasing latitude), which is not observed in case of the W-PVS because the waves are not reflected by the mean flow.

5.5 Summary and Conclusions

The linear relationship between hemispheric-scale disturbances of mid-tropospheric and lower stratospheric circulation in the NH were studied using 500- and 50-hPa geopotential heights. We applied CCA in the phase space of the leading EOFs to the 10-day lowpass filtered time series of these two fields. This statistical method was used as a lag-correlation technique to find the time lag at which the closest relationship between the circulation in both atmospheric layers exists. New to this study is that, using the SWAN approach, the 50- and 500-hPa geopotential heights are decomposed into wave fields of individual ZWNs to take into account the selective refraction of vertically propagating waves by the mean stratospheric flow (Charney and Drazin, 1961).

We identified the modes of tropospheric circulation which propagate into the lower stratosphere and exaggerate waves of ZWN 1 and ZWN 2. Our results reveal that the vertical propagation of these disturbances is mostly relevant around 60°N. Quasi-stationary waves of ZWN 1 in the lower stratosphere are mainly

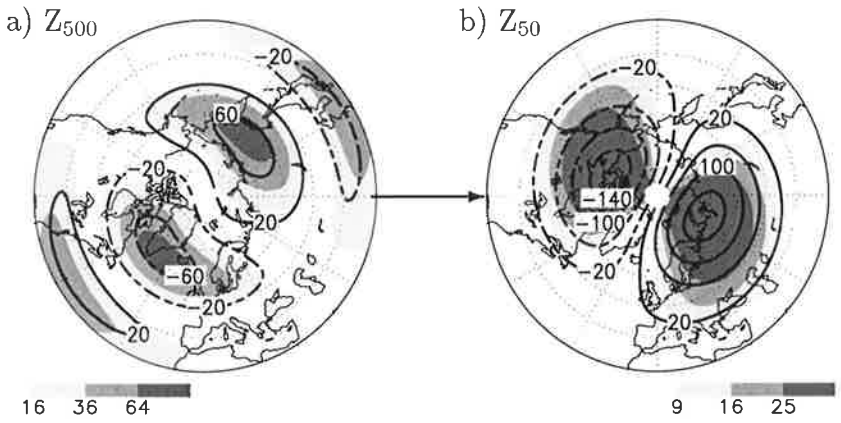

Figure 5.12. Maps of (a) homogeneous regression coefficients [gpm] of the 500-hPa ZWN 1 field and (b) heterogeneous regression coefficients [gpm] of the 50-hPa ZWN 1 field for the '−4 days-lag CCA' in the W-PVS composite. The shading indicates the explained fraction of local variance of the recomposed ZWN 1 field in [%]. Please note the difference scaling of the color bars in (a) and (b).

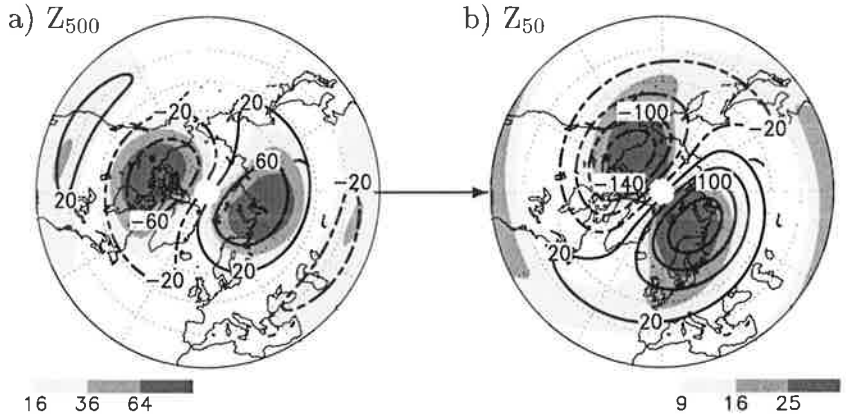

Figure 5.13. Same as Figure 5.12 but for '−2 days-lag CCA' in the S-PVS composite.

exaggerated by a wave train-like pattern which covers the North Pacific and North America. In contrast, quasi-stationary waves of ZWN 2 remain nearly intact when propagating into the stratosphere. We showed that a faster propagation time in the upward direction appears for waves of ZWN 2 (2 days) than for waves of ZWN 1 (4-5 days). The relationship between the tropospheric and stratospheric disturbances is smaller for waves of ZWN 2 ($r = 0.71$) than for ZWN 1 (r=0.59). The latter two features agree very well with the propagation characteristics of zonal waves at 51°N as derived by Randel (1987).

It is well known that an anomalously strong polar winter vortex leads to an increased southward refraction of wave energy (e.g., Matsuno, 1970; Boville, 1984; Kodera et al., 1996). We isolated in observations a coupled mode of wave-like disturbances which describes the downward- and equatorward propagation of wave-like anomalies of ZWN 1. This feature results from the refraction of wave energy by the stratospheric mean flow. It cannot be isolated as a clear local maximum in the graph of the canonical correlation, but is seen as a saddle-like feature when the time series of the stratospheric field leads the time series of the tropospheric field by 4 - 6 days. By studying the vertical propagation of waves of ZWN 1 during different winter seasons, the feature of the refraction of waves of this ZWN 1 could be isolated more clearly in seasons when the polar winter vortex is anomalously strong (S-PVS). In contrast, this process of refraction of wave energy is not important during winter seasons when the polar winter vortex is anomalously weak (W-PWS). We have also detected that both winter seasons differ in the propagation time for upward propagation of waves of ZWN 1. These propagation times (from the 500- to the 50-hPa level) amount to 2–3 and 4–5 days during the S-PWS and W-PWS, respectively.

The difference in the propagation characteristics for waves of ZWN 1 during the W-PVS and S-PVS has numerous implications:

- This finding fundamentally supports the implications of the Charney-Drazin Theorem about the existence of Rossby critical velocities for individual waves.
- A downward control of climate due to the reflection of vertically propagating waves of ZWN 1 exists *only* in the S-PVS.
- The exaggeration of an anomalously strong polar winter vortex may lead to non-linear changes in tropospheric winter circulation because the bifurcation point for the vertical propagation of waves of ZWN 1 is exceeded.
- The results manifest our theoretical understanding from theoretical studies. These should be held with some reservation as samples from 13 and 15 winter seasons may not be enough to *guarantee* that our results are statistically reliable.

Chapter 6

Relationship Between the Polar Winter Vortex and the Tropospheric Circulation

6.1 Introduction

It has been proposed that stratospheric circulation changes arising from natural stratospheric variability (as may be caused by the QBO and more continuously by the solar cycle) and anthropogenic effects (ozone depletion and increased greenhouse gas concentration) can be communicated downwards and amplified inducing significant perturbations of both the tropospheric circulation and climate (SPARC, 1993, 1998). The mechanism for such downward influence, which has been seen in model studies by Kodera et al. (1996), is the downward propagation of temporally averaged zonal-mean wind anomalies. The observational study by Baldwin and Dunkerton (1999) illustrated a downward propagation of the AO signal from the stratosphere to the surface. They defined the AO as the 3-dimensional EOF of the geopotential height. At stratospheric pressure levels, the AO pattern describes a variation in the strength of the polar winter vortex. In the troposphere, the pattern is less zonally symmetric, with a high latitude center of action shifted towards southern Greenland. The AO is described as a hemispheric scale phenomenon characterized by a strong zonally symmetric component (Thompson and Wallace, 1998, 2000). However, our previous study (Perlwitz and Graf, 1995) revealed that the strength of the stratospheric polar winter vortex is significantly related only to the circulation over the North Atlantic/Eurasia.

The dynamical processes most relevant for a downward propagation of strato-

spheric circulation anomalies and modification of this signal in the troposphere are not yet well understood. One key mechanism for the understanding of this downward control has been detected in the previous chapter. We have illustrated that waves of ZWN 1 are partly refracted down- and equatorward when the polar winter vortex is anomalously strong. In this chapter, we will discuss the linear relationship between the strength of the stratospheric polar winter vortex and the tropospheric circulation using daily geopotential height data at the 50- and 500-hPa pressure level. The 500-hPa heights, spatially filtered by EOF analysis (Section 6.3) and by Fourier harmonics (Section 6.4) were analyzed, and both the cold-season months November to April and winter seasons (December to February), characterized either by an anomalously strong or weak polar winter vortex, were investigated.

6.2 Analysis Methods

CCA in the phase space of the leading EOFs was applied, whereby this method was used as a lag-correlation technique. We analyzed 10-day lowpass filtered time series determined on the basis of the 21-point filter by Blackmon and Lau (1980). A CCA series consists of analyses with time lags from -30 to 30 days. Again, a positive (negative) time lag corresponds to a leading of the time series of the 50-hPa (500-hPa) heights.

The variation in the zonal mean field of geopotential heights is (due to the geostrophic balance) directly related to variations in the zonal mean zonal component of the geostrophic wind ($\bar{u}$). As shown in section 4.4, the leading EOF of $\bar{u}_{50}$ explains 72% of the total variance and describes the variation of the strength of the stratospheric polar winter vortex at the 50-hPa level. We studied the statistical relationship between the temporal expansion coefficients of this EOF and the time series of both the spatially unfiltered 500-hPa heights and the height fields recomposed by single waves of ZWNs 0 to 3. Because only the first EOF of the stratospheric field was considered, the approach of CCA reduces to a multiple regression analysis. The CCA series for the total 500 hPa height field was based on the first 10 EOFs (64%), whereas for the tropospheric wave fields of ZWNs 1 to 3, the first 4 EOFs were considered. They explain 81%, 86% and 90% of the total variability of the ZWN 1, 2 and 3 fields, respectively. The ZWN 0 field is derived from the zonal mean zonal component of the geostrophic wind ($\bar{u}_{500}$), where the first 3 EOFs of $\bar{u}_{500}$ (81%) are considered in this CCA series.

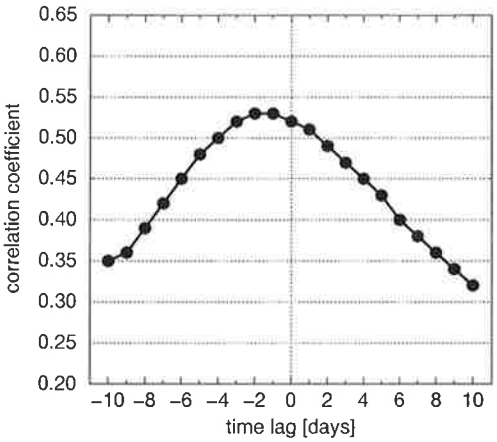

Figure 6.1. Canonical correlation coefficients ($r_{CCA}(lag)$) of the CCA series (from lag -10 to lag 10). The first 10 EOFs of the 500-hPa height field and the first EOF of $\bar{u}_{50}$ were used. A positive time lag indicates that the time series of the stratospheric field leads the time series of the tropospheric field and vice versa.

6.3 EOF-filtered 500-hPa Geopotential Heights

First, we will focus on the results of the CCA series, carried out for the total 500-hPa height field filtered by retaining the first 10 EOFs. The canonical correlation coefficients of this analysis series with different time lags (from -10 to 10 days) are shown in Figure 6.1. The maximum value of $r_{CCA}(lag)$ which amounts to 0.53 is found when the time series of the tropospheric field leads the time series of $\bar{u}_{50}$ by one to two days. However, this increase from lag 0 to lag -1 is very small and amounts to only 0.01.

Thus, by using the first 10 EOFs of the 500-hPa height field, it is neither possible to find clear evidence for a short time direct influence of the tropospheric circulation on the strength of the polar winter vortex, nor it is possible to find indications for an influence of the strength of the this winter vortex on the circulation at the 500-hPa level. There is just a small tendency for a leading tropospheric effect given by the slightly higher correlation coefficients at small negative time lags.

6.4 Single Tropospheric Waves

The tropospheric circulation is characterized by a large number of spatial degrees of freedom which makes it difficult to clearly isolate a signal from noise on the basis of 10-day lowpass filtered daily data. Therefore, we studied the relationship between the strength of the stratospheric polar winter vortex and the tropospheric circulation for single waves of the 500-hPa height field. Figure 6.2 combines the canonical correlation coefficients, $r_{CCA}(lag)$, of all individual analyses, i.e., for each ZWN (0–3) of the 500-hPa field and each time lag (-30 to 30). It becomes obvious that $r_{CCA}(0)$ for the waves of ZWNs 1 to 3 are small compared to $r_{CCA}(0)$ for $\bar{u}_{500}$. This means that ZWN 0 is the most important component. Figure 6.2 also reveals that r_{CCA} never exceeds 0.3. Thus, the relationship between the

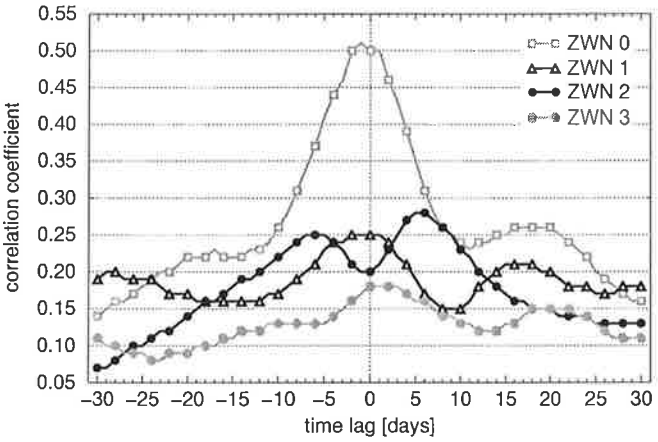

Figure 6.2. Canonical correlation coefficients of the CCA series (from lag -30 to 30) for the first EOF of the $\bar{u}_{50}$ and single tropospheric wave (0–3) fields. A positive time lag indicates that the time series of the stratospheric field leads the time series of the tropospheric field and vice versa.

strength of the stratospheric polar winter vortex and the fields of single ZWNs 1, 2 and 3 is smaller than the relationship between mid-tropospheric circulation and the lower stratospheric waves (Chapter 5). A correlation coefficient larger than 0.1, however, is significant at least at the 95% level. We will discuss relationships described by $r_{CCA} > 0.15$.

The graphs of the canonical correlation coefficients for the individual ZWN analysis (Figure 6.2) indicate that $r_{CCA}(0)$ decreases with increasing tropospheric ZWN from 0.50 for ZWN 0 to 0.18 for the ZWN 3. The graphs for ZWN 0 and 1 have their maximum value at lag 0. The center of the ZWN 3 graph is shifted slightly towards a positive time lag. A second local maximum is recognized at time lags from 15 to 23 days for tropospheric waves of ZWN 0 and ZWN 1 and at lags from 18 to 22 days for waves of ZWN 3. The ZWN 1 graph shows a further weak local maximum at a time lag of about -28 days. In contrast to the other wave fields, the graph of the ZWN 2 wave field, exhibits a local minimum at lag 0. The global maximum of 0.28 is found at a positive time lag near 6 days. A further local maximum region with a value of 0.25 can be found at lags near -6 days.

In order to better understand the relationship between the strength of the polar winter vortex, two additional aspects were considered: the differences between early and high winter season and the differences between the strong polar-winter-seasons (S-PVS) and weak polar-winter-seasons (W-PVS).

The early and high winter seasons were defined as 60-day periods, starting for the stratospheric time series at November 15 and January 15, respectively. Differences between both seasons were found mainly for waves of ZWN 2 and ZWN 3.

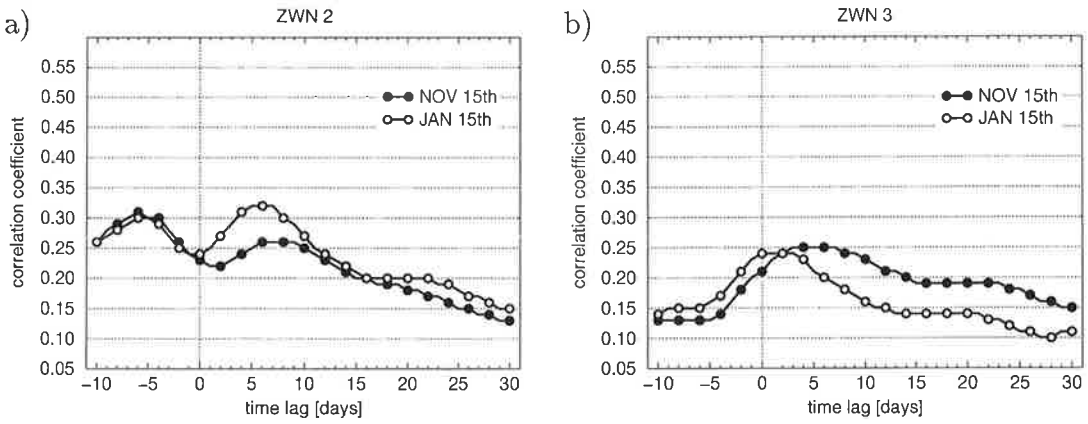

Figure 6.3. Canonical correlation coefficients as a function of time lag of $r_{CCA}(\text{lag})$ of the CCA series between the index of the first EOF of $\bar{u}_{50}$ and single tropospheric wave fields of 500-hPa geopotential height: (a) ZWN 2 and (b) ZWN 3. The early (60-day period beginning on November 15) and high winter season (60-day period beginning on January 15) were studied. A positive time lag indicates that the time series of the stratospheric field leads the time series of the tropospheric field and vice versa.

(Figure 6.3). The local maximum at the positive time lag for the tropospheric ZWN 2 field is higher in the high winter period than in early winter. For the ZWN 3 field, in contrast, a maximum at a positive time lag (3 to 7 days) clearly appears only in the early winter period. A reason for this different seasonal behavior of waves of ZWN 2 and 3 may be the varied sensitivity of the waves to the spatial distribution of zonal mean stratospheric flow (e.g., mean wind and vertical shear) (Charney and Drazin, 1961; Matsuno, 1970). Clearly, the polar night jet moves northward from the early to the high winter period so that the latitudinal effect in the Charney-Drazin relationship (Equation 2.34) may explain the observed differences.

In the previous chapter, we illustrated that the composites for an anomalously strong and an anomalously weak polar winter vortex exhibit different transmission-refraction properties for upward propagating waves of ZWN 1. Thus, a linear increase in the zonal mean zonal wind may be connected with non-linear changes in waves of ZWN 1 wave. As a consequence, linear methods, such as correlation analysis, applied to all cold-season months, my fail to isolate an influence of the strength of the polar winter vortex on this tropospheric wave. The non-linear aspects can be reduced by studying the linear relationship between both parameters for the composites of the S-PVS and W-PVS individually.

We carried out the CCA series (from lag -30 to 30) for waves of ZWN 0 to 3,

both for the composites of the S-PVS and W-PVS. The definition for the composites are given in Section 5.4.2. The canonical correlation coefficients are shown in Figure 6.4. Taking into account that a correlation coefficient larger than 0.3 is significant at least at the 95% level, the graphs for ZWN 1 of both composites (Figure 6.4b) exhibits a different behavior when the correlation coefficients for the positive time lags are compared. In the S-PVS, a significant correlation coefficient is persistent from lag 0 to lag 7 days, whereas in the W-PVS a significant relationship is found, when the stratospheric index leads by about 23 days.

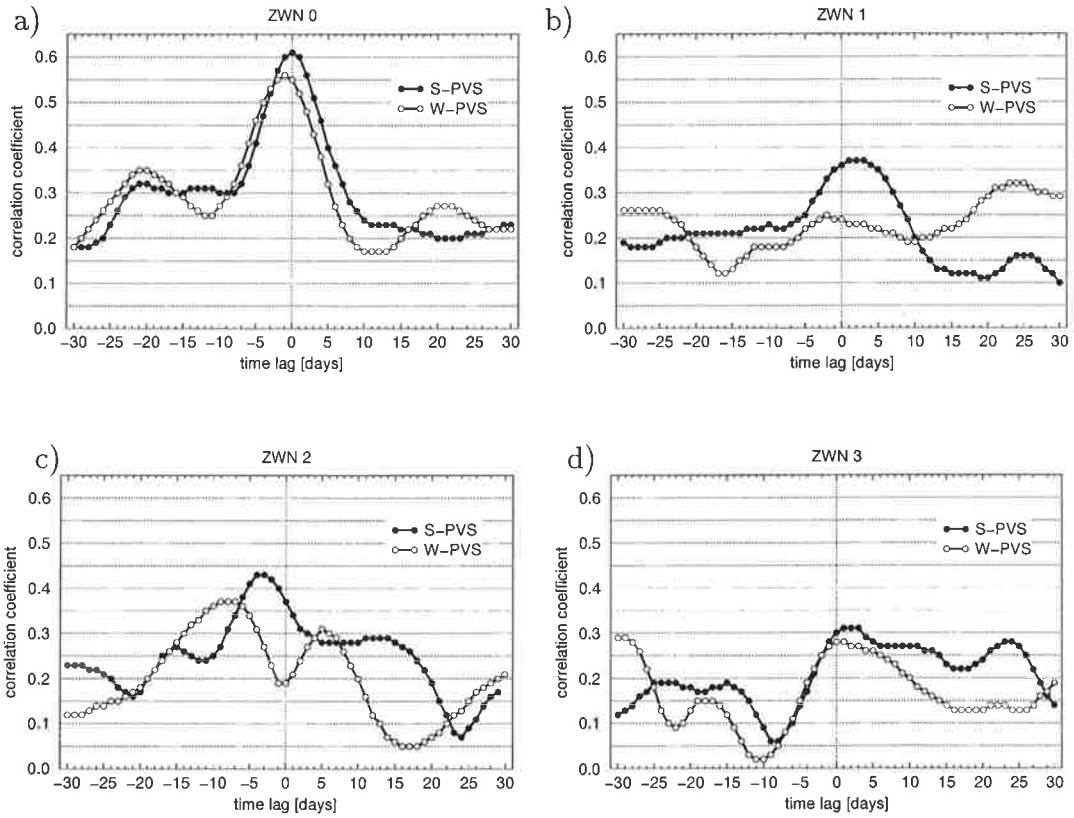

Figure 6.4. Canonical correlation coefficients as a function of time lag of r_{CCA}(lag) of the CCA series between the index of the first EOF of $\bar{u}_{50}$ and single tropospheric wave fields of 500-hPa geopotential height: (a) ZWN 0, (b) ZWN 1, (c) ZWN 2 and (d) ZWN 3. The composites of S-PVS and W-PVS were studied.

By comparing the graphs of the two composites for the other zonal wave numbers (Figure 6.4), the following features are notable: First, the graphs for the zonal mean zonal wind (ZWN 0) are very similar in which the maximum for the W-PVS is somewhat weaker and slightly shifted to negative time lags. Second, the maximum at negative time lags for ZWN 2 appears earlier during the S-PVS (−3 days) than during the W-PVS (−8 days). Only during W-PVS is a local minimum found at lag 0. Third, both for ZWN 2 and ZWN 3, the drop of r_{CCA}

with increasing time lag beginning at lag 5 is obviously faster in the W-PVS than during the S-PVS. However, the value of the persistent r_{CCA} during the S-PVS is slightly below the discussed significance threshold. Therefore, we cannot exclude that the third result will change when a larger database becomes available.

6.4.1 The Single Wave Patterns

Next we will turn our attention to the spatial patterns corresponding to particular maxima of r_{CCA}. The two maxima of r_{CCA} in the ZWN 2 analysis series indicate that, on the time scale of days, there is a significant (but weak in the global sense) two-way interaction between the strength of the stratospheric polar winter vortex at the 50-hPa level and waves of ZWN 2. To illustrate the physical mechanisms of this two-way coupling, the homogeneous regression patterns of tropospheric ZWN 2 field are shown for the '-6 days-lag CCA' and '6 days-lag CCA' in Figure 6.5. Both wave patterns clearly differ in their spatial structure. Figure 6.5a illustrates the ZWN 2 pattern, affecting the strength of the polar winter vortex by about 6 days later. The main center of action of this wave pattern is found between 45° and 55°N. This is the latitudinal belt where waves of this scale have maximum amplitude. In contrast, the wave pattern in the '6 days-lag CCA' (Figure 6.5b) exhibits a pronounced eastward tilt with increasing latitude and, hence, an equatorward propagation of energy of this planetary-scale zonal wave. The largest anomalies appear between 60° and 75°N. The heterogeneous regression patterns of the 500-hPa field for the '0 days-lag CCA' and the '6 days-lag CCA' (Figure 6.6) illustrate the main local effects in the troposphere by variations in the polar winter vortex. When the index of the stratospheric field leads by 6 days a significant fraction of local variance of waves of ZWN 2 can be explained at high latitudes. In contrast, a coherent variation (lag 0) in the strength of the stratospheric winter vortex and high latitude waves is not prominent.

Further, we examined the relationship between the strength of the stratospheric polar winter vortex and waves of ZWN 2 at the 500-hPa level at the two latitudes 50°N and 65°N separately. The variability of the ZWN 2 field at one latitude can be completely described by two EOFs. Taking these two EOFs, there is no subjective factor left in the analysis for choosing the number of tropospheric EOFs. The canonical correlation coefficients of both analysis series were determined for the time lags from -10 to 10 days. Figure 6.7 exhibits that the maximum of r_{CCA} in the analysis series for 50°N appears at a negative time lag of -5 to -6 days. In contrast, the maximum in the graph for the analysis series for 65°N, is found at a positive time lag of 5 days and very small values (< 0.1) are found at negative time lags. Thus, the results of the CCA series for the individual latitudes of waves of ZWN 2 in the mid-troposphere clearly support the hemispheric scale results for this wave: Mid-latitude waves of ZWN 2 in the troposphere influence the strength of the stratospheric polar winter vortex. The variation in the strength

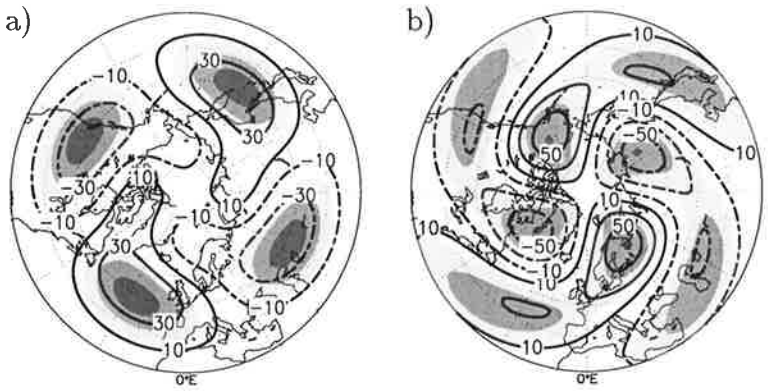

Figure 6.5. Homogeneous regression patterns of the waves of ZWN 2 of the 500-hPa geopotential height [gpm] for the analyses at different time lags. (a) -6 days and (b) 6 days. The light, medium and dark shadings indicate where the absolute correlation coefficients exceed 0.4, 0.6 and 0.8. The regression patterns correspond to the phase of a strong polar winter vortex.

of this vortex is closely related to the equatorward propagation of tropospheric wave anomalies of ZWN 2 and mainly affects the structure of these waves at high latitudes.

To illustrate how the structure of waves of ZWN 3 is modified by variations in the strength of the stratospheric polar winter vortex during the early winter season, we compared the heterogeneous regression and correlation patterns for the '0-lag CCA' and '5 days-lag CCA' (Figure 6.8). The center of action of waves of ZWN 3 appears between 50° and 60°N. In comparison to the pattern of the '0 day-lag CCA' (Figure 6.8a), the pattern for the positive time lag (Figure 6.8b) shows a westward phase shift by about 10° and both a slightly higher amplitude and a larger fraction of explained local variance at the centers of action. Additionally, CCA series for the single latitude of 50°N were carried out. The results of this CCA series support the results of the hemispheric scale analysis (not shown). Thus, the structure of waves of ZWN 3 at mid-latitudes is influenced by variations in the strength of the stratospheric polar winter vortex.

A physical interpretation of the structures of the ZWN 1 at the local maxima in the graph of r_{CCA} when the whole cold-season months are studied is more difficult. We compared the heterogeneous regression patterns of the '0 days-lag CCA' and '16 days-lag CCA' (Figure 6.9). Both patterns have a very similar structure. Larger anomalies appear for the lag 0 analysis. Using a linear statistical approach, we did not find any influence of the strength of the stratospheric polar winter vortex on the structure of the tropospheric waves of ZWN 1.

A significant influence becomes obvious when the winter seasons, characterized

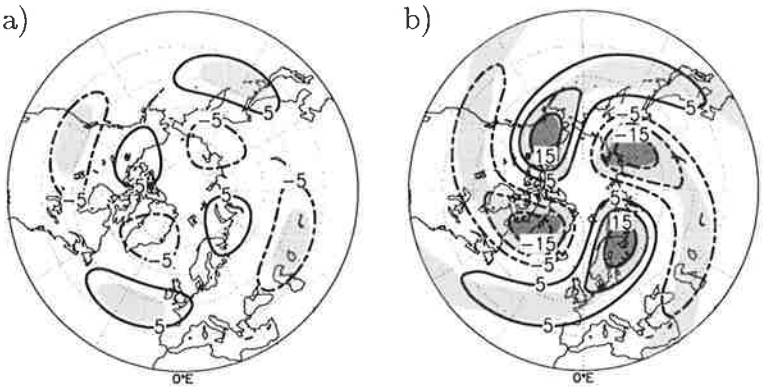

Figure 6.6. Heterogeneous regression patterns of the waves of ZWN 2 of the 500-hPa geopotential heights [gpm] for the analyses at different time lags. (a) 0 days and (b) 6 days. The light (dark) shading indicates where the absolute correlation coefficients exceed 0.2 (0.25). The regression patterns correspond to the phase of a strong polar winter vortex.

by an anomalously strong or weak polar vortex, are studied separately. Corresponding to the graphs in Figure 6.4b, we display the heterogeneous regression patterns of the ZWN 1 field for lag 0 and lag 3 for the S-PVS (Figure 6.10) and for lag 0 and and lag 23 for the W-PVS (Figure 6.11). In both seasons, but on different time scales, an influence of the strength of the stratospheric polar winter vortex on the structure of waves of ZWN 1 near 50°N can be detected. The heterogeneous regression patterns in both figures correspond to the phase of an anomalously strong polar winter vortex. By comparing the patterns of Figure 6.10b and Figure 6.11b, a different structure of the mid-latitude waves can be seen. Thus, an anomalously strong polar winter vortex during both seasons is significantly related to positive geopotential height anomalies over the central North Atlantic about three days later in the S-PVS, but to negative height anomalies over eastern North America about 23 days later in the W-PVS.

So far, our study has indicated that the the strength of the stratospheric polar winter vortex modifies the structure of tropospheric waves of ZWNs 1 to 3. In contrast, the closest relationship between the index of the stratospheric zonal mean field and tropospheric ZWN 0 field is found at lag 0 (Figures 6.2a and 6.4a). The zonal mean geopotential heights at the 500-hPa level regressed on the expansion coefficients of the tropospheric canonical pattern (Figure 6.12), exhibit a pressure seesaw between mid- and high latitudes and can be understood as an annular mode as discussed by Thompson and Wallace (2000). We conclude that the annular mode does not have a forecast potential for the tropospheric circulation when changes in the stratospheric circulation are observed because the highest correlations between variations in ZWN 0 both in the troposphere

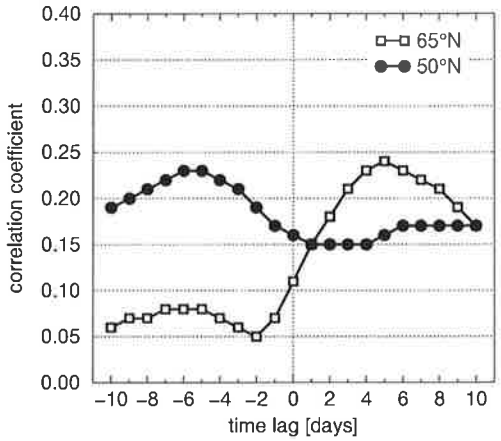

Figure 6.7. Canonical correlation coefficients as a function of time lag of $r_{CCA}(\text{lag})$ of the CCA series between the index of the first EOF of $\bar{u}_{50}$ and waves of ZWN 2 at the 500-hPa level at 65°N and 50°N.

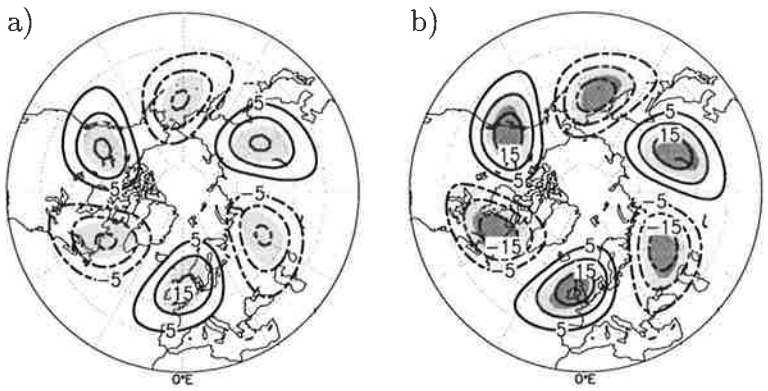

Figure 6.8. Homogeneous regression patterns of the waves of ZWN 3 of the 500-hPa geopotential heights [gpm] for the CCA analyses at different time lags in which the early winter season is studied. (a) 0 days, (b) 6 days. The light (dark) shading indicates where the absolute correlation coefficients exceeds 0.2 (0.25). The regression patterns correspond to the phase of a strong polar winter vortex.

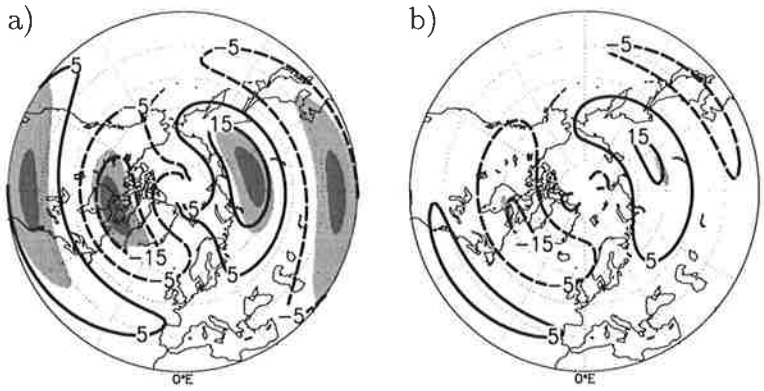

Figure 6.9. Heterogeneous regression patterns of the waves of ZWN 1 of the 500-hPa geopotential heights [gpm] for the CCA analyses at different time lags in which the cold season is studied. (a) 0 days, (b) 16 days. The light (dark) shading indicates where the absolute correlation coefficients exceed 0.2 (0.25). The regression patterns correspond to the phase of a strong polar winter vortex.

and in the stratosphere is found at lag 0. The forecast potential is achieved by the ultra-long planetary waves.

6.4.2 The Combined Pattern

We have shown that the strength of the stratospheric polar winter vortex significantly affects the structure of tropospheric waves. However, the influence of the strength of this polar vortex on the structure of hemispheric scale tropospheric circulation anomalies can hardly be imagined on the basis of the previous analyses. Because the meridional propagation of wave anomalies is involved, changes in the spatial structure only become visible when stronger temporal filtering is applied in addition to put higher weight on stationary features. On the other hand, a recomposition and superposition of the single wave effects, i.e., a process filter may also be successful. To elucidate the features of a hemispheric scale structural change of the tropospheric circulation, we performed the following analysis. First, the original time series were filtered in time by smoothing 10-day averages. Second, the resulting 500-hPa geopotential height fields were reconstructed by superposition of the waves of ZWNs 0 to 3. Third, the reconstructed time series were regressed onto the standardized index of the first EOF of $\bar{u}_{50}$ whereby the index time series was also filtered by determining smoothed 10-day averages. This analysis was carried out for the cold-season months (November to April).

Figure 6.13 shows the maps of the regression coefficients (isolines) and correlation coefficients (shading) for both lag 0 and lag 13. By comparing both regression

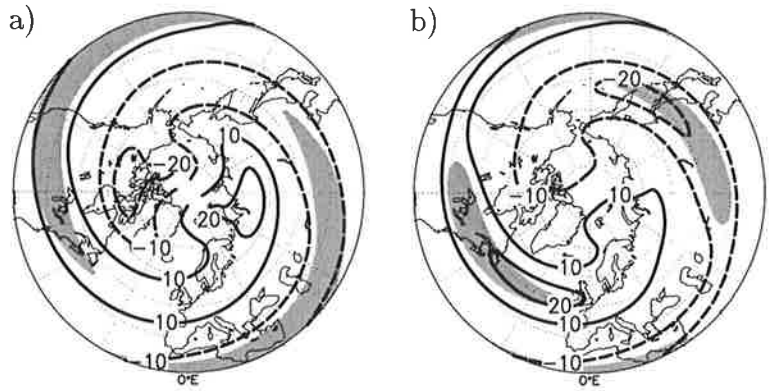

Figure 6.10. Heterogeneous regression patterns of ZWN 1 height field at the 500-hPa [gpm] for the CCA analyses in the S-PVS composites at different time lags. (a) 0 days, (b) 3 days. Shading indicates where the absolute correlation coefficients between the stratospheric index of the strength of the polar winter vortex and the time series of the recomposed ZWN 1 field exceeds 0.3. The regression patterns correspond to the phase of a strong polar winter vortex.

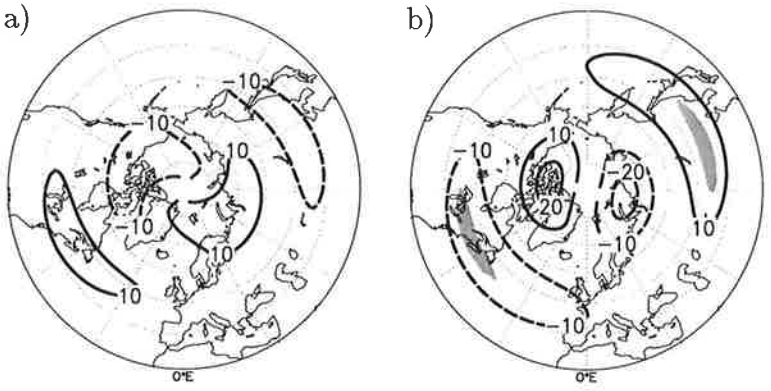

Figure 6.11. Heterogeneous regression patterns of ZWN 1 height field at the 500-hPa [gpm] for the CCA analyses in the W-PVS composites at different time lags. (a) 0 days, (b) 23 days. Shading indicates where the absolute correlation coefficients between the stratospheric index of the strength of the polar winter vortex and the time series of the recomposed ZWN 1 field exceeds 0.3. The regression patterns correspond to the phase of a strong polar winter vortex.

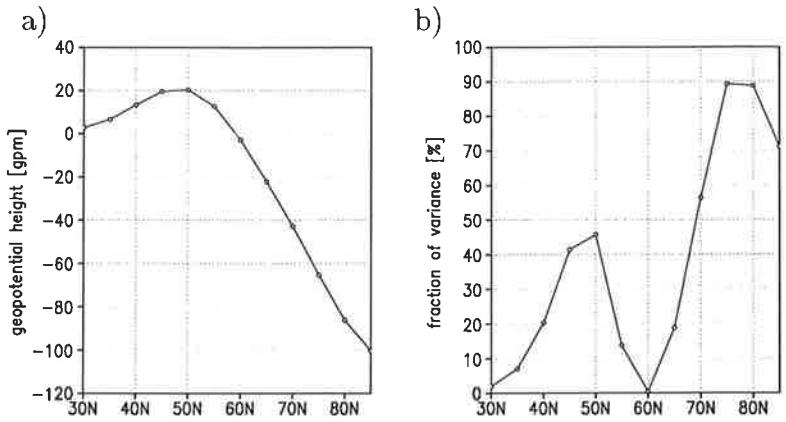

Figure 6.12. Graph of (a) regression coefficients [gpm] and (b) correlation coefficients (displayed as explained fraction of variance in [%]) between the zonal mean geopotential heights at the 500-hPa level and the temporal expansion coefficients of the canonical pattern of the '0 days-lag CCA'. The CCA were carried out between the ZWN 0 field of the 500-hPa heights and the first EOF of $\bar{u}_{50}$.

patterns, it becomes obvious that the circulation over the North Atlantic is mainly influenced. When the index of the polar winter vortex leads the time series of the 500-hPa field by about 2 weeks, a larger fraction of local variance over the North Atlantic is explained than when the simultaneous variation (lag 0) is studied. Thus, an anomalously strong (weak) polar winter vortex causes an intensified (weakened) pressure gradient over the mid-latitudes of the North Atlantic. This pressure seesaw over the North Atlantic corresponds to the features characterizing the well-known phenomenon NAO. Simultaneous with the change over the North Atlantic, the meridional pressure gradient over western Asia is affected. There is no recognizable influence on the circulation over the North Pacific. The correlation coefficients are smaller than 0.1 over this region when the index of the stratospheric field leads 13 days.

We examined the relationship between the strength of the stratospheric polar winter vortex and the mid-tropospheric westerlies over the North Atlantic in more detail. The centers of action, described by correlation coefficients larger than 0.3 (Figure 6.13, dark shading) can be found at high latitudes over the Davis Strait and at mid-latitudes to the west of Europe. We defined a 500-hPa NAO-index as the pressure difference between two grid-points in the centers of action: (10°W;50°N) – (60°W;70°N). On the basis of this index it is possible to determine time lag at which the closest relationship between the strength of the polar winter vortex and the 500-hPa-NAO appears. For this analysis, we used 10-day averages that did not overlap. The graph of the correlation coefficients from the time lags −30 to 30 are given in Figure 6.14. The maximum correlation coefficient (0.43) can clearly be seen at a time lag of about 13 days, i.e., the closest

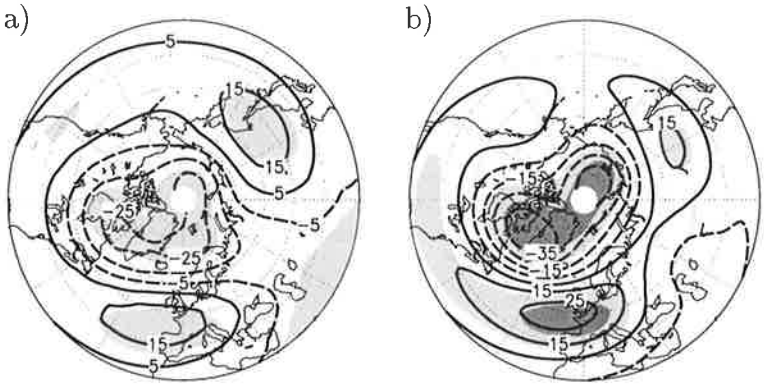

Figure 6.13. Maps of regression coefficients (gpm) between the standardized index of the polar winter vortex and the time series of the 500-hPa field, reconstructed by waves of ZWNs 0 to 3, smoothing 10-day averages. (a) 0-day lag analysis. (b) 13-day lag analysis The light (dark) shading indicates where the absolute correlation coefficient exceeds 0.2 (0.3).

relationship between the index of the strength of the stratospheric polar winter vortex and the 500-hPa NAO index is found when stratospheric index leads the NAO-index by 13 days. The same analysis was performed on the basis of the total 500-hPa field. The graph of correlation coefficients then exhibits similar results. That is, on the basis of 10-day averages, the variability of the 500-hPa geopotential height field is mainly caused by waves from ZWN 0 to ZWN 3. Therefore, the strength of the NAO or its tendency can (at least in part) be forecasted from the strength of the stratospheric polar vortex.

The origin of this relationship between the 500-hPa-NAO and the strength of the stratospheric polar winter vortex can be better understood when winter seasons characterized by an anomalously strong (S-PVS) or weak (W-PVS) polar winter vortex are studied separately. The correlation coefficients as a function of the time lag are shown for both composites in Figure 6.15, together with the graph determined on the basis of all winter seasons (December to February, 1958–1999). What emerges is that the forecast potential for the NAO results mainly from the *transition* from an anomalously weak to an anomalously strong polar winter vortex. Both seasons differ in the transmission-reflection properties for waves of ZWN 1. During winter seasons, characterized either by an anomalously strong or weak polar vortex, the influence of the tropospheric circulation dominates. However, there is a persistent relationship between the index of stratospheric polar winter vortex and the 500-hPa-NAO index during the S-PVS because significant correlation (>0.3[1]) are found from lag 0 to lag 10. In contrast, there is a fast decrease in the correlation coefficients from lag 0 to the increasingly positive time

[1]A correlation coefficient of 0.3 is significant at least at the 95% level.

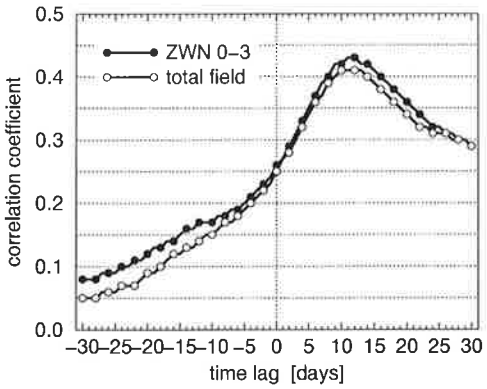

Figure 6.14. Correlation coefficients between the index and the 500-hPa-NAO as a function of time lag. Non-overlapping 10-day averages of the cold season (November to April) were used.

lag in the W-PVS.

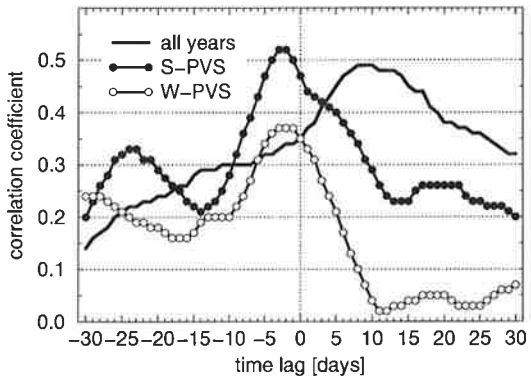

Figure 6.15. Correlation coefficients between the index and the 500-hPa-NAO as a function of time lag. Non-overlapping 10-day averages of the winter months (December to February) were analyzed for all years, and the composites of both the S-PVS and W-PVS.

6.5 Summary and Conclusions

The linear relationship between the strength of the stratospheric polar winter vortex and the tropospheric circulation has been studied by applying CCA as a lag-correlation technique to daily time series of the 50- and 500-hPa geopotential heights. From the investigation of this relationship for the single mid-tropospheric wave fields, relevant processes characterizing the dynamical coupling between troposphere and stratosphere during the cold season have been detected.

The results indicate that the structure of tropospheric waves of ZWN 2 in mid-latitudes significantly effects the strength of the polar winter vortex. We also showed that variations in the strength of the polar winter vortex modify the structure of tropospheric waves of ZWN 2 and ZWN 3. Waves of ZWN 2 are mainly affected at high latitudes during high winter, whereas a significant influence on the waves of ZWN 3 appears in mid-latitudes in early winter. The characteristic propagation time for this 'downward' effect is only a few days.

A significant influence of the strength of the polar winter vortex on the structure of waves of ZWN 1 could not be detected when all cold-season months (November to April) were considered. By studying the composites of the S-PVS and W-PVS seperately, significant links to the mid-latitude structure of this wave at the 500-hPa level were isolated for positive time lags. However, the characteristic time for the 'downward effect' is longer during the W-PVS (about 23 days) than during the S-PVS (3 days) and the phase of the tropospheric waves differs between the composites.

The study of Baldwin and Dunkerton (1999) implies that the strength of the polar winter vortex modifies the tropospheric circulation on a hemispheric scale similar to the pattern of the AO. We showed, however, that only the circulation over the North Atlantic and east Asia is significantly affected. This corresponds to our previous results (Perlwitz and Graf, 1995) when we studied the coherent variation in the tropospheric and stratospheric circulation on the basis of monthly mean values. Since the characteristic time scale of the downward influence is days to weeks, we had to fail in the previous study, however, to show clear evidence that the observed relationship is primarily due to changes in the stratospheric circulation.

The previous results lead to the following implications: First, the forecast potential of the strength of the stratospheric polar winter vortex for changes in the mid-tropospheric circulation does not result from change in the zonal mean zonal wind but from modification of the structure of tropospheric waves. Second, the strongest influence on the phase of the NAO appears when changes in the stratospheric flow lead to a modification of transmission-refraction properties for waves of ZWN 1. Third, a stronger mutual coupling between the stratospheric and tropospheric circulation may be expected in winter seasons in which waves of ZWN 1 are partly refracted downward and equatorwards (S-PVS).

Chapter 7

Coupled Modes of Variability and Interdecadal Climate Change

7.1 Introduction

For a description of the physical state of the atmosphere, we have to distinguish between "weather" and "climate". Weather is defined as the complete state of the atmosphere at a given instant. Thus, weather is continuously changing and is associated, for example, with the day-to-day variation of individual synoptic systems. Historically, climate is defined by the mean state ("averaged weather") of the atmosphere together with measures of variability or fluctuations such as the standard deviation or autocorrelation statistics for a specific period (e.g., season, year, decade or longer periods). Thus, climate is described by the PDF of elements characterizing the atmospheric state (e.g., near surface temperature). Using a more physically motivated characteristic, climate can also be described by the PDF of modes of natural climate variability superposed by noise (Palmer, 1993, 1999). Such fundamental climate variability modes (FCVMs) include information about the spatial and temporal structure of climate elements and give a more comprehensive view of the atmospheric state. As a consequence of this expanded definition of climate, its changes may be characterized not only by changes in the PDF of its atmospheric climate elements, but also by changes in the PDF of its naturally occurring FCVMs (Palmer, 1993). FCVMs can be estimated by applying multivariate statistical methods to datasets of one or more climate variables of interest. An approach for the estimation of nonlinear regimes of natural climate variability of NH circulation was proposed by Molteni et al. (1990).

The horizontal structure of recent climate change in the NH circulation is corre-

lated with the horizontal structure of modes of natural variability (Corti et al., 1999; Graf et al., 1995). In a previous study (Graf et al., 1995), we emphasized the strong similarity between the trend patterns of the winter season of NH 50- and 500-hPa geopotential height and the respective patterns of the leading coupled mode of the troposphere/stratosphere circulation. Corti et al. (1999) described the mid-tropospheric circulation changes during the cold season (November to April) in terms of changes in the PDF of naturally occurring regimes. They also showed that this behavior is consistent with the temporal development of the expansion coefficients (PCs) of the first two EOFs of the NH 500-hPa geopotential height field. The 10-year running average of the PCs of the second EOF exhibited a continuous increase during the analysis period (1949–1994). This EOF (Figure 4.4b, on page 45) is very similar to the circulation pattern which manifests the 'cold ocean warm land' (COWL) pattern (Wallace et al., 1996). The 10-year running average of the PCs of the first EOF exhibits a bias towards a positive index at the end of the analysis period.

In this chapter, we will study how the interdecadal circulation change is represented by a change in the coupled modes of variability of tropospheric and stratospheric circulation. An overview of these coupled modes in the NH in winter has been given in Section 1.2. In Perlwitz and Graf (1995), we applied CCA in the phase space of the leading EOFs to the 50- and 500-hPa geopotential heights on the basis of winter months December to February and isolated two coupled modes. For the analysis in this thesis, SVD analysis were applied to the cold-season monthly means (November to April). There are two reasons for using SVD analysis. First, we are mainly interested in the coherent variations in both fields. The covariance between two fields is maximized in SVD analysis. In contrast, CCA maximizes the temporal correlations between two fields. Therefore, we applied CCA in the previous chapter in order to isolated the direction of the relationship between tropospheric and stratospheric circulation. Second, SVD analysis has no user-specific parameter as CCA has in choosing the number of EOFs considered.

Different features of the coupled modes of variability in the 50- and 500-hPa geopotential height fields will be discussed. A main feature of this chapter is the comparison of the SVD results with the results of the EOF analyses separately obtained for the height fields at both pressure levels. The leading EOFs are patterns which describe maximum variance; they are not selected for physical reasons. We propose studying the coupled modes between the time series of both fields to increase the physical importance of these modes. During the cold season, tropospheric and stratospheric circulation are coupled by wave-mean flow interaction (Chapters 5 and 6). The stratospheric circulation exhibits a filter to tropospheric disturbances propagating into the stratosphere (Charney and Drazin, 1961). Thus, the leading coupled modes of the tropospheric and stratospheric quasi-stationary circulation may reflect not only a mathematical filtering

(by maximizing the covariance) but also a dynamical one and the hemispheric variability modes of atmospheric circulation are isolated in the context of specific physical processes as implicated by the Charney-Drazin theorem.

The following features are compared for the EOF- and SVD analysis results: the eigenvalue spectra (Sections 7.2), the spatial patterns (Sections 7.3) and the change in the PDFs of the temporal index values of the variability modes (Sections 7.4). The spectra and patterns of the individual EOF analyses have already been discussed in Section 4.3. In order to study the change in the PDF of the modes of variability, we projected the anomaly patterns of the 50- and 500-hPa geopotential height fields, which were *not detrended*, onto the singular patterns (SPs) and the EOFs of the respective fields. EOFs and SPs were derived from detrended data. The PDFs of these modes were estimated by determining the frequency distribution of occurrence of these projection coefficients. To stress the structural similarity between the patterns, the pattern correlation between the non-detrended anomaly fields and both the EOFs and the SPs were also determined. The modes of variability were determined for the period from 1958 to 1999 taken from NCEP reanalyses. In order to study the change in the PDF of these modes in the troposphere, the longer period 1949-1999 was used.

7.2 Spectrum of Eigenvalues

By applying simple EOF analysis to the 500-hPa geopotential heights of cold-season months, we isolated only one variability mode of the mid-tropospheric circulation (Section 4.3). Due to limited sampling size, higher modes could not be clearly separated from each other on the basis of 246 realizations (Figure 4.2 on page 44). However, it can be shown that the spatial structure of the second EOF is very robust when a longer analysis period (1949-1999) is studied. We determined the sampling errors of the eigenvalues of the cross-covariance matrix between the time series of the 500- and 50-hPa heights according to North's Rule of Thumb (Equation 2.9). In Figure 7.1, the spectrum of eigenvalues is shown together with their error bars. This spectrum indicates that not only the first, but also the second coupled variability mode, identified with the help of SVD analysis, can be very well separated from the next higher modes considering that all 246 realizations are independent. Since the persistence of the strength of the stratospheric polar winter vortex is larger than one month (Chapter 4), we also assumed (as a very conservative estimate) that only every second realization is independent ($N = 123$). Again, the first two coupled variability modes of tropospheric and stratospheric circulation on the monthly time scale are well separated from higher modes (not shown).

The first and second coupled mode explain 64% and 15% of the total squared

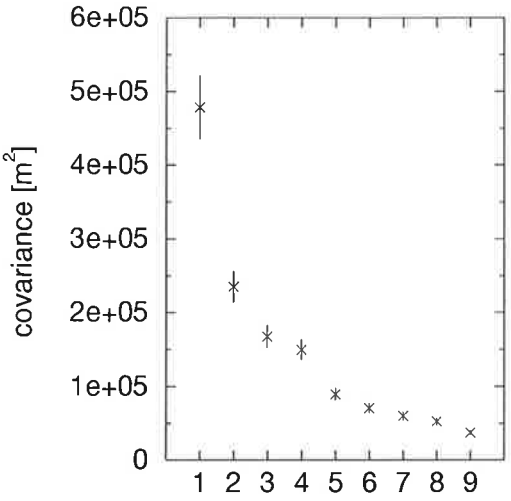

Figure 7.1. First 9 eigenvalues λ_i, together with their error bars, of the covariance matrix between time series of the NH 50 hPa and 500 hPa geopotential heights determined with SVD analysis.

covariance, respectively. It can be shown that the temporal expansion coefficients of the first and second coupled mode are not significantly correlated either for the 50- or the 500-hPa SPs, although this is not a constraint of the applied statistical method. The correlation coefficients amount to -0.05 (50-hPa SPs), and 0.09 (500-hPa SPs).

7.3 Spatial Patterns

Figure 7.2 shows the 50- and 500-hPa SPs of the first coupled mode of variability. These SPs can be directly linked to the EOFs (Section 4.3) of the individual fields because SVD analysis is a straightforward expansion of the EOF analysis. The EOFs of the 50- and 500-hPa field can be found in Figures 4.3a and 4.4a on page 45. In Appendix B.1, the homogeneous and heterogeneous regression patterns of the first and second modes are displayed.

The structural differences between the 50-hPa SP and the first EOF are small and only appear at mid-latitudes over western Europe and the North Pacific (Figure 7.2a). The differences in the respective patterns of the 500-hPa field are more pronounced. The main centers of action of the tropospheric SP are found over the North Atlantic and over eastern Asia (Figure 7.2b). In contrast, the first EOF of this tropospheric field has a more hemispheric-scale structure (Figure 4.4a) in which also the North Pacific is involved. The reason for this is that the variance is maximized by EOF analysis.

The related patterns of the first coupled mode are very similar to the respective analysis results of our previous study (Perlwitz and Graf, 1995). This coupled mode represents the well-known relationship between the strength of the stratospheric polar winter vortex and the circulation over the North Atlantic/Eurasia.

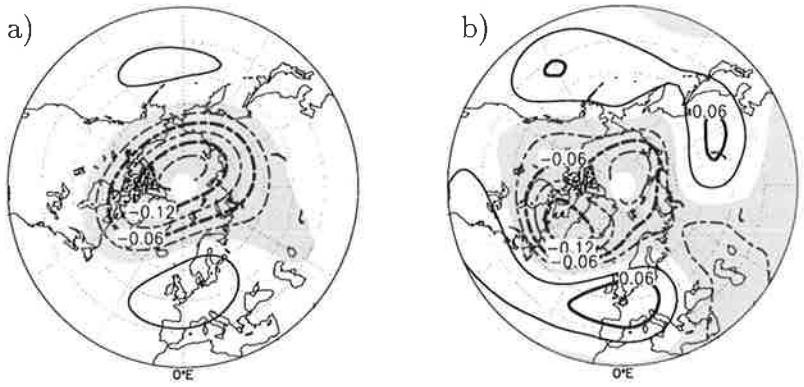

Figure 7.2. Singular patterns of the first SVD mode determined between the time series of the 50- and 500-hPa geopotential height fields of cold-season months. (a) 50-hPa and (b) 500-hPa geopotential heights.

In the previous chapter, it was shown, on the basis of daily data, that the circulation over the North Atlantic/Eurasia is affected by variations in the strength of the stratospheric polar winter vortex. Therefore, we conclude that the first SVD mode mainly describes this downward influence. The correlation between the temporal expansion coefficients is 0.61.

Now, we will focus on the spatial patterns of the second coupled mode. The 50-hPa pattern exhibits a superposition of wave anomalies of ZWN 1 and ZWN 2 (Figure 7.3a). The related tropospheric pattern shows two wave trains (Figure 7.3b). One reaches from the North Pacific over North America to the western North Atlantic. The second one covers the eastern North Atlantic, northern Europe and Asia. Together, these two wave trains exhibit a spherical wave-like structure of ZWN 2 at higher latitudes (north of 60°N). Considering the results of Section 5.3 for daily data, we conclude that this mode evolves from the upward propagation of tropospheric quasi-stationary disturbances into the stratosphere. The propagation time from the 500- to the 50-hPa level is about 2-6 days. On the monthly time scale, an equivalent-barotropic increase with height of the anomalies over North America and Scandinavia appears. This feature becomes obvious when comparing the associated anomaly patterns (Appendix B.1, Figures B.2b and B.2c). The correlation coefficient between the temporal expansion coefficients amounts to 0.73.

The difference between the spatial structures of the EOFs and SPs can be clearly illustrated by taking the EOFs as an orthonormal basis (Equation 2.3) and by determining how much of the spatial variability of the SPs can be explained by the leading EOFs of the corresponding field. The fractions of total spatial variance of the 50- and 500-hPa SP, which is explained by EOFs 1 to 9, are given in Figure 7.4. It becomes obvious that both the tropospheric and stratospheric SPs

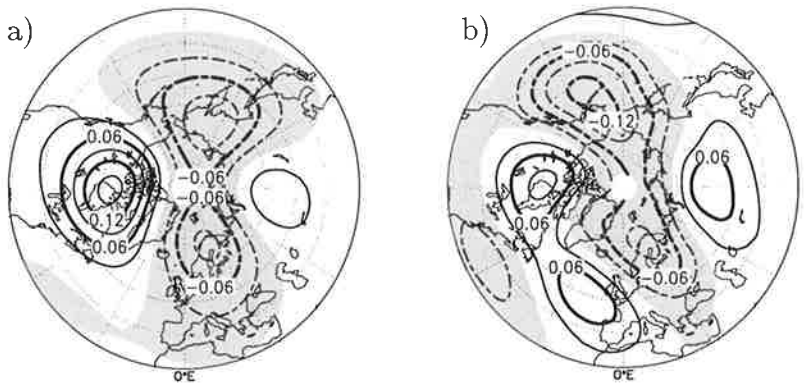

Figure 7.3. Singular patterns of the second SVD mode determined between the time series of the 50- and 500-hPa geopotential height fields of cold-season months. (a) 50-hPa and (b) 500-hPa geopotential heights.

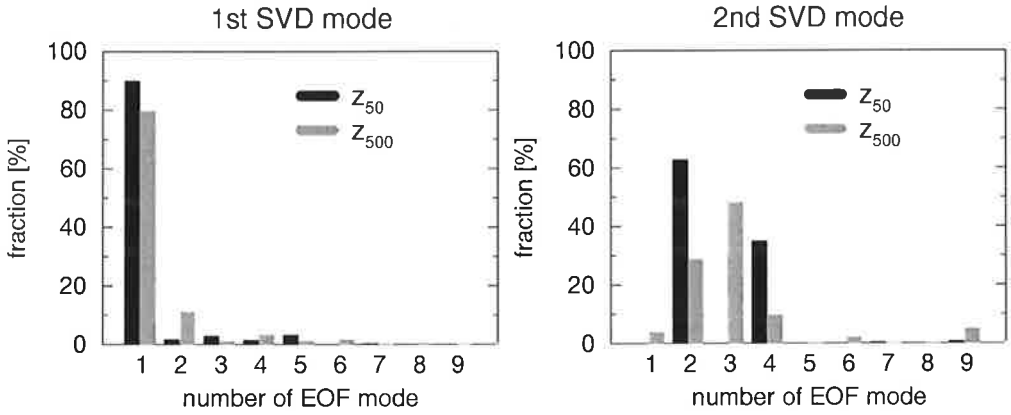

Figure 7.4. Fraction of total spatial variance [%] of the singular patterns of the 50- and 500-hPa geopotential height fields explained by the individual EOFs 1 to 9 of the respective fields. (a) 1st SVD mode, (b) 2nd SVD mode

of the first SVD mode are very similar to the leading EOFs of the respective fields (Figure 7.4a). This similarity is stronger for the stratospheric pattern than for the tropospheric one, for which the second EOF of the 500 hPa also contributes to the structure of the SP (12%). In contrast to the SPs of the first coupled mode, the patterns of the second coupled mode cannot be attributed to mainly one EOF. Figure 7.4b reveals that the 50-hPa SP is a linear combination of the second and fourth EOF, the 500-hPa SP are recomposed by the EOFs 2 to 4.

The results of Chapters 5 and 6 reveal that the relationship between the tropospheric and stratospheric wave-like disturbances is closer than the relationship between the strength of the polar winter vortex and tropospheric ultra-long planetary waves. This feature is also reflected by the correlation coefficients between the expansion coefficients of the 50- and 500-hPa singular patterns of the first

two coupled modes determined on the monthly mean time scale. This value is higher for the second mode (0.73), describing the upward influence, than for the first one, reflecting the downward influence (0.61).

By comparing the statistical parameters (explained fraction of total squared covariance correlation coefficients between the time series) of the first two SVD modes it becomes obvious that the choice of analysis method may influence the structure of the "leading coupled mode". Using SVD analysis, the leading mode exhibits the downward relationship between the strength of the stratospheric polar winter vortex and the structure of tropospheric waves. With the help of the CCA, the correlation coefficients between the temporal expansion coefficients are maximized. Therefore, the second SVD mode describing the upward propagation of disturbances appears as the leading CCA mode, although only 15% of total squared covariance is explained. The CCA results, however, depend on the number of EOFs used for the stratospheric fields. Using only three EOFs as in Perlwitz and Graf (1995), the vertical propagation of wave-like disturbances in ZWN 2 is not considered. Only disturbances of ZWN 1 waves are considered. Therefore, the tropospheric pattern of the coupled mode in Perlwitz and Graf (1995) exhibits mainly the wave train over the North Pacific/North America whereas in the respective pattern of the SVD analysis a wave train over the North Atlantic/Eurasia also appears. In the latter analysis, there is a considerable contribution (more than 30%) of the fourth EOF to the stratospheric singular pattern.

7.4 Interdecadal Climate Change

Figure 7.5 shows the linear trends of the 50- and 500-hPa geopotential heights for the cold seasons (November to April average) from 1958 to 1998, determined on the basis of the FUB stratospheric data and NMC analysis, i.e., for these patterns *the NCEP reanalyses were not used.* The patterns of local linear trends show a high similarity to the main structures of the leading coupled mode in the stratosphere (Figure 7.2a). The polar vortex has intensified considerably. Main features of the horizontal structure of the change in the mid-tropospheric circulation agree with the center of action of the tropospheric SP (Figure 7.2b). Since 1958, the westerlies over the North Atlantic and the geopotential height over eastern Asia have intensified significantly.

We have isolated two coupled variability modes which reflect relevant features of the dynamical coupling between tropospheric and stratospheric circulation. Now, we will study how the climate change observed during the cold season of the last 4 decades is represented in the change in the PDF of these two coupled modes.

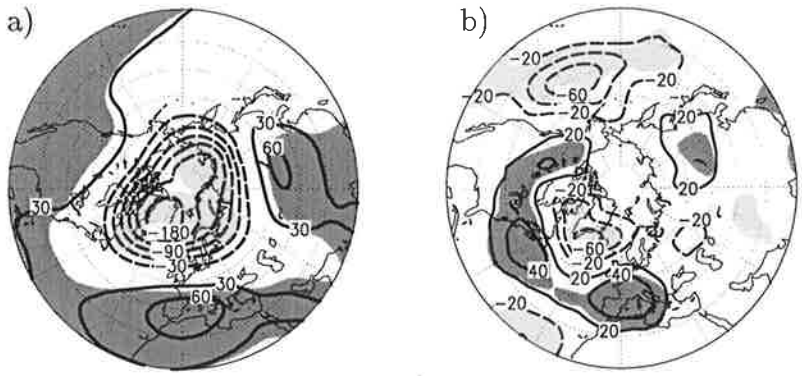

Figure 7.5. Patterns of local linear trend in [gpm/dec] of the cold season (average from November to April) for the 40-year period 1958-1998. (a) 50-hPa geopotential heights, FUB analysis, (b) 500-hPa geopotential heights, NMC analysis. The shading indicates where the local trends are significant at least at the 95% level (2-tailed t-test.)

7.4.1 First Coupled Mode

In order to illustrate the temporal development of the coupled variability modes since 1958, we calculated the projection coefficients between the not-detrended anomaly patterns and the singular patterns, which were calculated from detrended data. Figure 7.6 shows these index time series for both the 50- and 500-hPa geopotential height field. The time series were normalized respective to the mean value and the standard deviation of the 120 index values of the subperiod 1958/59–1977/78. A positive index of "one" corresponds to the patterns shown in Appendix B.1 (Figures B.1a and B.1c) (i.e. anomalously strong polar winter vortex at the 50 hPa level, anomalously strong westerlies over the North Atlantic at the 500 hPa level). The most obvious feature of both time series is the strongly persistent positive index, which can be observed from 1988/89 to 1996/97 in the stratosphere and to 1995/96 in the troposphere. To study the differences in the PDF of this coupled mode between the 20-year periods 1958/59–1977/78 and 1979/80–1998/99 in more detail, the frequency distributions of occurrence of the projection coefficients for both periods were determined (Figure 7.7). In order to evaluate, in addition, the change in the spatial structure during the last 4 decades, we also determined temporal indices of pattern correlations between the anomaly fields and the SPs. Pattern correlations only put stress on the spatial structure whereas changes in the mean of the anomaly patterns are not considered. The estimated PDFs of the correlation coefficients for both periods are shown in Figure 7.8.

Both histograms for the projection coefficients (Figure 7.7) indicate that the pos-

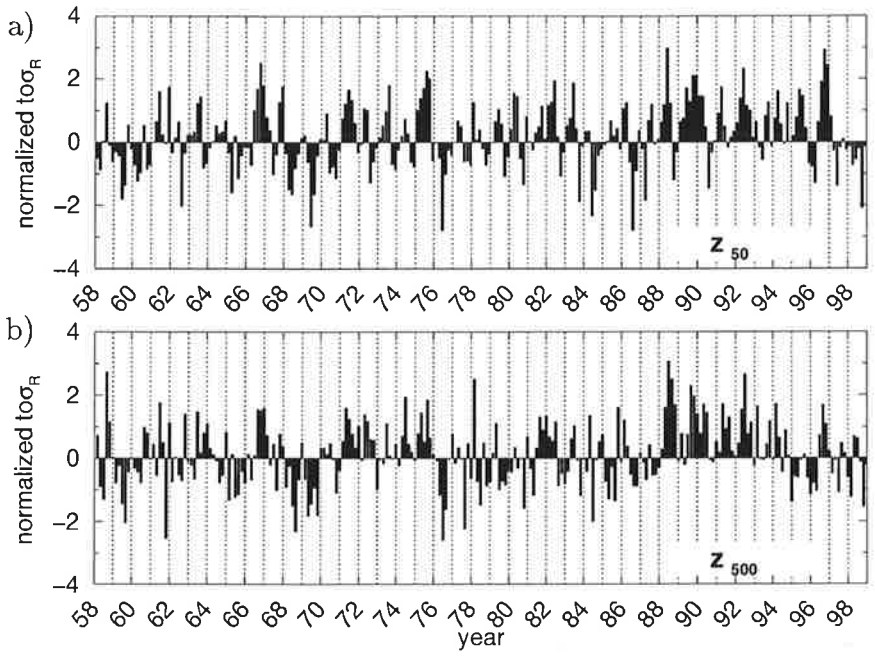

Figure 7.6. Time series of projection coefficients: The non-detrended anomaly fields of cold-season months were projected onto singular patterns of the first SVD mode of the respective field. (a) 50-hPa geopotential heights, (b) 500-hPa geopotential heights. The time series are standardized to the period 1958/59–1977/78.

itive phase (> 1) of the leading coupled modes is more often exited in the second period than in the first one, whereas the number of months with an anomaly pattern of the negative phase of this mode (< -1) is reduced. The changes in the excitation of the coupled mode are larger in the lower stratosphere than in the mid-troposphere. For both the 50- and 500-hPa height fields these changes are more clearly represented by studying the indices of the pattern correlations. Taking into account the results of Chapter 5, it can be concluded that the number of months when waves of ZWN 1 were refracted down- and equatorward increased during the period 1979/80 – 1998/99. This strengthened downward control was related to a change in the structure of tropospheric waves.

In order to compare both periods in more detail concerning the behavior at the tails of the frequency distribution, a parameter was defined that describes the ratio of positive and negative enhancements of the studied mode during an analyzed period. For the index time series of the projection coefficients, we determined the ratio ($R = N_{>1.0}/N_{<-1.0}$) between the number of months ($N_{>1.0}$), which have a positive index larger than 1.0, and the number of months ($N_{<-1.0}$) with a negative index that is smaller than -1.0. For the index time series of

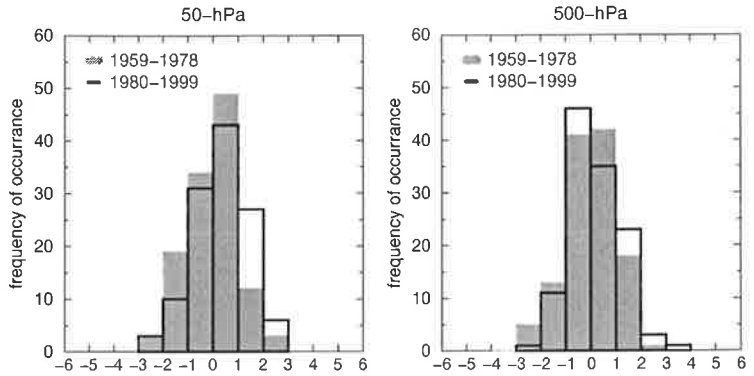

Figure 7.7. Histogram of the projection coefficients, shown in Figure 7.10. The PDF of the periods 1958/59 – 1977/78 and 1979/80 – 1998/99 are compared. (a) 50-hPa geopotential heights, (b) 500-hPa geopotential heights.

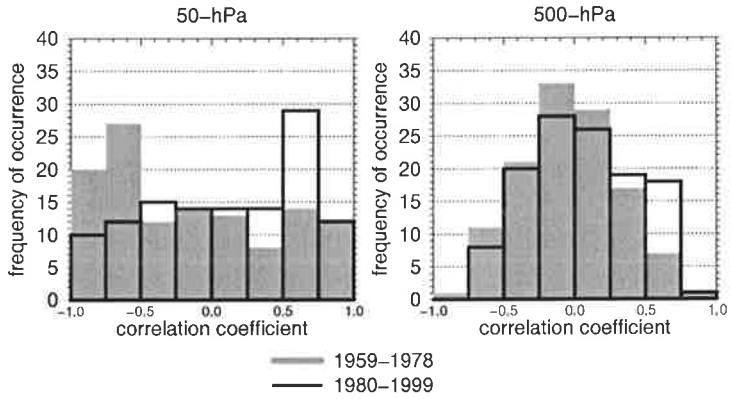

Figure 7.8. Histogram of the pattern correlation coefficients, determined as described in text. The PDF of the periods 1958/59 – 1977/78 and 1979/80 – 1998/99 are compared. (a) 50-hPa geopotential heights, (b) 500-hPa geopotential heights.

the correlation coefficients, the ratio $R=N_{>0.5}/N_{<-0.5}$ was used. The results for the 500-hPa SP are shown in Table 7.1. By comparing the linearized measures 'lg R', it becomes obvious that the change in the index of the pattern correlation is stronger than the change in the index of the projection coefficients.

We also calculated these indices of projection and correlation coefficients for the first EOF of the 500-hPa geopotential height fields and studied the change in the estimated PDFs of these indices by determined the ratios R given in Table 7.1. Clearly, the change in the indices of the SP is stronger than the change in indices of the EOF.

As in the study of Corti et al. (1999), we calculated the time series of the 10-year running averages of the projection coefficients of the first tropospheric variability mode, described by the SP (Figure 7.9) and the leading EOF. The not-detrended

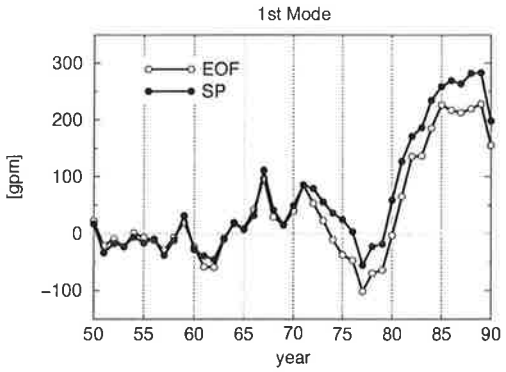

Figure 7.9. Time series of the 10-year running averages of projection coefficients. The non-detrended anomalies of the 500-hPa geopotential heights of cold-season months are projected onto 1st EOF (open circles) and 1st SP (filled circles) of the 500-hPa geopotential heights. The time series were centered on the sub-period 1950–1970.

anomalies of cold-season months from 1949 to 1999 were studied. Because the spatial average over all grid points is equal unity both for the EOFs and the SP, the time series can be directly compared. This time series shows the smoothed temporal behavior during the analysis period. The time series of SP exhibits a transition from high-frequency variations, which are very small by amplitude during the first decade, to a large low-frequency variation during the last 30 years. Corresponding to the previous analysis, the change in the index of the singular pattern is higher (about 20%) than the change in the index of the first EOF.

The previous analysis reveals that the leading coupled mode of tropospheric and stratospheric circulation better represents the features of the observed circulation change during the cold season than the leading EOF of mid-tropospheric geopotential height field.

7.4.2 Second Coupled Mode

The index time series and histograms of the projection coefficients of the second coupled variability mode are shown in Figures 7.10 and 7.11, respectively. A positive index of "one" in the projection coefficients corresponds to the patterns shown in Appendix B.1 (Figures B.2a and B.2c). The most obvious feature is an increase in the variance of the indices which is very pronounced in the index of the 50-hPa geopotential height field. The statistical parameters for the indices of the second sub-period[1] are 0.42 ± 1.48 (50-hPa heights) and 0.35 ± 1.20 (500-hPa heights). Thus, the increase in the mean value is accompanied by an increase

[1]The first period is standardized, i.e., the statistical parameters are 0.0 ± 1.0.

Table 7.1. Ratio R of positive and negative enhancements of the variability modes of the 500-hPa geopotential heights during the periods 1958/59–1977/78 and 1979/80–1998/99. The index time series of the projection and correlation coefficients of the first EOF and the first SP were considered.

	1958–1978		1979–1999	
	projection coefficients			
	$R^{(a)}$	$\lg(R^{(a)})$	$R^{(a)}$	$\lg(R^{(a)})$
SPs	$\frac{19}{18}$	**0.02**	$\frac{27}{12}$	**0.35**
EOFs	$\frac{19}{19}$	**0.00**	$\frac{22}{13}$	**0.23**
	correlation coefficients			
	$R^{(b)}$	$\log(R^{(b)})$	$R^{(b)}$	$\log(R^{(b)})$
SPs	$\frac{8}{12}$	**-0.18**	$\frac{19}{8}$	**0.38**
EOFs	$\frac{10}{11}$	**-0.04**	$\frac{14}{7}$	**0.30**

(a) $R = N_{>1.0}/N_{<-1.0}$,
(b) $R = N_{>0.5}/N_{<-0.5}$,

in the variance. Using the F-test (Sachs, 1992, pp 347–348), this increase in the standard deviations is significant at least at the 95% level. The changes in index time series of the tropospheric pattern are somewhat more pronounced when an earlier sub-period (1949–1969) is used to normalize the projection coefficients of the recent sub-period. Then the statistical parameters of the tropospheric index time series of the latter period amount to 0.39 ± 1.22, indicating a significant increase in the variance.

Studying the period 1949–1994, Corti et al. (1999) found that the smoothed 10-year averages of the temporal expansion coefficients of the 500-hPa EOFs for the second mode exhibit a continuous increase. We want to compare the temporal development of the 500-hPa indices of the second modes on the decadal time scale. Figure 7.12 shows the 10-year running means of the projection coefficients of the second EOF (Figure 4.4 b), and the second SP (Figure 7.2b). In contrast to the time series of the second EOF, which shows the known continuous increase, the time series of the second SP only increases until 1975. After that year the index varies around a value of 100 gpm. Thus, a continuous increase as in the COWL-circulation pattern has not been found in the index time series of the second coupled variability mode of the troposphere/stratosphere circulation system. The COWL-pattern is related to the air-sea interaction (Palmer, 1999) and a study of the coupled modes of the atmosphere-ocean system may show whether the second EOF is the physically optimized pattern for the description of this interaction. Such studies would exceed the scope of this thesis.

We have shown that the increase of the variance in the temporal expansion coefficients is an important additional feature which has characterized the inderdecadal change observed. We determined the smoothed 20-year standard deviations of the temporal indices for both the second EOF and the second SP. The time series in Figure 7.13 reveals that there is a continuous increase in the variations of the tropospheric temporal index of the second coupled mode. This behavior cannot be detected using the second EOF of the 500-hPa height field.

The present analysis has revealed that the second coupled mode of variability in the 50- and 500-hPa geopotential heights clearly differs to the second EOFs both in the stratosphere and the troposphere. This mode exhibits a strong increase in the variability of the projection coefficients of the coupled mode during the last four decades. The beginning of this increase of the index time series corresponds to the beginning of the incorporation of satellite data into the NCEP reanalyses (around 1978). Therefore, it is imaginable that the changes in the index of the second coupled mode are an artefact. However, we have shown that the temporal expansion coefficients of the second coupled mode agree very well with the respective indices based on a different dataset (Chapter 3).

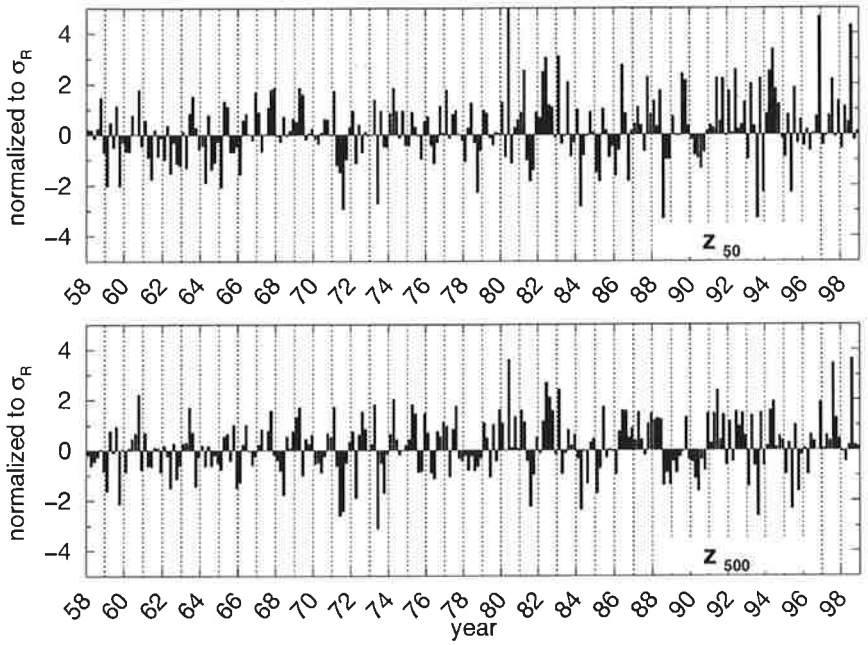

Figure 7.10. Time series of projection coefficients: The non-detrended anomaly fields of cold-season months were projected onto singular patterns of the second SVD mode of the respective field. (a) 50-hPa geopotential heights, (b) 500-hPa geopotential heights. The time series are standardized to the period 1958/59–1977/78.

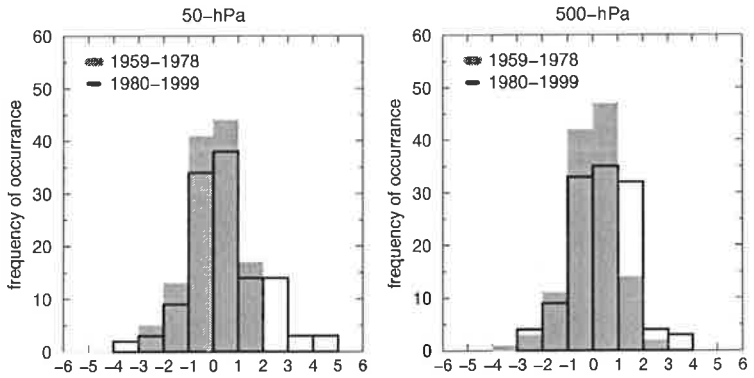

Figure 7.11. Histogram of the projection coefficients, shown in Figure 7.10. The PDF of the periods 1958/59 – 1977/78 and 1979/80 – 1998/99 are compared. (a) 50-hPa geopotential heights, (b) 500-hPa geopotential heights.

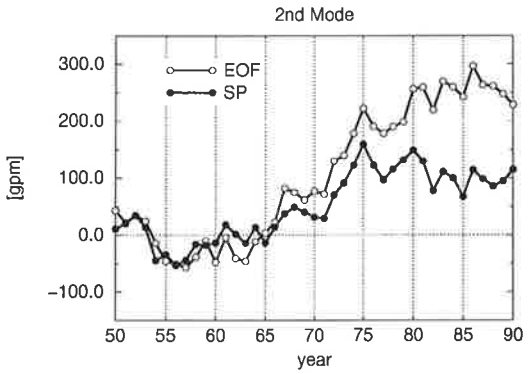

Figure 7.12. Time series of the 10-year running averages of projection coefficients. The non-detrended anomalies of the 500-hPa geopotential heights of cold-season months are projected onto the 2nd EOF (open circles) and 2nd SP (filled circles) of the 500-hPa geopotential height. The time series were centered on the period 1950–1960 of the SP time series.

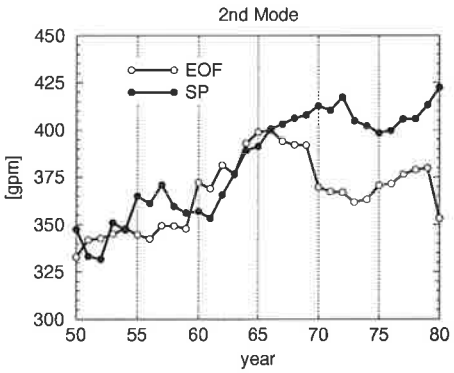

Figure 7.13. Time series of the 20-year running standard deviations of the projection coefficients. The non-detrended anomalies of the 500-hPa geopotential heights of cold-season months are projected onto the 2nd EOF (open circles) and 2nd SP (filled circles) of the 500-hPa height field. The time series were centered to the period 1950–1970.

7.5 Discussion and Conclusions

In the present chapter, we have introduced an approach for studying the spatial structures of both variability and interdecadal changes of the atmospheric circulation of the NH. We isolated the coupled variability modes of the troposphere/stratosphere circulation system by applying SVD analysis to the time series of 50- and 500-hPa geopotential heights of cold-season months. SVD analysis has no user-specific parameters and can therefore be used for the comparison of coupled variability modes between observational data and climate models.

Corresponding to our earlier study (Perlwitz and Graf, 1995), two coupled variability modes could be isolated. These coupled modes reflect relevant features of the dynamical interaction between tropospheric and stratospheric circulation on the monthly mean time scale, that were isolated with the SWAN approach on the basis of daily data. The coupled mode explaining the largest fraction of covariance (1st SVD mode) describes the influence of the strength of the polar cyclonic vortex in the stratosphere on the tropospheric circulation over the North Atlantic/Eurasia. This mode is well known from earlier studies and was isolated on different time scales and by various statistical methods (Baldwin et al., 1994; Perlwitz and Graf, 1995; Kodera et al., 1996). The coupled mode with the highest temporal correlations between the associated patterns (2nd SVD mode) results from the vertical propagation of quasi-stationary tropospheric disturbances into the stratosphere, where waves of ZWN 1 and 2 are exaggerated. This mode has a different spatial structure than the respective coupled mode of our previous study (Perlwitz and Graf, 1995). The reason is that in the latter study CCA in the phase space of the leading EOFs was applied and the influence of variations of waves of the ZWN 2 (EOFs 4 and 5) was not included.

Because the isolated first two coupled variability modes of the 50- and 500-hPa geopotential heights in the NH reflect the dynamical interaction of tropospheric and stratospheric circulation, we conclude that these two coupled modes represent the two most important FCVMs of the troposphere/stratosphere circulation system during the cold season. Therefore, the change in the PDF of these modes represents changes in the atmospheric circulation by physical reasons. In the future, they should be studied together with FCVMs describing processes of air-sea interactions and non-linear regimes of the atmospheric circulation.

By studying the change in the PDF of the coupled variability modes, not only known features have been reviewed including more recent data, but new aspects have also been introduced. This study and our findings (Perlwitz et al., 1997) reveal that the number of cold-season months, characterized by an anomalously strong stratospheric polar winter vortex has increased while the number of months with a weak polar vortex has decreased. Here, we have shown that the tropospheric pattern of the leading coupled mode manifests this change better than

the leading EOF. We detected a significant interdecadal change in the second coupled mode. The variance of the index time series of these mode has been increased both in the troposphere and in the stratosphere. Our results have also revealed that the changes in the PDF of the two coupled modes are stronger in the lower stratosphere than in the troposphere. This corresponds to our conclusion in Chapter 4 where we emphasized that circulation changes in the atmosphere can be detected earlier in the stratosphere than in the troposphere because of the filtering effect of the stratospheric flow to tropospheric disturbances.

The possibility that this change is an artefact in the NCEP reanalyses is small because this change was also determined on the basis of another independent dataset. Various physical explanations for this change can be supposed. One reason might be that the amplitude of tropospheric waves may have increased by air-sea interaction. Another possibility is that the strengthening of the stratospheric polar winter vortex and the increase of the variance of the second coupled variability mode have to be treated together since both phenomena exhibit the same physical process: The observed strengthening of the stratospheric polar winter vortex was related to the change in the transmission-reflection properties for vertically propagating Rossby waves and, thus, to an increase in the downward control of the tropospheric circulation. Therefore, the wave energy is more often trapped in the troposphere and equivalent-barotropic effects become more important. These equivalent-barotropic effects are represented by the second coupled mode. A higher variability in this modes is an indication for a higher importance of these effects.

The validity of the first possibility can be investigated by studying the changes in the PDF of the FCVMs in integrations using atmospheric GCMs forced by observed SST and ice distribution. In the following chapter, we will focus on the second possibility and present the results of the study of variability modes in periods characterized by a preferred exaggeration of either an anomalously strong or weak polar winter vortex.

Chapter 8

The leading variability mode of the coupled troposphere-stratosphere winter circulation in different climate regimes[1]

8.1 Introduction

The leading mode of variability of of winter mean troposphere-stratosphere circulation desribes the relationship between the strength of the stratospheric polar winter vortex and the circulation over North Atlantic/Eurasia Baldwin et al. (1994). The main goal of this chapter is to discuss the features of this leading coupled mode, as they appear on the interannual timescale, in two different climate regimes. The two regimes differ in the mean strength of the stratospheric polar vortex. A preferred excitation of a strong polar vortex by external forcing or internal variability of the coupled atmosphere-ocean climate system over several years may lead to a preferred trapping of planetary wave energy in the troposphere. This may change the structure of the leading coupled variability mode of atmospheric circulation determined with linear statistical methods. The observed records of tropospheric and stratospheric circulation (about 42 years) are too short for the investigation of variability modes in a strong polar vortex state. For the determination of coupled modes with multivariate statistical methods, a higher number of realizations is needed to gain reliable analysis results. Therefore we used the 1900-year control integration carried out with the coupled atmosphere-ocean general circulation model (AOGCM) ECHAM3-LSG, although

[1]The results of this Chapter are published in Perlwitz et al. (2000).

its stratosphere is only marginally represented. Feser et al. (2000) showed that secular variability of the strength of the stratospheric polar-night vortex can be found in this integration. The knowledge about the spatial structures of the leading coupled mode in a strong polar vortex regime will be used for the understanding of features of both the coupled variability under increased anthropogenic greenhouse gas (GHG) forcing and the structure of climate change response of the atmospheric circulation itself. For this study we used a climate change experiment, carried out with the same AOGCM.

The plan of this chapter is as follows: Section 8.2 describes the used data and analysis method. Aspects of the structure and coupling between the troposphere and stratosphere in the control integration are discussed in section 8.3. The leading coupled atmospheric modes in the model's strong and weak polar vortex regimes are shown in section 8.4. In section 8.5 we discuss the exaggeration of the leading coupled mode by increased GHG concentration and the features of the coupled mode under increased anthropogenic forcing. The discussion and conclusions are given in section 8.6.

8.2 Data and Applied Analysis Method

We studied a long-term control integration of 1900 years and a GHG experiment forced with observed CO_2 concentrations from 1880 to 1985 and concentrations according to the Intergovernmental Panel on Climate Change (IPCC) scenario A (business as usual) (Houghton et al., 1990) from 1986 to 2084. Both the control run and the experiment were carried out with the AOGCM ECHAM3-LSG. The atmospheric circulation model ECHAM3, a global low-order spectral model, is a version of the European Center operational weather forecast model with physical parameterizations modified for climate modeling purposes (Roeckner et al., 1992). The model was run with a triangular truncation at wave number 21 (T21), corresponding to a horizontal resolution of about 5.6°, and with 19 vertical levels between the Earth's surface and 10 hPa. The ocean model used was the large scale geostrophic model (LSG) based on primitive equations (Maier-Reimer et al., 1993). The coupled model and the first 500 years of the control run were described by Voss et al. (1998). Timmermann et al. (1998) studied a coupled atmosphere-ocean mode, inherent in this model integration. The AOGCM ECHAM3-LSG has been used for climate change studies, sensitivity experiments, and detection studies (Hasselmann et al., 1995; Cubasch et al., 1997; Hegerl et al., 1997). The ECHAM3 model, coupled with a chemical module CHEM (Steil et al., 1998), was used by (Dameris et al., 1998) to estimate the future development of the ozone layer superposed on an increased GHG forcing.

We applied SVD analysis between the NH (north of 20°N) 50- and 500-hPa geopo-

tential heights on the basis of winter means (December to ebruary). The time series at the grid points were weighted with the square root of the cosine of the geographical latitude. Thus our analysis agrees with the approach of Baldwin et al. (1994). They determined the leading coupled mode on the basis of winter mean observations using SVD analysis. We show homogeneous and heterogeneous regression and correlation patterns as described by Bretherton et al. (1992) and Cheng and Dunkerton (1995). The maps of regression coefficients shown correspond to one standard deviation (σ) of the temporal expansion coefficients of the SVD singular patterns.

We used NCEP reanalysis data for the comparison between model and observational patterns. The similarity of the patterns is given by pattern correlation coefficients. The associated patterns of the leading coupled mode of 50- and 500-hPa geopotential heights, determined on the basis of winter means, are found in Appendix B.2.

8.3 Stratospheric Features of the Leading Coupled Mode in the ECHAM3-LSG Model

The leading coupled variability mode between the time series of NH 50- and 500-hPa geopotential heights in the 1900-year integration of the ECHAM3-LSG model captured the main relationship found in observational data (Baldwin et al., 1994, e.g.). The coupled variability mode describes the connection between the strength of the stratospheric polar vortex and a tropospheric circulation pattern characterized by a hemispheric pressure seesaw between high and middle latitudes, whereas the closest relationship can be found over the North Atlantic region. The fraction of explained total squared covariance of the first (leading) mode is less in the model (60%) than in observational data (76%) determined on the basis of observed 42 winter means. Nevertheless, the model's leading mode is well separated from the second mode, explaining 22% of total squared covariance. The correlation between the expansion coefficients of the singular patterns (not shown) is 0.66.

There are some notable differences between observations and the climate model in the spatial structure of this mode. In this section we want to focus on the stratospheric part of the coupled circulation mode. Figure 8.1 shows the 50-hPa geopotential height field regressed onto the time series of the expansion coefficients of the 50-hPa singular pattern. The variability center of the stratospheric polar vortex is displaced toward the Pacific in the model, whereas it is stronger over the North Atlantic in observational data. The interannual variability of the model's stratospheric polar-night vortex, as depicted in this coupled mode, is remarkably less than in observations (Figure B.3b in Appendix B.2). Over the

North Pole the variability corresponding to one standard deviation of the index time series of the stratospheric field is, with approximately 120 geopotential meters (gpm), only almost half as large as observed (210 gpm). One reason is an overly strong polar-night vortex, which is a common bias in most climate models with an upper boundary set already at 10 hPa. This reduces the possibility of disturbances of the stratospheric circulation by tropospheric planetary waves (Boville and Cheng, 1988) and therefore the variability in the strength of the stratospheric polar vortex. As a result, at the 50-hPa pressure level, the long-term winter mean temperature at the North Pole amounts to −78°C, which is 9 K colder than observed (−69°C), and the long-time mean west wind at 60°N is 9 m/s stronger than observed. Another cause for the reduced variability of the strength of the stratospheric polar vortex in the model results from the absence of external forcing (e.g., volcanic eruptions and solar activity) and of the quasi-biennial oscillation (QBO) in the tropical stratosphere. The phase of the QBO, through modulation of the zonal mean zonal wind, affects the upward and equatorward propagation of ultralong planetary waves Dunkerton and Baldwin (1991).

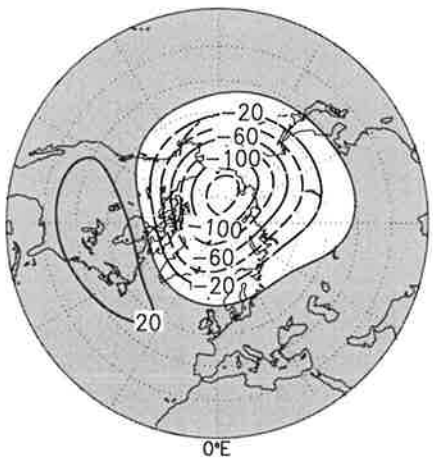

Figure 8.1. Winter mean Northern Hemisphere (NH) 50-hPa geopotential heights regressed onto temporal expansion coefficients of the 50-hPa singular pattern of the leading atmospheric circulation mode, determined from singular value decomposition (SVD) analysis between the time series of the 50- and 500-hPa geopotential height field. Contour interval is 20 geopotential meters (gpm). Positive values are shaded.

We studied the differences in the meridional and vertical propagation of stationary waves between the two states of the leading coupled mode (anomalously weak and strong polar vortex) in the control integration of the climate model. As a diagnostic tool, the Eliassen-Palm flux (E-P flux) (Section 2.2.1 on page 23) is used, which indicates the wave activity and energy propagation. We selected the composites of the E-P flux for the two states on the basis of temporal expansion

coefficients of the 50-hPa pattern of the leading mode. From the 1899 individual winter means, 305 years were characterized by an anomalously strong polar vortex ($\sigma > 1$). The composite for an anomalously weak stratospheric vortex ($\sigma < -1$) is calculated from 289 years.

The meridional cross section of the difference vector of the E-P flux composites (not shown) exhibits the known features of energy flux when the influence of the strength of stratospheric polar vortex is studied (Boville, 1984; Kodera and Koide, 1997). When the polar vortex is anomalously strong, the vertical propagation of stationary wave energy in the stratosphere and the northward flux within the troposphere are significantly reduced, indicating an anomalously strong trapping of stationary wave energy in the troposphere. We also determined composites of the E-P flux for the individual stationary zonal waves by expanding the geopotential height fields in their zonal Fourier harmonics. The contribution of the individual waves to the total E-P flux is additive and depends on the square of the amplitude and the latitudinal and vertical derivatives of the phase of the individual waves (Equation 2.48 on page 26). Figure 8.2 shows the meridional cross section of the difference vectors (strong minus weak polar vortex) for the zonal wave numbers (ZWNs) 1 and 2. When the polar vortex is anomalously strong, the vertical propagation of wave energy of ZWN 1 in the stratosphere is reduced between 60° and 85°N but increased between 40° and 50°N, and an increased southward propagation in the midtroposphere can be found. Thus planetary wave energy of ZWN 1 is more effectively trapped in the troposphere at high latitudes in the strong polar vortex state than in the weak one. At midlatitudes (between 40° and 60°N), a more effective trapping of stationary wave energy of ZWN 2 in a strong polar vortex state dominates. A reduced vertical propagation of ZWN 2 into the stratosphere and a reduced northward propagation in the midtroposphere can be found. As a consequence of the reduced propagation of wave energy into the stratosphere by waves of ZWN 1 and 2, the North Pole temperature at the 50-hPa level is significantly lower (−81°C) than in the weak polar vortex case (−76°C). The discussed results are significant at least at the 95% level.

8.4 The Leading Coupled Mode in the Strong and Weak Polar Vortex Regime

8.4.1 The Definition of the Strong and Weak Polar Vortex Regime

The preferred exaggeration of a strong polar-night vortex in a particular analysis period may change the structure of linear variability modes in the atmospheric

circulation because the waves are trapped more effectively in the troposphere. We used the studied long-term integration of AOGCM ECHAM3-LSG to compare the leading coupled mode on the interannual timescale in a strong and weak polar vortex state. Feser et al. (2000) studied the interannual variability of winter mean NH zonal mean zonal wind in the long-term integration of the ECHAM3-LSG model and found considerable variations on the secular timescale. Following the linear theory, the vertical propagation of planetary waves into the stratosphere depends on a critical velocity which decreases with an increasing zonal wave number (Charney and Drazin, 1961). Thus linear changes in the strength of the stratospheric polar vortex can be connected with nonlinear effects in tropospheric circulation because a critical velocity for a specific wave is involved. We took into consideration this threshold problem for the selection of periods which are characterized by a preferred exaggeration of a strong or weak polar vortex in the control run. We counted how often the expansion coefficient of the singular pattern of the 50-hPa field is larger (smaller) than σ ($-\sigma$) during a 30-year period, where σ is the long-term standard deviation of the temporal expansion coefficients. In the following, $N_{>\sigma}$ and $N_{<-\sigma}$ stand for the number of positive and negative enhancements, respectively. In section 8.3 we have shown that the characteristics of vertical propagation for waves of ZWN 1 and 2 are different between both states. We used the ratio $rat_{30} = N_{>\sigma}/N_{<-\sigma}$ as a measure which indicates the preference of the positive enhancement ($rat_{30} > 1$, anomalously strong polar vortex) or the negative enhancement ($0 < rat_{30} < 1$, anomalously weak polar vortex) of the regression pattern (Figure 8.1) within the studied 30-year period. To avoid $N_{<-\sigma}$ becoming zero, both $N_{<-\sigma}$ and $N_{<\sigma}$ were set equal to 1 before counting. Figure 8.3 shows the time series of this ratio at the 50-hPa level, determined for overlapping 30-year periods. This smoothed time series does not emphasize single extreme anomalies as does a 30-year running average.

The visual inspection of this time series shows a pronounced secular variability, characterized by periods in which an anomalously strong vortex is more often excited than an anomalously weak one or vice versa. The respective periods which clearly differ in the preference of a strong and weak stratospheric vortex are called strong and weak polar vortex regimes (PVR).

8.4.2 The Leading Coupled Mode in the Strong and Weak PVR

To study the interannual coupled variability between tropospheric and stratospheric winter circulation in the climate model within the two PVRs, we selected periods permanently characterized by a ratio rat_{30} larger (smaller) than one standard deviation [$\sigma_{lg(rat_{30})} = 0.23$]. The composed time series for the strong (weak) PVR consist of a total of 174 (194) years. We applied the SVD analysis between

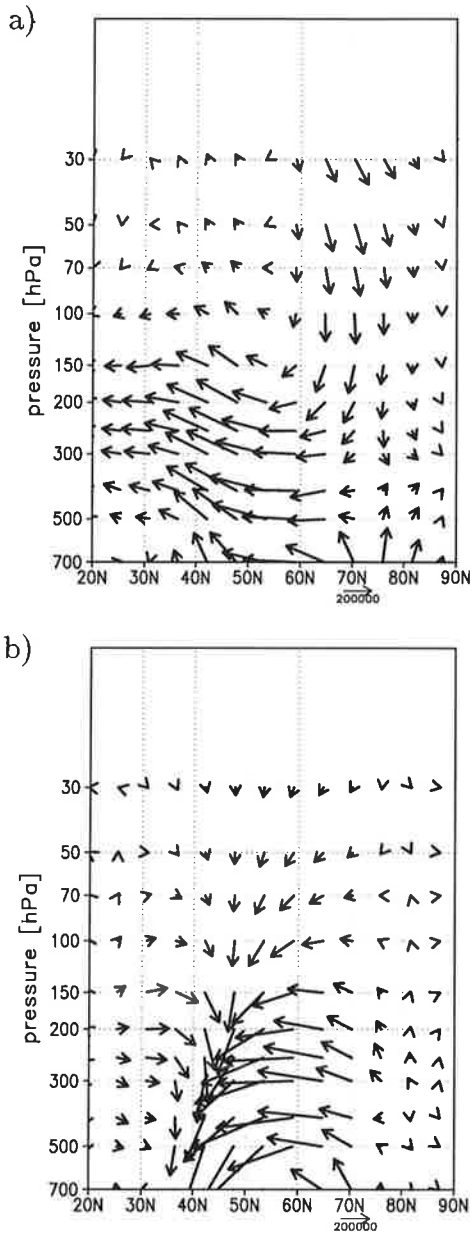

Figure 8.2. Meridional cross section of difference vectors between the composites of the Eliassen-Palm (E-P) flux (strong minus weak polar vortex state) for (a) zonal wave number (ZWN) 1 and (b) ZWN 2. The arrow scale amounts to $2.0 \times 10^5\,\mathrm{kg\,s^{-1}}$. The vertical scaling factor c is 125.

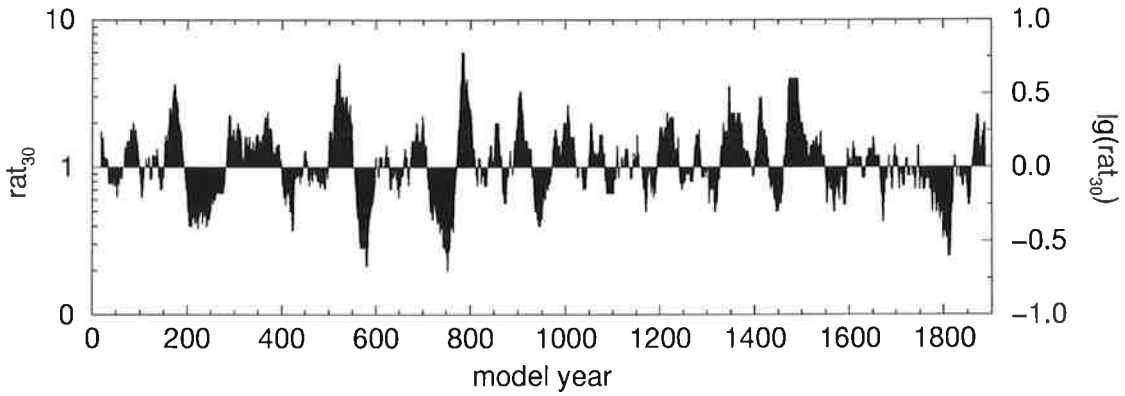

Figure 8.3. Time series of the ratio of numbers of positive to negative enhancement of the strength of the stratospheric polar vortex for overlapping 30-year periods as described in text.

the 50- and 500-hPa geopotential height fields for the composed data set of the strong and weak PVR, separately. As expected, the total covariance between the NH 50- and 500-hPa geopotential fields is higher in the weak than in the strong PVR. The extra covariance in the weak PVR is mainly concentrated in the first SVD mode, explaining 61% of total squared covariance, whereas the fraction amounts to 52% in the strong PVR.

Figure 8.4 compares the associated (heterogeneous) regression patterns of the strong and weak PVR. The shading represents the heterogeneous correlation patterns. The light and dark shadings indicate "remarkable" absolute correlation coefficients larger than 0.3 and 0.5, respectively (a correlation coefficient of 0.2 is already significant at the 95% level). The pattern correlation between the regression patterns of the observations (Figure B.3c) and a model regime indicate that the weak PVR of the model better matches the observed mode than the model's strong PVR. The agreement of the 500-hPa patterns between observations and the weak (strong) PVR further increases (decreases) when the spatial structures north of 35°N (instead of 20°N) are compared. The 50-hPa pattern of the weak PVR (Figure 8.4a) clearly shows a pronounced circumpolar pressure seesaw, whereas the corresponding pattern of the strong PVR (Figure 8.4b) depicts a more zonally asymmetric structure. This becomes clear from Table 8.1, which contains the zonal mean geostrophic wind and the amplitudes of both ZWNs 1 and 2 at 58°N of the 50- and 500-hPa regression patterns shown in Figure 8.4. This latitude is representative for the latitude belt between 50° and 70°N. In comparison with the weak PVR, the meridional gradient of the regression pattern of the 50-hPa field in the strong PVR, and thus the zonal mean geostrophic wind, is reduced, whereas the amplitude of the waves of both ZWN 1 and 2 is visibly increased. Table 8.1 also indicates that the difference in the heterogeneous regression patterns of the 500-hPa geopotential heights between both

Table 8.1. Zonal Mean Zonal Component of the Geostrophic Wind (u_g) and Amplitude (A_k) of Waves of Zonal Wave Numbers (ZWNs) $k = 1$ and $k = 2$ for the Heterogeneous Regression Patterns of 50- and 500-hPa Geopotential Heights at 58°N

	50 hPa		500 hPa	
	weak PVR	strong PVR	weak PVR	strong PVR
u_g [m/s]	2.1	1.2	1.0	0.8
A_1 [gpm]	24 (96%)	34 (66%)	9 (89%)	8 (30%)
A_2 [gpm]	3 (1%)	24 (32%)	1 (1%)	11 (58%)

regimes mainly results from a higher amplitude of the ZWN 2 component in mid-latitudes in the strong PVR. At the same time, the variability of waves of ZWN 1 is reduced in the pattern of the strong PVR between 35° and 45°N. At 42°N the reduction amounts to about 4 gpm. As a result of these differences in the zonal wave structure of the coupled variability patterns, the node line between positive and negative anomalies over both the North Atlantic and the North Pacific is shifted southward in the strong PVR relative to the weak one. Over the North Atlantic this shift is quite small (about 5°), but over the North Pacific it amounts to about 20°.

During winter, owing to advective processes, circulation anomalies are closely related to lower tropospheric temperature anomalies. The 850-hPa temperatures regressed onto temporal expansion coefficients of the 50-hPa singular pattern are given in Figure 8.5. Again, the regression pattern of the weak PVR better matches the observations (Koide and Kodera, 1999; Perlwitz and Graf, 1995) than the pattern of the strong PVR, which exhibits a pronounced cold-ocean-warm-land variation between 50° and 80°N.

Comparing the regression patterns of the 500-hPa field between the model's weak PVR (Figure 8.4c) and observations (Figure B.3c), a difference in the positions of the positive and negative centers of the 500-hPa pressure anomalies over the North Atlantic can be found. In observations, an anomalously strong vortex is connected with a stronger than normal southwesterly wind over the eastern North Atlantic, causing an intensified advection of mild and wet maritime air to northwest Europe (Figure B.4, Koide and Kodera, 1999; Perlwitz and Graf, 1995). In the model's weak PVR the North Atlantic centers of action, as depicted in the tropospheric regression pattern of the leading coupled mode, are arranged meridionally, and their node line is mainly zonally directed. Therefore, in connection with this coupled circulation mode in the climate model, this advective influence of the circulation on the temperature of northwest Europe is underestimated.

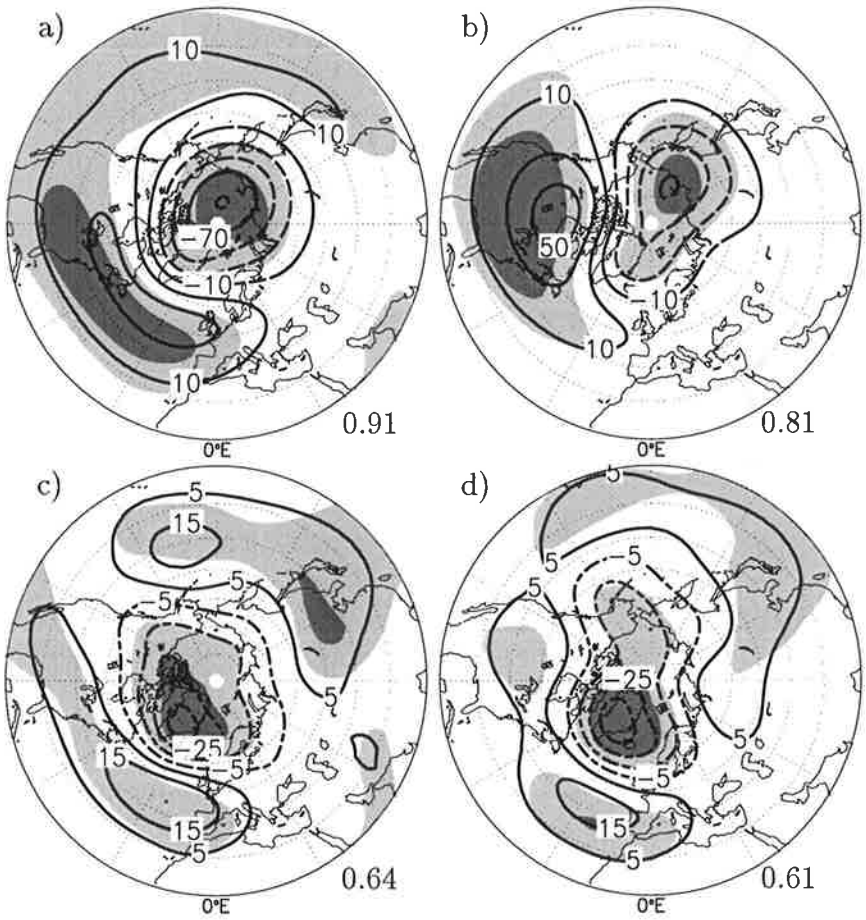

Figure 8.4. Regression patterns of SVD analysis between the time series of 50- and 500-hPa geopotential heights for the weak and strong polar vortex regimes (PVRs): (a) 50 hPa, weak PVR, (b) 50 hPa, strong PVR, (c) 500 hPa, weak PVR, and (d) 500 hPa, strong PVR. The contour intervals are 20 gpm (50-hPa maps) and 10 gpm (500-hPa maps). The light (dark) shading indicates that the absolute correlation coefficients between the time series of the expansion coefficients and of the local geopotential heights exceeds 0.3 (0.5). The numbers in the bottom right corner of each panel indicate the pattern correlation coefficients between the regression patterns of the model and observations.

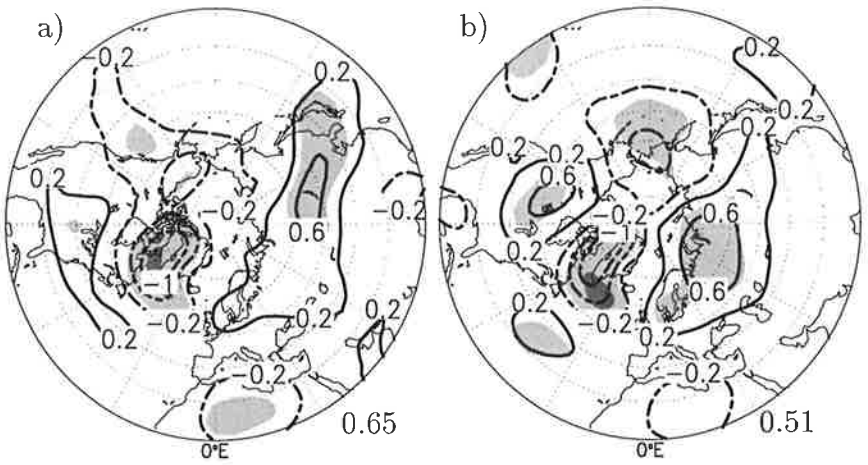

Figure 8.5. The 850-hPa temperature regressed on the temporal expansion coefficient of the 50-hPa singular pattern for the (a) weak and (b) strong PVR. The contour interval is 0.4 K. The light (dark) shading indicates that the absolute correlation coefficients between the time series of the expansion coefficients and of the local temperature exceeds 0.3 (0.5).

A still-to-strong polar vortex in the weak PVR, and a relatively low spatial resolution (T21) smoothing the orography in the model, may explain the structural differences between the observed and the modeled tropospheric pattern. However, we found a visible reduction in the structural bias of the leading atmospheric circulation mode in the weak PVR in comparison with the total model integration, although the reduction of the cold bias in the high-latitude 50-hPa temperature amounts to only 1 K.

8.4.3 Causes of the Structural Differences Between the Coupled Modes of Both Regimes

We studied in more detail whether the strong differences in the leading atmospheric variability mode can be mainly attributed to the preferred enhancement of an anomalously strong polar-night vortex. From the results of the SVD analyses, it cannot be concluded that the circulation in the strong PVR is characterized by a higher variability of midlatitude waves of ZWN 2. We compared the standard deviation of the amplitude of this stationary wave, determined from the geopotential height fields, between both PVRs and did not find any significant differences. Another possibility is that in the strong PVR the variability of waves of ZWN 2 is more stationary than in the weak PVR. This would be an indication of the stronger effect of the tropospheric trapping of wave energy in the

strong PVR, which is connected with an increase of equivalent-barotropic effects (Boville and Cheng, 1988). To study the spatial variability structure of the individual zonal waves, EOF analysis was used. We selected a specific latitude and expanded the individual realizations of the geopotential height fields in their zonal Fourier harmonics. Let z_k be anomalous geopotential height fields related to the kth zonal wave component at a specific latitude. Then z_k at the longitude λ of the year t is expressed as follows:

$$z_k(\lambda, t) = a(t)\cos(k\lambda) + b(t)\sin(k\lambda).$$

If the longitudinal structure of the year-to-year variation is geographically fixed, the time series $a(t)$ and $b(t)$ are not independent. One EOF can, then, explain the total variability of the latitudinal field z_k. Contrary to this, when this variation is randomly distributed, the correlation between $a(t)$ and $b(t)$ becomes zero and the total variance is equally shaded by two EOFs (50% each). Therefore the fraction of variance explained by the leading EOF can be used as a measure of the stationarity of the variation of the wave of ZWN k at a specific latitude.

We performed this analysis for the waves of both ZWN 1 and 2, at each latitude of the NH (north of 20°N) grid and each available pressure level between 1000 and 30 hPa. The explained fractions of total variance of the leading EOF, obtained from the individual analyses, are combined as a meridional cross section. Figures 8.6a and 8.6c show these meridional cross sections of ZWN 1 and 2, respectively, for the weak PVR. The meridional cross section of the difference of this parameter between the strong and weak PVR (strong minus weak) is given in Figures 8.6b (ZWN 1) and 8.6d (ZWN 2). In the weak PVR a strong stationarity of waves of ZWN 1 can be found in the troposphere around 25°N and between 40° and 50°N. At midlatitudes more than 75% of total variance is explained by the leading EOF from the surface to the 150-hPa level. In the strong PVR the tropospheric centers of stationarity are shifted southward and are slightly increased. In the weak PVR the two tropospheric centers of high stationarity for ZWN 2 can be found around 30°N and between 55° and 65°N. In the strong PVR the degree of stationarity is more than 10% higher in both centers. For the midlatitude center the difference increases with increasing altitude, and the leading EOF of ZWN 2 explains more than 70% of total variance from the surface to the 50-hPa level. At these latitudes the highest amplitude of the leading EOF can be found. We also determined the phase of the first EOF of ZWN 2, for example, the longitude where the first extremum (minimum or maximum) of the wave is found. At midlatitudes, where the maximum change in the degree of stationarity occurs in the upper troposphere and lower stratosphere, we found an eastward shift of phase in the strong PVR relative to the weak one. For instance, at 58°N and the 500-hPa level the phase amounts to 63°E and 72°E for the weak and strong PVR, respectively. The eastward phase shift decreases with increasing height.

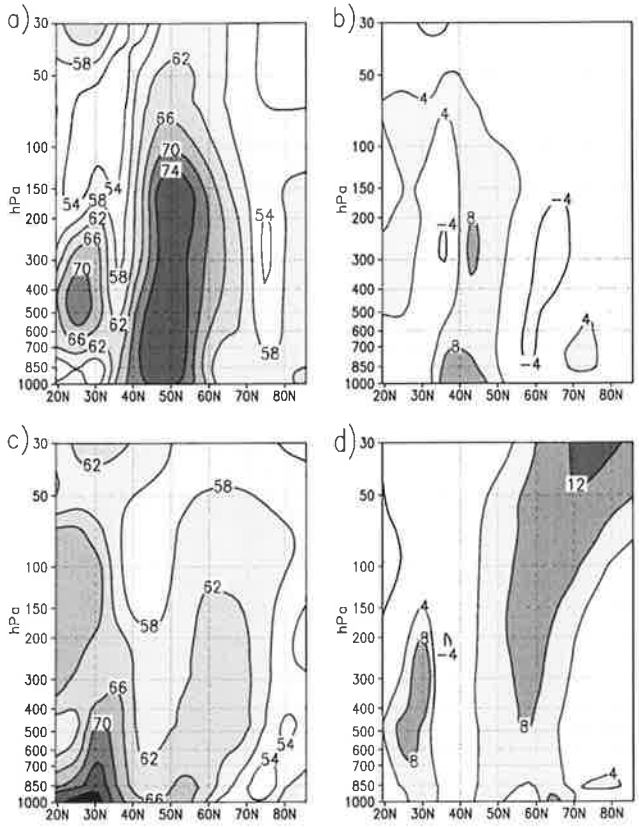

Figure 8.6. Meridional cross section of the explained fraction of total variance of the leading empirical orthogonal function (percent) as described in text. Shown are (a) weak PVR, ZWN 1; (b) strong minus weak PVR, ZWN 1; (c) weak PVR, ZWN 2; and (d) strong minus weak PVR, ZWN 2.

This shift amounts to 5° and 2° at the 200-hPa and 50-hPa level, respectively. At higher altitudes the increase of stationarity of the variability of ZWN 2 is more important.

As expected in a strong PVR, the dynamical coupling between the troposphere and stratosphere is considerably reduced. We have shown that this is related to a change in the spatial structure of the leading coupled variability mode of tropospheric and stratospheric circulation in the studied climate model. In the strong PVR the more effective tropospheric trapping of stationary wave energy of ZWN 2 at midlatitudes changes the zonal variability structure of this stationary wave in the troposphere as well as in the stratosphere. In the next section we want to give an application of the knowledge about the spatial structure of the associated patterns in a strong PVR.

8.5 The Exaggeration of the Leading Coupled Mode by the Increased Greenhouse Effect

Palmer (1993) suggested that the impact of enhanced atmospheric CO_2 concentration manifests itself as an increase in certain preferred patterns of internal variability of the atmosphere rather than in some new pattern of atmospheric variability which is orthogonal to the internal modes. Orthogonality of the response pattern is the main prerequisite for the application of optimal fingerprint analysis (Hasselmann, 1993). There is a physical process which can explain the exaggeration of the leading coupled variability mode by increasing GHG forcing via changes in the stratospheric circulation (Perlwitz and Graf, 1995). The increase in tropospheric temperature and humidity in lower latitudes due to the combined greenhouse effect leads to a lifting of the lower-latitude geopotential height layers and thus to an initial intensification of the polar-night vortex by the strengthening of the thermal wind. The climate change sensitivity experiments of Shindell et al. (1999b) and Graf et al. (1995) show a strengthening of the stratospheric polar vortex with rising anthropogenic forcing. An intensified polar vortex is related to changed transmission-refraction properties of vertically propagating tropospheric waves and may produce tropospheric circulation anomalies similar to the positive phase of the leading coupled circulation mode.

Therefore we studied the exaggeration of the coupled mode of atmospheric winter circulation due to anthropogenic GHG forcing in an experiment, carried out with the ECHAM3-LSG model. The GHG forcing is based on observations (1880-1985) and the IPCC (1990) scenario A (business as usual, 1986-2084) (Houghton et al., 1990). The yearly winter (December-January-February) response patterns were calculated as difference patterns between the individual winter means of the GHG experiment and the long-term winter mean of the control run. The global average was removed from the individual winter mean geopotential height fields of the scenario simulation before determining the difference patterns. This allows one to neglect the global mean increase in the geopotential height caused by the thermal expansion of the atmosphere due to increasing temperature. We projected these difference patterns of 50- and 500-hPa geopotential heights onto the respective singular patterns, isolated by SVD analysis of the total unforced model run. The time series of the projections, normalized by the standard deviation of the respective control run, σ_C, are shown in Figure 8.7. After 1980 a preferred enhancement of the positive phase of the main coupled circulation mode, both in the stratosphere and in the troposphere, can be seen. The interannual variability, as it is depicted in this coupled mode, decreases with the increase of the GHG concentration. Extremes only occur in the positive phase of this mode.

The time series for 50-hPa geopotential heights (Figure 8.7a) reveals that in the studied GHG forcing experiment, the stratospheric polar vortex strengthens con-

tinuously with increasing GHG concentration. This changes the condition for the vertical propagation of tropospheric planetary waves. Thus a reduction of dynamical interaction between tropospheric and stratospheric circulation under stronger GHG forcing may be connected with a transition to a new dynamic regime similar to the strong PVR which was isolated in the control run. To isolate the leading coupled variability mode of stratospheric and tropospheric circulation under stronger GHG forcing, we performed a SVD analysis between winter mean NH 50- and 500-hPa geopotential heights using the last 70 years of the GHG simulation (2014-2084). The long-term local trends were removed before applying the SVD approach. As expected, the associated patterns capture very well the features of the corresponding patterns of the strong PVR. We found that the concurrent variation of the meridional pressure seesaw over the North Atlantic and North Pacific of NH 500-hPa circulation (Figure 8.8) is more pronounced than in the model's strong PVR (Figure 8.4d). Both high-latitude centers of action over the ocean show about the same value of the regression coefficient (25 gpm), whereas the meridional pressure seesaw in the strong PVR is clearly stronger over the North Atlantic than over the North Pacific. In the studied climate change experiment the strength of the seesaw over the North Atlantic is visibly reduced under increased anthropogenic forcing. Relative to the regression map of the strong PVR of the control run, the map of the GHG experiment shows a southward shift of the node line between positive and negative anomalies over both oceans. Additionally, an eastward shift of the centers of action over the North Atlantic is found. The latter result corresponds partly to the study of Ulbrich and Christoph (1999). They investigated the shift of the centers of action of the NAO with increasing GHG forcing in the AOGCM ECHAM3/OPYC (T42), using sea level pressure, and found a northeastward shift.

We were also interested in the consequences of a polar vortex intensified by increased GHG concentration for the structure of the response in atmospheric circulation. With the associated patterns of the leading coupled mode in the different PVRs, a basis for such an analysis is given. We studied the similarity between the climate change response in tropospheric and stratospheric circulation and the associated patterns of the coupled troposphere-stratosphere circulation in the weak and strong PVR. We determined spatial pattern correlations between the patterns of the model response of NH 50- and 500-hPa geopotential heights with the singular patterns of the coupled modes for both the strong and weak PVR. This correlation coefficient can vary between -1.0 and 1.0 and clearly stresses the structural pattern similarity and not the anomalies. The time series of pattern correlation determined for overlapping decadal mean (11-year) response patterns are given in Figure 8.9. The overlapping decadal averages reduce the spatial and temporal noise associated with higher-frequency variability. After 1990, there is, in general, a higher similarity between the response patterns and the associated patterns of the model's strong PVR than of the weak one. For the strong PVR the pattern correlations of the 50-hPa level fluctuate between 0.6 and 0.7, while

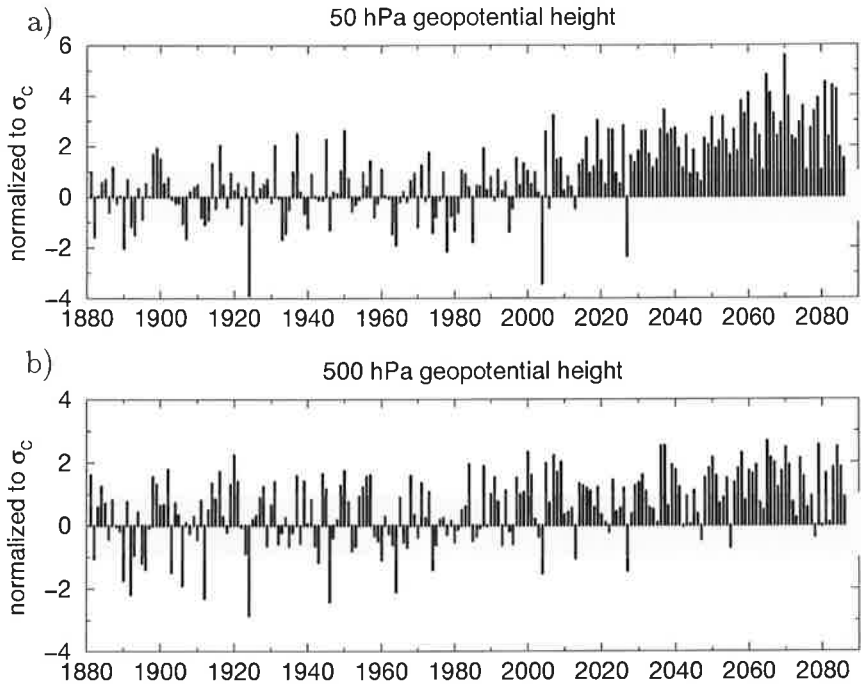

Figure 8.7. Time series of projections of response pattern, determined from a transient greenhouse gas (GHG) forcing experiment, onto the singular patterns of leading atmospheric circulation mode, determined from the 1900-year control run. The time series for (a) 50-hPa geopotential height field (north of 20°N) and (b) 500-hPa geopotential height field (north of 20°N) are nomalized by the standard deviation σ_C of the individual projections of the control run.

the spatial pattern correlations of the 500-hPa level are higher and can reach values greater than 0.8, explaining about 70% of the 11-year smoothed spatial response structure.

We also studied the similarity between the response of the 850-hPa temperature and the regression patterns shown in Figure 8.5. The temporal course (Figure 8.9c) follows mainly the time series of spatial pattern correlation of the 500-hPa geopotential height field. The mean pattern correlation coefficients after 1990 amount to about 0.6 for the pattern of the strong PVR, indicating that 36% of the hemispheric response can be explained.

We have shown that the strength of the stratospheric polar vortex is a control parameter for the structure of the climate change response in tropospheric temperature and circulation in the studied climate change experiment. The spatial pattern correlation remains smaller than 1.0 because other processes, the air-sea interaction, for example, are also very important for the development of the climate change response (Timmermann et al., 1998, 1999).

Figure 8.8. The 500-hPa heterogeneous regression patterns of SVD analysis between 50- and 500-hPa geopotential heights for the GHG experiment on the basis of the time period 2014–2084 of the simulation. The shading corresponds to Figure 8.4.

8.6 Discussion and Conclusions

We studied the leading coupled mode between the time series of NH 50- and 500-hPa geopotential heights for two climate regimes of a 1900-year control run, carried out with the AOGCM ECHAM3-LSG (T21). The two regimes differ on the interdecadal timescale in the strength of the stratospheric polar vortex and therefore in the transmission-refraction properties of vertically propagating tropospheric waves. We found that this difference has consequences for the spatial structures of the coupled mode between both regimes, which were determined with a linear statistical analysis method. The spatial structures of the leading coupled variability mode of observational data better match the corresponding patterns of the model's weak PVR than those of the strong one's. In the model's strong PVR the concurrent variation of waves of ZWN 2 in the troposphere and stratosphere is increased, whereas the interaction of tropospheric waves with the mean stratospheric flow is reduced. Because of the more effective tropospheric trapping of stationary wave energy of ZWN 2 at midlatitudes, the zonal variability structure of this wave on the interannual timescale is considerably influenced by barotropic effects in the troposphere as well as in the stratosphere. For the studied integration with the AOGCM ECHAM3-LSG, we could show that the phase in which the North Atlantic and the North Pacific varies concurrently on the interannual timescale is influenced by the strength of the stratospheric polar vortex during the analysis period. During periods with a preferred exaggeration of a strong polar vortex, the inphase variation of both atmospheric regions is emphasized. Our analysis is clearly focused on the investigation of atmospheric circulation modes. On the interannual timescale, the variability of the sea sur-

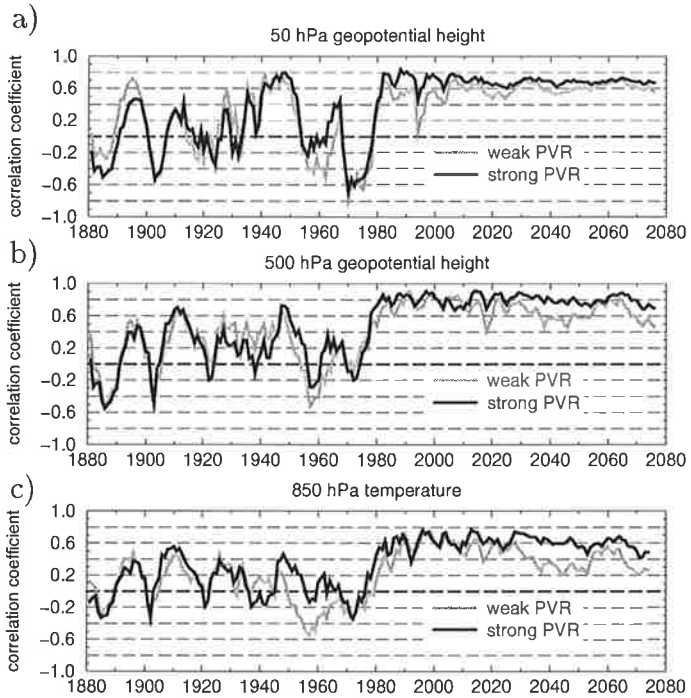

Figure 8.9. Time series of the spatial pattern correlation between the decadal response patterns and the singular patterns of the model's leading coupled circulation mode for both the model's weak PVR (solid line) and strong PVR (shaded line). Shown are (a) 50-hPa geopotential height field (north of 20°N), (b) 500-hPa geopotential height field (north of 20°N), and (c) 850-hPa temperature (north of 20°N). The corresponding reference patterns of the 850-hPa temperature are given in Figure 8.5.

face temperature is primarily forced by atmospheric variability (e.g., Delworth, 1996). For the explanation of atmospheric variability on multiyear to multidecadal timescales, however, the interaction of the atmosphere with the ocean becomes important (e.g. Rodwell et al., 1999). With this paper we wanted to show that besides the ocean, the strength of the stratospheric polar vortex is also an important parameter for the understanding of both variability modes of the atmosphere-ocean system of a climate model (e.g. Timmermann et al., 1998) and features of observed climate variability. Further studies are required to determine whether a changed tropospheric anomaly structure, resulting from changes in the strength of the stratospheric polar vortex in individual years, contributes to the amplification and stabilization of longer timescale modes of the atmosphere-ocean system.

The leading coupled variability mode of the troposphere-stratosphere circulation as well as the response of winter circulation were studied in a climate change experiment with increasing GHG concentration carried out with the same model.

In this experiment a large part of the climate change signal is carried by the leading coupled mode. This result confirms the idea of Palmer (1993) that the impact of enhanced atmospheric GHG concentration manifests itself mainly as an increase in certain preferred patterns of internal variability of the atmosphere. We clearly focused on the winter season and isolated physically filtered patterns representing the related variation of stratospheric and tropospheric circulation on the interannual timescale. We could show, however, that the spatial structure of the climate change patterns alters with increased forcing. One parameter for this change is the intensification of the stratospheric polar vortex with increasing greenhouse effect. This intensification leads not only to an exaggeration of the positive phase of the leading coupled variability mode but also to a change in the structure of this mode. Under increased GHG forcing, both the response and the coupled variability between tropospheric and stratospheric circulation itself have a high similarity to the leading coupled mode of the model's strong PVR. The changed structure of the leading coupled mode can be interpreted as the orthogonal signal evolving from external forcing that is studied in optimal fingerprint analysis (Hasselmann, 1993).

There are increasing efforts to attribute the cold-season climate change, which has been observed during the last 40 years, to the increased GHG effect. Our results emphasize two important points which have to be considered when comparing observed climate changes with the cold-season GHG response of sensitivity experiments with comprehensive climate models.

First, the strength of the stratospheric polar vortex of a climate model used for the study of climate changes during winter is one crucial parameter that determines the spatial structure of the climate response and the strength of the signal. This conclusion agrees with the results of Shindell et al. (1999b). They found considerable differences in the change of the AO index, depending on the representation of the stratosphere in their climate model, which were forced with increasing GHG concentration.

Second, the representation of the variability of the planetary waves in the climate model influences the spatial structure of the winter responses in circulation and temperature. One reason is the intensification of the stratospheric polar vortex with rising GHG concentration, which leads to a change of the structure of planetary waves that are trapped in the troposphere when the polar vortex is intensified. The predominant change in the zonal structure of the variability of waves of ZWN 2 may be partly attributed to the relatively coarse horizontal resolution (5.6°). Other important factors may be the vertical resolution and, as explained in the previous point, the top height of the model.

Thus an evaluation of climate models used for sensitivity experiments should include the investigation of the coupled variability modes of troposphere-stratosphere circulation. It is of the greatest importance that climate models properly

represent the energy and structure of the leading atmospheric variability mode because this mode can be exaggerated by stratospheric aerosols from tropical volcanic eruptions (Graf et al., 1993; Kodera, 1994), reduced ozone concentration at the end of the winter (Graf et al., 1998), solar activity (Shindell et al., 1999a)], and, as demonstrated by (Shindell et al., 1999b), Graf et al. (1995), and this study, the increasing anthropogenic greenhouse effect.

Chapter 9

Summary and Outlook

The main issue of this thesis has been to increase our understanding of the mechanisms by which the stratosphere can affect the tropospheric climate. The dynamical coupling of tropospheric and stratospheric circulation in the Northern Hemisphere (NH) was investigated by applying the new approach *Single Wave Analysis* (SWAN) which combines a well-known theoretical concept of the coupling mechanism with the statistical analysis of observational datasets. The isolated features were used to interpret both the coupled modes of variability in tropospheric and stratospheric geopotential height fields and the changes in the estimated probability density function (PDF) of these modes.

9.1 Characteristic Features of the Dynamical Coupling in Observations

The new SWAN approach is based on the Charney-Drazin Theorem and implies the investigation of the relationship between geopotential height fields at tropospheric and stratospheric pressure levels for single wave fields. These single wave fields of geopotential heights can be determined by deriving Fourier harmonics. The 10-day lowpass filtered time series of the 50- and 500-hPa geopotential heights from the reanalyses of the National Centers for Environmental Prediction (NCEP) were used. The data were studied for the cold-season months November to April since the processes underlying the Charney-Drazin Theorem are most prominent during these months. Canonical Correlation Analysis (CCA) was applied as lag-correlation technique to detect the direction of the relationship between tropospheric and stratospheric wave fields.

Four mechanisms describing the dynamical coupling between troposphere and

stratosphere were investigated. They can be summarized as follows:

1. Modes of tropospheric circulation exaggerating waves of zonal wave number (ZWN) 1 and 2 in the lower stratosphere

The upward propagation of quasi-stationary disturbances is most relevant near 60°N. Waves of ZWN 1 in the lower stratosphere are mainly exaggerated by a wave train-like pattern covering the North Pacific and North America. In contrast, quasi-stationary waves of ZWN 2 remain nearly intact when propagating into the stratosphere. A faster propagation time in the upward direction occurs for waves of ZWN 2 (2 days) than for waves of ZWN 1 (4-5 days). The relationship between the tropospheric and stratospheric disturbances is closer for waves of ZWN 2 ($r = 0.71$) than for ZWN 1 (r=0.59). The latter two features agree very well with the propagation characteristics of zonal waves at 51°N as derived by Randel (1987).

2. Downward propagation of spherical wave-like anomalies

A key-mechanism for understanding the downward control by stratospheric circulation was identified by isolating the characteristic patterns in the 50- and 500-hPa geopotential height fields, which describe the down- and equatorward propagation of the wave energy of ZWN 1. This feature was weak only when all cold-season months were studied. However, it could be clearly detected by studying the vertical propagation of wave anomalies during winter seasons (December to February), which are characterized by an anomalously strong polar winter vortex (S-PVS[1]). Thus, a downward control is only possible during this state of the stratospheric circulation. In contrast, when the state of the stratospheric circulation is characterized by an anomalously weak polar winter vortex (W-PVS[2]), the energy generated in the troposphere propagates unhindered into the stratosphere. This finding fundamentally supports the Charney-Drazin Theorem concerning the existence of Rossby critical velocities for single zonal waves.

3. Relationship between the strength of the stratospheric polar winter vortex and single tropospheric waves

It was found that variations in the strength of the stratospheric circulation significantly influence the structure of the mid-tropospheric waves of ZWN 1 to ZWN 3, whereas the zonal mean zonal wind (ZWN 0) in the troposphere is not directly changed. Thus, the forecast potential of the strength of the stratospheric polar winter vortex for changes in the mid-tropospheric circulation does not result from the change in the zonal mean zonal wind, but from the modification of the structure of tropospheric waves:

[1]S-PVS: strong-polar-vortex season
[2]W-PVS: weak-polar-vortex season

- Variations in the strength of the stratospheric polar winter vortex significantly affect the tropospheric waves of ZWN 2 at high latitudes and waves of ZWN 3 at mid-latitudes. The effect on waves of ZWN 3 is only apparent during the early winter season (November to December). The characteristic propagation time for this 'downward effect' is only a few days.

- Non-linear changes in the transmission-refraction properties for the waves of ZWN 1 are involved, so that linear methods, such as correlation analysis, applied to all cold-season months, failed to isolate an influence of the strength of the polar winter vortex on this tropospheric wave. The non-linear aspects were reduced by studying the linear relationship between both parameters separately for the composites of the S-PVS and W-PVS. A significant influence on the mid-latitude structure of the waves of ZWN 1 at the 500-hPa level was isolated in the two composites. However, the characteristic time for the 'downward effect' is longer during the W-PVS (about 23 days) than during the S-PVS (3 days) and the phase of the tropospheric waves differs between the composites.

4. Relationship between the strength of the stratospheric polar winter vortex and the North Atlantic Oscillation (NAO)

The combined signal of the recomposed field from waves of ZWN 0 to 3 for 10-day averages reveals that the circulation over east Asia and, more prominently, over the North Atlantic, which is similar to the NAO, is significantly affected by variations in the strength of the stratospheric polar winter vortex. By studying the relationship between the NAO and the strength of the stratospheric polar winter vortex in the S-PVS and W-PVS individually, it was found that a forecast potential for the phase of the NAO exists only when changes in the stratospheric flow modify the transmission-refraction properties for waves of ZWN 1. This confirms our previous results (Perlwitz and Graf, 1995) from studying the coherent variation in the tropospheric and stratospheric circulation on the basis of monthly mean values. The results of this study contradict the interpretations of Baldwin and Dunkerton (1999) who assumed that the strength of the polar winter vortex modifies the tropospheric circulation on a hemispheric scale similar to the pattern of the Arctic Oscillation.

9.2 Coupled Modes of Variability and Interdecadal Climate Change

The circulation of the NH during the cold season has changed significantly during recent decades. The results of this thesis give three arguments for why coupled

modes of variability of the stratospheric and tropospheric circulation can be used in describing climate changes during the cold season:

1. The stratosphere has a strong filtering effect on tropospheric disturbances.

This argument follows from the Charney-Drazin Theorem. Observational indications are that:

- The horizontal circulation of the stratosphere has a considerably smaller number of spatial degrees of freedom than the tropospheric circulation.
- The first three EOFs of the 50-hPa geopotential height field are well separated from higher modes, whereas for the 500-hPa geopotential height field, this is only true for the first mode.
- Variations in the stratosphere exhibit two preferred states: an anomalously strong and an anomalously weak polar winter vortex.

Therefore, the spatially filtered climate change pattern may be detectable earlier in the stratosphere than in the troposphere because of the larger signal to noise ratio for the stratospheric circulation. This pattern, however, may have a different spatial structure in the troposphere than in the stratosphere.

2. The coupled modes represent the physical processes.

SVD analysis was applied to the NH 50- and 500-hPa geopotential heights of the cold-season winter months. The first two coupled modes of the 50- and 500-hPa geopotential heights reflect relevant features of the dynamical interaction between tropospheric and stratospheric circulation on the monthly mean time scale. These features could be isolated using the SWAN approach on the basis of daily data. The coupled mode explaining the largest fraction of covariance (1st SVD mode) describes the influence of the strength of the polar winter vortex in the stratosphere on the tropospheric circulation over the North Atlantic/Eurasia. This mode is well known from earlier studies and was isolated on different time scales and by various statistical methods (Baldwin et al., 1994; Perlwitz and Graf, 1995; Kodera et al., 1996). The coupled mode with the highest temporal correlations between the associated patterns (2nd SVD mode) results from the vertical propagation of quasi-stationary tropospheric disturbances into the stratosphere, where waves of ZWN 1 and 2 are exaggerated. This mode has a different spatial structure in comparison to the respective coupled mode of our previous study (Perlwitz and Graf, 1995) in which CCA in the phase space of the leading EOFs were applied. The CCA results, however, depend on the number of EOFs used for the stratospheric fields. By using only the first three EOFs as in Perlwitz and Graf (1995), the vertical propagation of wave-like disturbances in ZWN 2 was not considered.

3. The coupled modes are insensitive to inhomogeneities in the NCEP reanalyses.

The growing database considered in the reanalysis process has led to inhomogeneities in the NCEP reanalyses. It was shown that these inhomogeneities do not affect the results from the statistical analyses regarding the coupled modes of variability which represent the physical process of the dynamical coupling between both atmospheric layers.

The two coupled modes represent the important fundamental modes of climate variability of the troposphere/stratosphere circulation system. In contrast to EOFs derived in mid-tropospheric geopotential height fields, the characteristic patterns of the coupled modes reflect physical processes. Therefore, analyzing the PDF of these modes can increase our understanding of the mechanisms which are most relevant to the atmospheric circulation changes. By comparing the estimated PDFs of these two modes between the 20-year periods 1959–1978 and 1980–1999 the following characteristics were found:

- The number of cold-season months characterized by an anomalously strong stratospheric polar winter vortex has increased.
- The tropospheric pattern of the leading coupled mode manifests the observed climate change better than the leading EOF.
- The second coupled mode shows a significant increase in the variance of its index time series.
- Changes in the PDF of the coupled modes are more pronounced for the index time series of the stratospheric field than for the index time series of the tropospheric field.

The findings described in the first item confirm our previous studies (Graf et al., 1995; Perlwitz and Graf, 1995; Perlwitz et al., 1997) by including more recent data.

In this thesis it has been proposed that the strengthening of the stratospheric polar winter vortex and the increase in the variance of the second coupled variability mode have to be treated together since both phenomena exhibit the same physical process. The observed strengthening of the stratospheric polar winter vortex is related to the change in the transmission-refraction properties for vertically propagating Rossby waves and, thus, to an increase in the downward control of the tropospheric circulation. Therefore, the wave energy is more often trapped in the troposphere and equivalent-barotropic effects become more important. These equivalent-barotropic effects are represented by the second coupled mode.

This proposed mechanism has been confirmed by studying the coupled modes of variability on the interannual time scale in climate regimes characterized by

a preferred exaggeration of either an anomalously weak or strong polar winter vortex over 30 years or longer in a control run with the coupled atmosphere-ocean model ECHAM3-LSG. A sensitivity experiment forced with increasing greenhouse gas concentration exhibits a continuous increase in the stratospheric polar winter vortex as well as a transition to a strong polar vortex regime (PVR).

9.3 Conclusions

The prominent result of this thesis is that winter seasons characterized either by an anomalously strong or weak polar winter vortex exhibit different tropospheric circulation regimes. Only in the case of a strong stratospheric polar winter vortex does a downward control of the tropospheric circulation by reflection of waves of ZWN 1 occur. This downward influence on the structure of tropospheric waves is considerably less than the influence of tropospheric disturbances on the structure of stratospheric waves of ZWN 1 and 2. This result confirms our understanding of the coupling of stratosphere and troposphere: Waves in the stratosphere originate in the troposphere, whereas the disturbances in the tropospheric circulation result mainly from internal processes. However, the findings also reveal that the two circulation regimes, characterized either by an preferred exaggeration of an anomalously strong or weak polar winter vortex, exhibit different tropospheric variability structures and are of high relevance to interannual and interdecadal climate variability.

The results lead to the following implications for the detection of cold-season climate change in the NH:

- Changes observed during the last decades can only be understood by taking into account the interaction between tropospheric and stratospheric circulation.

- The strengthening of the polar winter vortex by natural and anthropogenic forcing may lead to strong non-linear effects in the tropospheric climate when the critical velocity for the vertical propagation of waves of ZWN 1 is exceeded.

- The detection of the climate change may fail with optimal fingerprint analysis because this method is based on a linear approach.

- A forecast of the anthropogenic climate change signal using climate models will fail, if the climate model is characterized by a polar cold bias, i.e., the control climate in the models is already similar to a strong PVR.

9.4 Future Plans

These results encourage to examine the dynamical processes in the strong and weak PVRs in more detail using atmospheric general circulation models (GCMs). The prerequisite for such a study is that the model used should reproduce the observed features of the dynamical coupling between troposphere and stratosphere. The following two projects are planned for the near future:

1. Process-oriented validation of atmospheric GCMs

So far, the validation of atmospheric circulation models has always concentrated on the investigation of the first two statistical moments (mean and variance) of important atmospheric parameters of the climate system. However, it must also be confirmed that correct values for the first two moments result from the appropriate physical processes. Therefore, a validation of the atmospheric circulation models should also include the evaluation of their capability to reproduce important physical processes. Atmospheric GCMs will be validated by the relevant features which characterize the dynamical coupling between troposphere and stratosphere determined from observational data.

2. Investigation of the ocean-troposphere-stratosphere (OTS) interaction

The decadal to multidecadal variability in the winter NAO over the past half century is associated with the North Atlantic SST (Rodwell et al., 1999; Latif et al., 2000). The air-sea interaction only partially explains the circulation changes observed (Rodwell et al., 1999). Using observational data, Bjerknes (1964) provided compelling evidence that interannual fluctuations in SST are largely governed by wind-induced changes in latent and sensible heat fluxes at the sea surface. Our study implies that the dynamical coupling between tropospheric and stratospheric circulation in winter influences the behavior of the planetary waves on the hemispheric scale and involves the NAO. Because of the short memory of the atmosphere, the interdecadal climate variations cannot be sufficiently explained by only studying the coupled troposphere/stratosphere system. A full understanding of the feedback processes involved in mid-latitude OTS interaction is still lacking. The relevant factors that control the space-time climate variability in the NH will be isolated, with and without external forcing, by studying the three component system OTS. Such factors may include stratospheric circulation regimes, the relevance of ocean dynamics, and the role of baroclinic eddies in the coupling.

Appendix A

Elements of Linear Analysis

A.1 Eigenvalues and Eigenvectors [1]

Let $\mathbf{A}$ a $n \times p$ matrix of rank $r = min(p, n)$:

$$\mathbf{A} = \begin{pmatrix} a_{11} & a_{12} & \dots & a_{1p} \\ a_{21} & a_{22} & \dots & a_{2p} \\ \vdots & \vdots & & \vdots \\ a_{n1} & a_{n2} & \dots & a_{np} \end{pmatrix}$$

$\mathbf{A}'$ indicates the transpose of the matrix $\mathbf{A}$.

DEFINITION: The *eigenvalues* of a square (i.e., p=n) matrix $\mathbf{A}$ are defines as the roots of the determinantal equation

$$h(\lambda) = |\mathbf{A} - \lambda\mathbf{I}| = 0, \tag{A.1}$$

' where $\mathbf{I}$ is the identity matrix. The p roots of $h(\lambda)$ are denoted by $\lambda_1, \lambda_2, \dots, \lambda_p$. Since

$$|\mathbf{A} - \lambda_i\mathbf{I}| = 0 \qquad \text{for each} \qquad i = 1, \dots, p, \tag{A.2}$$

it follows that $\mathbf{A} - \lambda_i\mathbf{I}$ is singular and hence there exists a nonzero vector γ satisfying

$$\mathbf{A}\gamma = \lambda_i\gamma. \tag{A.3}$$

[1] The description mainly follows Dillon and Goldstein (1984)

Any vector γ satisfying equation A.3 is called an associated *eigenvector* of $\mathbf{A}$ for the eigenvalue λ_i.

In general, the eigenvalues of a matrix $\mathbf{A}$ need not be real numbers; they may be complex. However, if $\mathbf{A}$ is symmetric (i.e. $a_{ij} = a_{ji}$ for all i and j), then all the eigenvalues of $\mathbf{A}$ will be real.

When $\mathbf{A}$ is symmetric, eigenvectors corresponding to distinct eigenvalues are *orthogonal.*

Any symmetric matrix $\mathbf{A}$ can be written as

$$\mathbf{A} = \mathbf{P}\Lambda\mathbf{P}', \tag{A.4}$$

where Λ is a diagonal matrix of eigenvalues of $\mathbf{A}$, and $\mathbf{P}$ is an orthogonal matrix, whose columns are the standardized eigenvectors associated with the diagonal entries of Λ.

A.2 Singular Value Decomposition Theorem

If $\mathbf{A}$ is an $n \times p$ matrix of rank r, than $\mathbf{A}$ can be written as

$$\mathbf{A} = \mathbf{P}\Sigma\mathbf{Q}', \tag{A.5}$$

where $\mathbf{P}$ $(n \times r)$ and $\mathbf{Q}$ $(p \times r)$ are column orthonormal matrices and Σ is a diagonal matrix with positive elements. An orthonormal matrix is defined as a matrix $\mathbf{P}$ for which $\mathbf{P}'\mathbf{P} = \mathbf{I}$, but $\mathbf{P}'\mathbf{P} \neq \mathbf{I}$. That is, each column vector has unit length and is orthogonal to every other column vector. The σ_i can be shown to be the square roots of the nonzero eigenvalues of the square matrix $\mathbf{A}\mathbf{A}'$ and the r column vectors of $\mathbf{Q}'$ are the eigenvectors of $\mathbf{A}'\mathbf{A}$. The diagonal elements are called singular elements and the column vectors are singular vectors.

Appendix B

Leading Coupled Modes of Variability

B.1 Coupled Modes for Cold-Season Months

B.1.1 1st SVD Mode

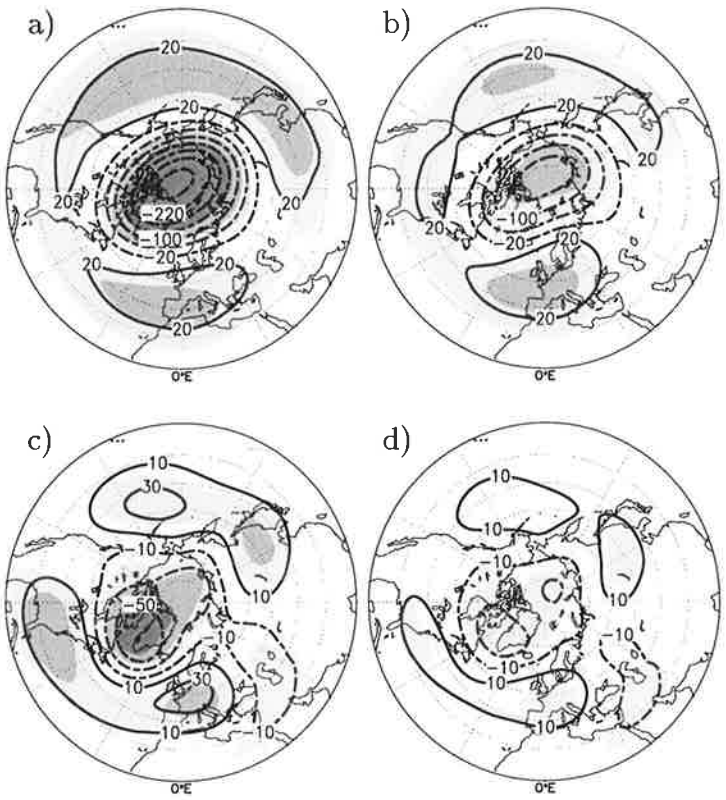

Figure B.1. Maps of regression coefficients (isolines, [gpm]) and correlation coefficients (shading) for the first SVD mode of 50- and 500-hPa geopotential heights, determined for cold-season months November to April. a) homogeneous maps for 50-hPa heights, b) heterogeneous maps for 50-hPa heights, c) homogeneous maps for 500-hPa heights, and d) heterogeneous maps for 500-hPa heights. Light, medium and dark shading indicates that the absolute correlation coefficients between the time series exceeds 0.3, 0.5 and 0.7.

B.1.2 2nd SVD Mode

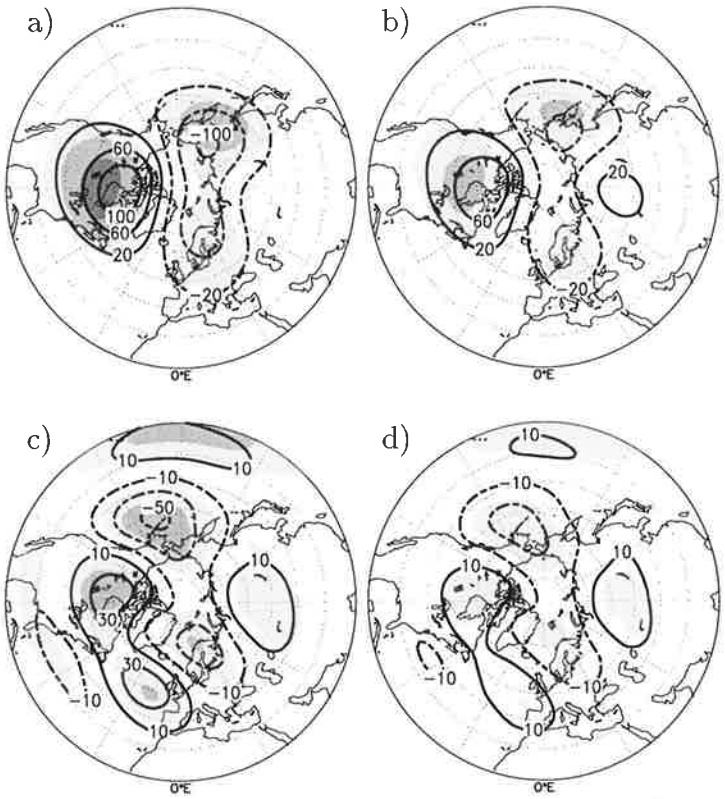

Figure B.2. Maps of regression coefficients (isolines, [gpm]) and correlation coefficients (shading) for the second SVD mode of 50- and 500-hPa geopotential heights, determined for cold-season months November to April. a) homogeneous maps for 50-hPa heights, b) heterogeneous maps for 50-hPa heights, c) homogeneous maps for 500-hPa heights, and d) heterogeneous maps for 500-hPa heights. Light, medium and dark shading indicates that the absolute correlation coefficients between the time series exceeds 0.3, 0.5 and 0.7.

B.2 The Leading Coupled Mode for Winter Means

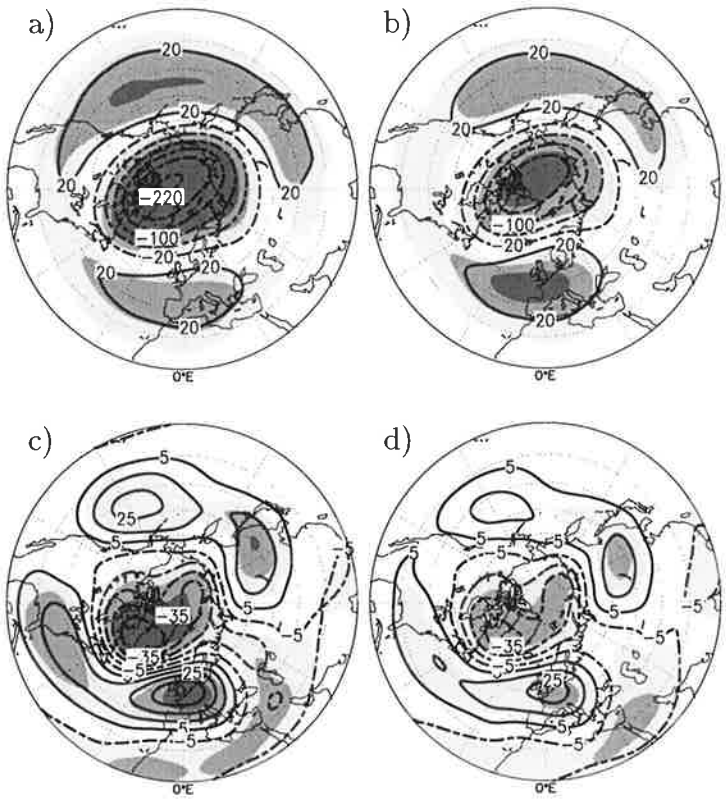

Figure B.3. Maps of regression coefficients (isolines, [gpm]) and correlation coefficients (shading) for the first SVD mode of 50- and 500-hPa geopotential heights, determined for winter means. a) homogeneous maps for 50-hPa heights, b) heterogeneous maps for 50-hPa heights, c) homogeneous maps for 500-hPa heights, and d) heterogeneous maps for 500-hPa heights. Light, medium and dark shading indicates that the absolute correlation coefficients between the time series exceeds 0.3, 0.5 and 0.7.

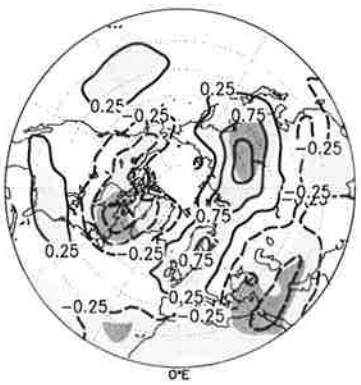

Figure B.4. The 850-hPa temperature [K] regressed onto the temporal expansion coefficients of the 50-hPa singular pattern, determined by SVD analysis of the 50- and 500-hPa geopotential heights for winter means. Light, medium and dark shading indicates that the absolute correlation coefficients between the time series exceeds 0.3, 0.5 and 0.7.

Appendix C

Nomenclature

Abreviations

AO	Arctic Oscillation
AOGCM	atmosphere-ocean general circulation model
CCA	canonical correlation analysis
COWL	cold ocean warm land
E-P flux	Eliassen-Palm flux
EOF	empirical orthogonal function
FCVM	fundamental climate variability mode
GHG	greenhouse gas concentration
IGY	International Geophysical Year
NAO	North Atlantic Oscillation
NCEP	National Centers for Environmental Prediction
NH	Northern Hemisphere
NMC	National Center of Meteorology of the United States
PC	Principle Component
PCA	Principal Composite Analysis
PDF	probability density function
PVR	polar vortex regime
QBO	quasi-biennial oscillation
S-PVS	strong polar-vortex-season
SH	Southern Hemisphere
SP	singular pattern
SPARC	Stratospheric Processes And their Role in Climate
SST	sea surface temperature
SVD	Singular Value Decomposition
SWAN	Single Wave Analysis
W-PVS	weak polar-vortex-season
ZWN	zonal wave number

Bibliography

Anderson, T. W., *An Introduction to Multivariate Statistical Analysis*, Wiley & Sons, 675 pp., 2nd edn., 1984.

Andrews, D. G., and M. E. McIntyre, Planetary waves in horizontal and vertical shear: The generalized Eliassen-Palm relation and the mean zonal accelation, *J. Atmos. Sci.*, *33*, 2031–2048, 1976.

Andrews, D. G., J. Holton, and C. B. Leovy, *Middle Atmosphere Dynamics*, Academic Press, pp 489, 1987.

Angell, J. K., Annual and seasonal global temperature changes in the troposphere and low stratosphere, 1960-85, *Mon. Wea. Rev.*, *114*, 1922–1930, 1986.

Baldwin, M. P., and T. J. Dunkerton, Propagation of the Arctic Oscillation from the stratosphere to the troposphere, *J. Geophys. Res.*, *104*, 30937–30946, 1999.

Baldwin, M. P., and D. O'Sullivan, Stratospheric effects of ENSO-related tropospheric circulation anomalies, *J. Clim.*, *8*, 659–667, 1995.

Baldwin, M. R., X. Cheng, and T. J. Dunkerton, Observed correlations between winter-mean tropospheric and stratospheric circulation anomalies, *Geophys. Res. Lett.*, *21*, 1141–1144, 1994.

Barnett, T. P., and R. Preisendorfer, Origins and levels of monthly and seasonal forecast skill for United States surface air temperatures determined by canonical correlation analysis, *Mon. Wea. Rev.*, *115*, 1825–1850, 1987.

Barnston, A. G., and R. E. Livezey, Classification, seasonality and persistence of low-frequency atmospheric circulation anomalies, *Mon. Wea. Rev.*, *115*, 1083–1126, 1987.

Bates, J. R., Dynamics of stationary ultra-long waves in the middle latitudes, *Q. J. R. Meteorol. Soc.*, *103*, 397–425, 1977.

Bjerknes, J., Atlantic air-sea interaction, *Adv. Geophys.*, *10*, 1–82, 1964.

Blackmon, M. L., and N. C. Lau, Regional characteristics of the Northern Hemisphere wintertime circulation: a comparison of the simulation of a GFDL general circulation model with observations, *J. Atmos. Sci.*, *37*, 497–514, 1980.

Boville, B. A., The influence of the polar night jet on the tropospheric circulation in a GCM, *J. Atmos. Sci.*, *7*, 1132–1142, 1984.

Boville, B. A., and X. Cheng, Upper boundary effect in a general circulation model, *J. Atmos. Sci.*, *45*, 2591–2607, 1988.

Bretherton, C. S., C. Smith, and J. M. Wallace, An intercomparision of methods for finding coupled patterns in climate data, *J. Clim.*, *5*, 541–560, 1992.

Charney, J. G., and P. G. Drazin, Propagation of planetary-scale disturbances from the lower into the upper atmosphere, *J. Geophys. Res.*, *66*, 83–109, 1961.

Cheng, X., and T. Dunkerton, Orthogonal rotation of spatial patterns derived from singular value decomposition analysis, *J. Clim.*, *9*, 2631–2643, 1995.

Cherry, S., Singular value decomposition analysis and canonical correlation analysis, *J. Clim.*, *9*, 2003–2009, 1996.

Corti, S., F. M. F, and T. N. Palmer, Signature of recent climate change in frequencies of natural atmospheric circulation regimes, *Nature*, *398*, 799–802, 1999.

Cubasch, U., R. Voss, , G. C. Hegerl, J. Waszkewitz, and T. Crowley, Simulation of the influence of solar radiation variations on the global climate with an ocean-atmosphere general circulation model., *Clim. Dyn.*, *13*, 757–767, 1997.

Dameris, M., V. Grewe, and B. Steil, Assessment of the future development of the ozone layer, *Geophys. Res. Lett.*, *25*, 3579–3582, 1998.

Delworth, T. L., North Atlantic variability in a coupled ocean-atmosphere model, *J. Clim.*, *9*, 2356–2375, 1996.

Dethloff, K., A. Weisheimer, A. Rinke, D. Handorf, M. V. Kurgansky, W. Jansen, P. Maaš, and P. Hupfer, Climte variability in a nonlinear atmosphere-like dynamical system, *J. Geophys. Res.*, *103*, 25957–25966, 1998.

Dillon, W. R., and M. Goldstein, *Multivariate Analysis*, New York, 1984.

Dole, R. M., and N. D. Gordon, Persistent anomalies of the extratropical Northern Hemisphere wintertime circulation: Geographical distribution and regional persistence characteristics, *Mon. Wea. Rev.*, *111*, 1567–1586, 1983.

Dunkerton, T. J., and M. P. Baldwin, Quasi-biennial modulation of planetary-wave fluxes in the Northern Hemisphere winter, *J. Atmos. Sci.*, *48*, 1043–1061, 1991.

Eliassen, A., and E. Palm, On the transfer of energy in stationay mountain waves, *Geophys. Publ.*, *22*, 1–23, 1961.

Feser, F., H.-F. Graf, and J. Perlwitz, Secular variability of the coupled tropospheric and stratospheric circulation in the GCM ECHAM3/LSG, *J. Theoret. Appl. Meteor.*, *65*, 1–15, 2000.

Fraedrich, K., C. Ziehmann, and F. Sielmann, Estimation of spatial degrees of freedom, *J. Clim.*, *8*, 361–369, 1995.

Fukuoka, A study on 10-day forecast (a synthetic report), *Geophys. Mag*, *22*, 117–208, 1951.

Geller, M. A., and J. C. Alpert, Planetary wave coupling between the troposphere and the middle atmosphere as a possible sun-weather mechanism, *J. Atmos. Sci.*, *37*, 1197–1214, 1980.

Glahn, H. R., Canonical correlation analysis and its relationship to discriminant analysis and multiple regression, *J. Atmos. Sci.*, *25*, 23–31, 1968.

Graf, H.-F., I. Kirchner, A. Robock, and I. Schult, Pinatubo eruption winter climate effects: model versus observations, *Clim. Dyn.*, *9*, 81–93, 1993.

Graf, H.-F., J. Perlwitz, I. Kirchner, and I. Schult, Recent northern winter climate trends, ozone changes and increased greenhouse gas forcing, *Contr. Atm. Phys.*, *68*, 233–248, 1995.

Graf, H.-F., J. Perlwitz, and I. Kirchner, Coupled modes of tropospheric and stratospheric circulation in nature and in models, in *Stratospheric Processes and their Role in Climate (SPARC). Proceedings of the First SPARC General Assembly. Geneva 1996*, vol. I, pp. 129 – 132, WMO/TD-No. 814, 1997.

Graf, H.-F., I. Kirchner, and J. Perlwitz, Changing lower stratospheric circulation: The role of ozone and greenhouse gases, *J. Geophys. Res.*, *103*, 11251–11261, 1998.

Gutzler, D. S., and L. Shukla, Analogs in the wintertime 500-mb height field, *J. Atmos. Sci.*, *41*, 177–189, 1984.

Hartmann, D. L., Some aspects of stratospheric dynamics, *Adv. Geophys*, *28*, 219–247, 1985.

Hasselmann, K., Optimal fingerprints for the detection of time dependent climate change, *J. Clim.*, *6*, 1957–1971, 1993.

Hasselmann, K., L. Bengtsson, U. Cubasch, G. C. Hegerl, H. Rodhe, E. Roeckner, H. v. Storch, R. Voss, and J. Waszkewitz, Detection of anthropogenic climate change using a fingerprint method, in *Proc. Modern Dynamical Meteorology. Symposion in Honor of Aksel Wiin Nicelson*, edited by P. Dittevson, ECMWF press, 1995.

Hegerl, G., K. Hasselmann, U. Cubasch, J. F. Mitchell, E. Roeckner, R. Voss, and J. Waszkewitz, Multi-fingerprint detection and attribution analysis of greenhouse gas, greenhouse gas-plus-aerosol and solar forced climate change, *Clim. Dyn.*, *13*, 613–634, 1997.

Hines, C. O., A possible mechanism for the production of sun-weather correlations, *J. Atmos. Sci.*, *31*, 589–591, 1974.

Horel, J. D., A rotated principal component analysis of the interannual variability of the Northern Hemisphere 500 mb height field, *Mon. Wea. Rev.*, *109*, 2080–2092, 1981.

Hotelling, H., Relations between two sets of variables, *Biometrika*, *28*, 321–377, 1936.

Houghton, J. T., G. J. Jenkins, and J. J. Ephraums, eds., *Climate change: The IPCC scientific assessment.*, Cambridge University Press, Cambridge, 1990.

Hurrell, J. W., Decadal trends in the North Atlantic Oscillation: Regional temperature and precipitation, *Science*, *269*, 676–679, 1995.

James, I. N., *Introduction to Circulation Atmosphere*, Cambridge University Press, 1994.

James, I. N., and P. M. James, Spatial structure of ultra-low-frequency variability of the flow in a simple atmospheric circulation model, *Q. J. R. Meteorol. Soc.*, *118*, 1211–1233, 1992.

Jolliffe, I. T., Rotation of ill-defined principal components, *Appl. Stat.*, *38*, 139–147, 1989.

Kalnay, E., et al., The NCEP/NCAR 40-year reanalysis project, *B. Am. Meteorol. Soc.*, *77*, 437–471, 1996.

Kanamitsu, M., Describtion of the NMC global assimilation and forcast system, *Weather Forecast*, *4*, 334–342, 1989.

Kanamitsu, M., et al., Resent changes implemented into the global forecast system at NMC, *Weather Forecast*, *6*, 425–435, 1991.

Kanzawa, H., Eliassen-Palm flux diagnostics and the effect of the mean wind on planetary wave propagation for an observed sudden stratospheric warming, *J. Meteor. Soc. Japan*, *60*, 1063–1073,, 1982.

Kaurola, J., Some diagnostics of the northern wintertime climate simulated by the ECHAM3 model, *J. Clim.*, *10*, 201–222, 1997.

Kitoh, A., H. Koide, K. Kodera, S. Yukimoto, and A. Noda, Interannual variability in the stratospheric-tropospheric circulation in a coupled ocean-atmosphere GCM,

Geophys. Res. Lett., *23*, 543–546, 1996.

Kodera, K., Influence of the stratospheric circulation change on the troposphere in the Northern Hemisphere winter, in *The role of the stratopshere in global change*, edited by M.-L. Chanin, vol. 18 of *NATO ASI Series*, pp. 227–243, Springer-Verlag, 1993.

Kodera, K., Influence of volcanic eruptions on the troposphere through stratospheric dynamical processes in the Northern Hemisphere, *J. Geophys. Res.*, *99*, 1273–1282, 1994.

Kodera, K., and M. Chiba, Tropospheric circulation changes associated with stratospheric sudden warmings: A case study, *J. Geophys. Res.*, *100*, 11055–11068, 1995.

Kodera, K., and H. Koide, Spatial and seasonal characteristics of recent decadal trends in the northern hemispheric troposphere and stratosphere, *J. Geophys. Res.*, *102*, 19433–19447, 1997.

Kodera, K., K. Yamazaki, M. Chiba, and K. Shibata, Downward propagation of upper stratosphere mean zonal wind perturbation to the troposphere, *Geophys. Res. Lett.*, *17*, 1263–1266, 1990.

Kodera, K., M. Chiba, H. Koide, A. Kitoh, and Y. Nikaidou, Interannual variability of the winter stratosphere and troposphere, *J. Meteor. Soc. Japan*, *74*, 365–382, 1996.

Koide, H., and K. Kodera, A SVD analysis between the winter NH 500-hPa height and surface temperature fields, *J. Meteor. Soc. Japan*, *77*, 47–61, 1999.

Kutzbach, J., Empirical vectors of sea-level pressure, surface temperature and precipitation complexes over North America, *Journal Applied Meteorology*, *6*, 791–802, 1967.

Labitzke, K., and H. v. Loon, The effect on the stratosphere of three tropical volcanic erruptions, in *The Mount Pinatubo Erruption. Effects on the Atmosphere and Climate*, edited by G. Fiocco, D. Fuá, and G. Visconti, vol. 42 of *NATO ASI Series I*, 1996.

Labitzke, K., and H. van Loon, Association between 11-year solar cycle, the QBO and the atmosphere. Part I: The troposphere and stratosphere in the Northern Hemisphere winter, *Atmos. Terr. Phys.*, *50*, 197–206, 1988.

Latif, M., K. Arpe, and E. Roeckner, Oceanic control of decadal north atlantic sea level pressure variability in winter, *Geophys. Res. Lett.*, *27*, 727–730, 2000.

Leder, S., K. Labitzke, and H. van Loon, Comparison between NCEP/NCAR and FUB analysis of the stratosphere, in *Proceedings of the First WCRP International Conference on Reanalysis*, pp. 379–382, WMO/TD-No. 876, 1998.

Lorenz, E. N., Empirical orthogonal functions and statistical weather prediction, 1956, Sci. Rep. No. 1, Statist.Forecasting Proj., Dept. Meorol, MIT, 49 pp.

Maier-Reimer, E., U. Mikolajewicz, and K. Hasselmann, Mean circulation of the Hamburg LSG model and its sensitivity to the thermohaline surface forcing, *J. Phys. Oceanogr.*, *23*, 731–757, 1993.

Matsuno, T., Vertical propagation of stationary planetary waves in the winter Northern Hemisphere, *J. Atmos. Sci.*, *27*, 871–883, 1970.

Molteni, F., S. Tibaldi, and T. N. Palmer, Regimes in the wintertime circulation over northern extratropics. I: Observational evidence, *Q. J. R. Meteorol. Soc.*, *116*, 31–67, 1990.

Newman, M., and P. D. Sardeshmukh, A caveat concerning singular value decomposi-

tion, *J. Clim.*, *8*, 352–360, 1995.

Nicholls, N., The use of canonical correlation to study teleconnections, *Mon. Wea. Rev.*, *115*, 393–398, 1987.

North, G. R., Theory of energy-balance climate models, *J. Atmos. Sci.*, *32*, 2033–2043, 1975.

North, G. R., T. L. Bell, R. F. Cahalan, and F. J. Moeng, Sample errors in the estimation of empirical orthogonal functions, *Mon. Wea. Rev.*, *110*, 699–707, 1982.

Palmer, N. T., A nonlinear dynamical perspective on climate prediction, *J. Clim.*, *12*, 575–591, 1999.

Palmer, T. N., A nonlinear dynamical perspective on climate change, *Weather*, *48*, 314–326, 1993.

Pawson, S., and M. Fiorino, A comparison of reanalyses in the tropical stratosphere. Part 1: thermal structure and the annual cycle, *Clim. Dyn.*, *14*, 631–644, 1998a.

Pawson, S., and M. Fiorino, A comparison of reanalyses in the tropical stratosphere. Part 2: the quasi-biennial oscillation, *Clim. Dyn.*, *14*, 644–658, 1998b.

Pawson, S., and M. Fiorino, A comparison of reanalyses in the tropical stratosphere. Part 3: Inclusion of the pre-satellite data era, *Clim. Dyn.*, *15*, 241–250, 1999.

Pawson, S., K. Labitzke, , R. Lenschow, B. Naujokat, B. Rajewski, M. Wiesner, and R.-C. Wohlfahrt, Climatology of the Northern Hemisphere stratosphere derived from Berlin analysis. Part 1: Monthly means, Tech. Rep. Band 7, Heft 3, Met. Abh. der FU Berlin, 1993.

Pearson, K., On lines and planes of closest fit to systems of points in space, *Phil. Mag.*, *2*, 559–572, 1902.

Peixoto, J. P., and A. H. Oort, *Physics of Climate*, American Institute of Physics, 1992, pp. 520.

Perlwitz, J., and H.-F. Graf, The statistical connection between tropospheric and stratospheric circulation of the Northern Hemisphere in winter, *J. Clim.*, *8*, 2281–2295, 1995.

Perlwitz, J., H.-F. Graf, and I. Kirchner, Increasing greenhouse gases and ozone trends, in *Stratospheric Processes and their Role in Climate (SPARC). Proceedings of the First SPARC General Assembly. Geneva 1996*, vol. II, pp. 461 – 464, WMO/TD-No. 814, 1997.

Perlwitz, J., H.-F. Graf, and R. Voss, The leading mode of the coupled troposphere-stratosphere winter circulation in different climate regimes, *J. Geophys. Res.*, *105*, 6915–6926, 2000.

Ramaswamy, V., M. D. Schwarzkopf, and W. J. Randel, Fingerprint of ozone depletion in the spatial and temporal pattern of recent lower-stratosphere cooling, *Nature*, *382*, 616–618, 1996.

Randel, W. J., Study of planetary waves in the southern winter troposphere and stratosphere. Part 1: Wave structure and vertical propagation, *J. Atmos. Sci.*, *44*, 917–935, 1987.

Randel, W. J., Further modification of time-longitude lag-correlation diagrams: Application to three-dimensional wave propagation, *Tellus*, *40A*, 257–271, 1988.

Richman, M. B., Rotation of prinicple components, *J. Climatol.*, *6*, 293–335, 1986.

Robock, A., and J. Mao, Winter warming from large volcanic eruptions, *Geophys. Res.*

Lett., *19*, 2405–2408, 1992.

Rodwell, M. J., D. P. Rowell, and C. K. Folland, Oceanic forcing of the wintertime North Atlantic Oscillation and European climate, *Nature*, *398*, 320–323, 1999.

Roeckner, E., et al., Simulation of the present-day climate with the ECHAM model: Impact of model physics and resolution, MPI-Report 93, Max-Planck-Institut für Meteorologie, Hamburg, 1992.

Sachs, L., *Angewandte Statistik*, Springer Verlag, 846pp, 1992.

Schmitz, G., and N. Grieger, Model calculations on the structure of planetary waves in the upper troposphere and lower stratosphere as a function of the wind field in the upper stratosphere, *Tellus*, *32*, 207–214, 1980.

Shindell, D. T., R. L. Miller, G. A. Schmidt, and L. Pandolfo, Greenhouse gas forcing of Northern Hemisphere winter climate trends, *Nature*, *399*, 452–455, 1999a.

Shindell, D. T., D. Rind, N. Balachandran, J. Lean, and P. Lonergan, Solar cycle variability, ozone, and climate, *Science*, *284*, 305–308, 1999b.

SPARC, Stratospheric processes and their role in climate. SPARC. Initial review of objectives and scientific issues, Tech. rep., (Prepared by the SPARC scientific steering group), 1993, WMO/TD-No. 582.

SPARC, Stratospheric processes and their role in climate. Implementation Plan, Tech. rep., 1998, WMO/TD-No. 914.

Steil, B., M. Dameris, C. Brühl, P. J. Crutzen, V. Grewe, M. Ponater, and R. Sausen, Development of a chemistry module for GCMs: first results of a multiannual integration, *Ann. Geophys.*, *16*, 205–228, 1998.

Thompson, D. W., J. M. Wallace, and G. Hegerl, Annular modes in the extratropical circulation.Part II: Trends, *J. Clim.*, *13*, 1018–1036, 2000, submitted to J. Cim.

Thompson, D. W. J., and J. M. Wallace, The arctic oscillation signature in the wintertime geopotential height and temperature fields., *Geophys. Res. Lett.*, *25*, 1297–1301, 1998.

Thompson, D. W. J., and J. M. Wallace, Annular modes in the extratopical circulation. Part I: month-to-month variability, *J. Clim.*, *13*, 1000–1016, 2000.

Timmermann, A., M. Latif, R. Voss, and A. Grötzner, Northern Hemisphere interdecadal variability: A coupled air-sea mode, *J. Clim.*, *11*, 1906–1931, 1998.

Timmermann, A., J. Oberhuber, A. Bacher, M. Esch, M. Latif, and E. Roeckner, Increased El Niño frequency in a climate model forced by future greenhouse warming, *Nature*, *398*, 694–697, 1999.

Toth, Z., Degrees of freedom in Northern Hemisphere circulation data, *Tellus*, *47*, 457–472, 1995.

Trenberth, K., Atmospheric circulation climate change, *Climate Change*, *31*, 427–453, 1995.

Ulbrich, U., and M. Christoph, A shift of the NAO and increasing storm track activity over Europe due to anthropogenic greenhouse gas forcing, *Clim. Dyn.*, *15*, 551–559, 1999.

van Loon, H., and K. Labitzke, Association between 11-year solar cycle, the QBO and the atmosphere. Part II: Surface and 700 mb in the Northern Hemisphere in winter, *JC*, *1*, 905–920, 1988.

von Storch, H., and F. W. Zwiers, *Statistical Analysis in Climate Research*, Cambridge

University Press, pp 513, 1998.

Voss, R., R. Sausen, and U. Cubasch, Periodically synchronous coupled integrations with the atmosphere-ocean general circulation model ECHAM3/LSG, *Clim. Dyn.*, *14*, 249–266, 1998.

Wallace, J. M., and D. S. Gutzler, Teleconnections in the geopotential height field during the Northern Hemisphere winter, *Mon. Wea. Rev.*, *109*, 784–812, 1981.

Wallace, J. M., and Y. Zhang, Structure and seasonality of interannual and interdecadal variability of the geopotential height and temperature fields in the Northern Hemisphere troposphere, *J. Clim.*, *6*, 2063–2082, 1993.

Wallace, J. M., X. Chen, and D. Sun, Does low-frequency atmospheric variability exhibits regime like behavior?, *Tellus*, *43A*, 16–26, 1991.

Wallace, J. M., C. Smith, and C. S. Bretherton, Singular value decomposition of wintertime sea surface temperature and 500-mb height anomalies, *J. Clim.*, *5*, 561–576, 1992.

Wallace, J. M., Y. Zhang, and J. A. Renwick, Dynamic contribution to hemispheric mean temperature trends, *Science*, *270*, 780–783, 1995.

Wallace, J. M., Y. Zhang, and L. Bajuk, Interpretation of interdecadal trends in Northern Hemisphere surface air temperature, *J. Clim.*, *9*, 249–259, 1996.

Wang, X., and S. S. Shen, Estimation of spatial degrees of freedom of a climate field, *J. Clim.*, *12*, 1280–1291, 1999.